

**POLITECNICO DI TORINO**

Department of Mechanical and Aerospace Engineering  
Master of Science in Mechanical Engineering

**Characterization of mechanical  
properties for Tobacco Mosaic Virus  
through Metrological Atomic Force  
Microscopy**



**Tutors**

Prof. MATTEO FASANO  
Dr. GIAN BARTOLO PICOTTO

**Student**

ROBERTO SPADA

A.Y. 2019/2020

# Table of content

Abstract.....	9
1 Introduction .....	10
1.1 AFM Background .....	10
1.2 How AFM works .....	11
1.3 AFM static and dynamic mode .....	14
1.3.1 AM-AFM.....	14
1.3.2 AF-AFM .....	15
1.4 Force spectroscopy .....	16
1.5 Tobacco Mosaic Virus (TMV) .....	18
1.6 Mica: a substrate for AFM.....	20
1.7 Tip properties .....	21
1.8 Thesis objective .....	23
2 Models and methods.....	25
2.1 A model system for AM-AFM .....	25
2.2 Resonance frequency for rectangular cantilever.....	27
2.3 Hertz theory .....	31
2.4 Importance of adhesion at the nanoscale .....	38
2.5 Johnson Kendall Roberts Model (JKR).....	39
2.6 Derjagin, Muller, Toropov (DMT Model).....	40
2.7 Description of the instruments for INRiM experimentation.....	41
3 Results .....	46
3.1 Tests procedure and analysis of Q-factor .....	46
3.2 Amplitude oscillation tests.....	51
3.3 Spectroscopy force tests.....	56
3.4 Calculation of the Young Modulus for TMV and Mica .....	60
4 FEM Analysis.....	72
4.1 Frequency Response function for cantilever model .....	72
4.2 Force-indentation curves.....	74
5 Discussion of the results.....	79
5.1 Results from dynamic analysis .....	79
5.2 Evaluation of the mechanical properties from static analysis.....	81
6 Conclusion and future works.....	88
Bibliography .....	90

## List of figures

Figure 1 AFM Scheme. 1, Laser Diode; 2, cantilever; 3, mirror; 4, photodetector; 5, electronic control; 6, PZT scanner with the sample. Picture taken from “How the Atomic Force Microscope Works”, Davide Ricci and Pier Carlo Braga, 2004-Springer.....	12
Figure 2 Geometry of the cantilever: height (h), radius of curvature (r) and width (w) Picture taken from “How the Atomic Force Microscope Works”, Davide Ricci and Pier Carlo Braga, 2004 Springer.....	13
Figure 3 AM-AFM control scheme Fig.3 AM-AFM control scheme. Picture taken from Dynamic Modes of Atomic Force Microscopy, A. Schirmeisen, B. Anczykowski and Harald Fuchs.....	15
Figure 4 AF-AFM Control scheme Picture taken from Dynamic Modes of Atomic Force Microscopy, A. Schirmeisen, B. Anczykowski, and Harald Fuchs.....	16
Figure 5 Lennard Jones potential as function of intermolecular distance. Picture taken from Wikipedia.....	18
Figure 6 Tobacco mosaic virus infection. Left: Leaf of a healthy tobacco plant. Center: Leaf of a TMV-infected plant Right: Organization and dimensions of a TMV ribonucleoprotein particle. This picture was taken from “Novel roles for well-known players: From tobacco mosaic virus pests to enzymatically active assemblies, Beilstein Journal of Nanotechnology, 613-629 .....	19
Figure 7 AFM examination of TMV onto mica. Picture taken from “Atomic force microscopy examination of tobacco mosaic virus and virion RNA”, Yuri F. Drygin, Olga A. Bordunova, Marat O. Gallyamov, Igor V. Yaminsky. ....	20
Figure 8 AFM mica discs. Picture taken from AGAR Scientific Website.....	21
Figure 9 Triangular silicon nitride cantilever. Picture taken from Soquelec website ....	22
Figure 10 Chip array size of Silicon nitride Cantilevers. Picture taken from Olympus-global website.....	23
Figure 11 Schematic of driven damped harmonic oscillator. Picture taken from Voigtländer, B. (2019). Atomic Force Microscopy. NanoScience and Technology.....	25
Figure 12 Schematic of cantilever-tip system in 3D. Picture taken from Dynamic atomic force microscopy and methods, R. Garcia.....	28
Figure 13 Plot relating the real and imaginary hydro-dynamic function to Reynolds number. Picture was taken from "Calibration of rectangular AFM", Sader.....	30
Figure 14 Graphic interpretation of the Quality factor as function of bandwidth. Picture taken from Electronicnotes website.....	31
Figure 15 Representation of contact between surface and plane.....	32
Figure 16 Two surfaces in contact at point P. ....	34
Figure 17 Curves of $\alpha$ and $\beta$ with respect to $\tau$ .....	35
Figure 18 Hertzian contact between sphere and elastic half-space. Picture taken from Norton, 2008.....	36
Figure 19 Illustration of AFM Metrological in INRiM.....	42
Figure 20 Zoom of the AFM Metrological: 1. support, 2, PZT scanner, AFM head (where the cantilever and the photodiode are placed) .....	43
Figure 21 Schematic of AFM interferometer .....	44
Figure 22 Piezoelectric control loop made in INRiM .....	45
Figure 23 Oscilloscope. It shows how the cantilever tip moves along x and y direction	45
Figure 24 Cantilever NP-20 n.3 made by Veeco, spring constant $k = 0.58$ N/m, seen	

through optical profilometer Sensofar PLu2300, confocal mode with 20x magnification, 21/10/2020. The black square in the picture correspondes to the cantilever tip. ....	48
Figure 25 Display of resonance search through "Resonance tool" .....	50
Figure 26 Picture of TMV sample topography. Size 25000nm, 256x256 pixel, 250 nN and spring constant equal to 0.12 N/m .....	51
Figure 27 Variation of the tip amplitude oscillation vs Z-piezoelectric offset for TMV in the approach phase with cantilever stiffness 5 N/m. Non-contact tip, 08/10/2020 .....	52
Figure 28 Variation of the tip amplitude oscillation vs Z-piezoelectric offset for TMV in the retract phase with cantilever stiffness 5 N/m. Non-contact tip, 08/10/2020 .....	52
Figure 29 Variation of the tip amplitude oscillation vs Z-piezoelectric offset for Mica in the approach phase with cantilever stiffness 5 N/m. Non-contact tip, 08/10/2020 .....	53
Figure 30 Variation of the tip amplitude oscillation vs Z-piezoelectric offset for Mica in the retract phase with cantilever stiffness 5 N/m. Non-contact tip, 08/10/2020 .....	53
Figure 31 Variation of the tip amplitude oscillation vs Z-piezoelectric offset for TMV in the approach phase with cantilever stiffness 0.12 N/m. Contact tip, 21/10/2020 .....	54
Figure 32 Variation of the tip amplitude oscillation vs Z-piezoelectric offset for TMV in the retract phase with cantilever stiffness 0.12 N/m. Contact tip, 21/10/2020.....	54
Figure 33 Variation of the tip amplitude oscillation vs Z-piezoelectric offset for Mica in the approach phase with cantilever stiffness 0.12 N/m. Contact tip, 21/10/2020 .....	55
Figure 34 Variation of the tip amplitude oscillation vs Z-piezoelectric offset for Mica in the retract phase with cantilever stiffness 0.12 N/m. Contact tip, 21/10/2020.....	55
Figure 35 Force spectroscopy of Mica. Comparison between approach and retract for non-contact tip, 08/10/2020 .....	57
Figure 36 Force spectroscopy of TMV. Comparison between approach and retract for non-contact tip, 08/10/2020 .....	58
Figure 37 Force spectroscopy of Mica. Comparison between approach and retract for contact tip, 21/10/2020 .....	58
Figure 38 Force spectroscopy of TMV. Comparison between approach and retract for contact tip, 21/10/2020 .....	59
Figure 39 Postprocessing of FEM simulation of rectangular cantilever .....	73
Figure 40 FRF for 08/10/2020 test .....	73
Figure 41 FRF for 20/10/2020 test .....	74
Figure 42 FEM Simulation of Cantilever-TMV nanoindentation.....	76
Figure 43 FEM Validation for Force-depth penetration curve, TMV .....	76
Figure 44 FEM Simulation of cantilever-mica nanoindentation.....	77
Figure 45 FEM Validation for Force-depth penetration curve, Mica.....	77
Figure 46 FEM Validation for contact radius - depth penetration curve, TMV.....	78
Figure 47 FEM Validation for contact radius - depth penetration curve, Mica .....	78
Figure 48 Indentation force - Depth penetration curve for TMV and comparison with other methods .....	84
Figure 49 Indentation force - depth penetration curve for mica and comparison with other method.....	85
Figure 50 Contact radius - depth penetration for TMV and comparison with the other theories .....	85
Figure 51 Contact radius - depth penetration for mica and comparison with the other theories .....	86
Figure 52 Force-displacement curves varying TMV Young Modulus.....	87
Figure 53 Force-displacement curve varying Mica Young Modulus.....	87

## List of tables

Table 1 Description of area contact shape according to some particular cases.....	35
Table 2 List of the cantilevers used for Metrological AFM .....	47
Table 3 E-B equation for Q-factor.....	49
Table 4 Q-factor with Reynolds .....	49
Table 5 Experimental Q-Factor .....	50
Table 6 Calculation of force-voltage coefficient for non contact tips.....	57
Table 7 Calculation of force-voltage coefficient for contact tips.....	57
Table 8 Stiffness for all the force-distance curves .....	60
Table 9 Calculation of mechanical properties for TMV with non-contact tip .....	62
Table 10 Calculation of mechanical properties for Mica with non-contact tip.....	63
Table 11 Calculation of mechanical properties for TMV with contact tip, 13/10/2020	64
Table 12 Calculation of mechanical properties for TMV with contact tip, 21/10/2020	65
Table 13 Calculation of mechanical properties for TMV with contact tip, 21/10/2020	65
Table 14 Calculation of mechanical properties for TMV with contact tip, 22/10/2020	66
Table 15 Calculation of mechanical properties for MICA with contact tip, 13/10/2020	67
Table 16 Calculation of mechanical properties for MICA with contact tip, 21/10/2020	68
Table 17 Calculation of mechanical properties for MICA with contact tip, 21/10/2020	69
Table 18 Calculation of mechanical properties for MICA with contact tip, 22/10/2020	69
Table 19 Young Modulus for Mica and TMV according to the models used. All the data are reported in the form of tables and hystograms. ....	71
Table 20 Resonant frequency and quality factor given by FEM Simulation .....	74
Table 21 Elastic properties used for FEM Simulation .....	75
Table 22 Comparison of resonant frequency.....	80
Table 23 Comparison of Q-factor.....	80
Table 24 Average value and standard deviation of resonant frequency and Q-factor ...	80
Table 25 Young Modulus for TMV and Mica, Mean Value and Standard Deviation for contact tip .....	81
Table 26 Depth penetration for TMV and Mica, Mean Value and Standard Deviation for contact tip .....	82
Table 27 Contact radius for TMV and Mica, Mean Value and Standard Deviation for contact tip .....	82
Table 28 Mechanical properties estimated with non-contact cantilever .....	83

## List of symbols

$\gamma$	$\text{J/m}^2$	Surface energy per unit area
$k$	$\text{N/m}$	Spring constant
$f_0$	$\text{Hz}$	Resonant frequency
$\rho$	$\text{Kg/m}^3$	Density
$\eta$	$\text{N s/m}^2$	Viscosity coefficient
$\text{Re}$		Reynolds number
$r$		Imaginary part of the hydro-dynamic function
$L$	$\text{m}$	Cantilever length
$W$	$\text{m}$	Cantilever width
$t$	$\text{m}$	Cantilever thickness
$m$	$\text{kg}$	Cantilever mass
$G$		Force-Voltage coefficient
$S$	$\text{N/m}$	Stiffness
$\nu$		Poisson ratio
$E'$	$\text{Pa}$	Reduced Young modulus
$E$	$\text{Pa}$	Young modulus
$A$	$\text{m}^2$	Contact area
$a$	$\text{m}$	Contact radius
$h$	$\text{m}$	Depth penetration / Deformation
$R$	$\text{m}$	Curvature radius
$F$	$\text{N}$	Force
$\alpha, \beta$		Coefficient for ellipse semi-axis
$q$	$\text{m}$	General contact radius (elliptical area)

## List of abbreviations

AFM	Atomic Force Microscopy
AF-AFM	Atomic Force Microscopy – Amplitude modulation
AM-AFM	Atomic Force Microscopy – Frequency modulation
DMT	Derjagin Muller Toropov
FEM	Finite Element Method
HOPG	Highly oriented pyrolytic graphite
INRiM	Institute National Research in Metrology
JKR	Johnson Kendall Roberts
PID	Proportional, Integrative and Derivative
SPM	Scanning Probe Microscopy
TEM	Transmission Electron Microscope
TMV	Tobacco Mosaic Virus

## Acknowledgments

I would like to thank all the people who have contributed to help and support me during this work of thesis and all the colleagues with whom I shared experiences and dreamed of the final goal of this university path.

First of all my **parents**, who have been present in each moment of my life, who have me taught that when something goes wrong, I must never give up and believe in my sacrifices, in my abilities and in all the qualities that will help me become a good man and a good engineer.

**Matteo Fasano**, my supervisor, who has really supported me since the first mail I have sent him, for his availability when I need his assistance, for the opportunity to explore a new scientific world, for showing me a great humanity beyond professionalism.

**Gian Bartolo Picotto** and **Luigi Ribotta**, my guides during these months in INRiM and for the constant presence during my thesis work.

Thanks to all my old **friends**, who have seen me grow up, to the new ones, who have demonstrated how much they appreciate the person I am.

# Abstract

The traceability of materials has become one of the most interesting topics of metrological research studies and a valid instrument for the reliability of the characterization tests. The definition of new samples and the regulation of industrial measurement instruments and systems require to follow several steps for an accurate calibration. INRiM works with nanostructure tests, exploiting the potential of a metrological Atomic Force Microscope (AFM). The first part of this work is essentially based on several kinds of AFM measurements on Tobacco Mosaic Virus (TMV), in order to check if this virus could become an ideal reference material. To do that, it is important to verify its diameter stability and AFM calibration has been done using different type of tips.

Second, a novel contribution of this thesis is to validate a new model for the calculation of mechanical properties of nanomaterials using the AFM, such as the sample's Young Modulus, comparing all the measurements done in laboratory with FEM analysis.

All the results obtained are used to demonstrate if TMV can be referable to the international system and a good quality of the measurements could have a good impact in the field of research for systems at the nanoscale.

# 1 Introduction

## 1.1 AFM Background

In the last years, the development of nanotechnology has grown fast and today it involves several scientific and technological studies. For this reason, scientists and researchers around the world are trying to tackle a new challenge: investigating the material properties at the nanoscale. The aim of this study is to discover a new mechanical characterization and then verify it with different tests<sup>1</sup>.

In 1986, Binning, Quate and Gerber were recognized as the leading inventors of Atomic Force Microscopy (AFM). It represents an important innovation for the topographic and mechanical analysis of surfaces of different materials, such as metals, polymers, composite materials and at the same time it had a strong impact on a medical level, given its ability to study biological tissues, biomolecules or macromolecules (proteins, DNA, RNA, plastics), useful for biochemical and biophysical applications<sup>2</sup>.

The atomic force microscope is a so flexible tool that provides the mapping of samples with a resolution higher than the one of the optical and electrical microscopes.

AFM belongs to SPM (Scanning Probe Microscopy) family and the surfaces of samples are scanned with a sharp tip at the free end of the cantilever. Surface mapping generates images, visible on a laptop, and provides information on mechanical properties of materials (stiffness, hardness, friction, dissipation and adhesion), electrical properties (capacitance, electrostatic forces, potentials, electric currents), magnetic and optical properties. The sample is typically placed on a substrate and the experiment can be performed in different modes (tapping mode, contact mode, no contact mode, nanoindentation etc.) and it is observed how the force-distance curve between tip and sample varies. When the cantilever bends forwards, it approaches the surface and the force is typically attractive, when it starts to deflect backwards, away from the sample, the force becomes repulsive and it derives from the adhesion at the

interface. In this way it is possible to trace different mechanical properties, depending on different factors, one of these is the geometry of the tip.

Another method for evaluating the mechanical properties of materials is to perform FEM analysis, which offers a valid alternative to the experimental method, providing details about the deformation of the sample in the loading and unloading phases, by reproducing a model of the system at a computational level.

In recent decades, efforts have been made to optimize these models and to make their contribution increasingly effective, in order to evaluate all the properties and sample performances in a more complex way. For instance, their application is finding wide space in the pharmaceutical world, where mechanisms are being studied. They develop biomolecular systems; whose functions assume great importance in the study of cellular processes<sup>3</sup>. In this way it is possible to propose, and then produce, a pharmaceutical-type product capable of inhibiting the development and the multiplication of cancer cells within an organism.

In fact, in 1993, the tapping mode was introduced to study proteins in a non-destructive way, by adjusting the frequency oscillation of the cantilever<sup>4</sup>. AFM has had a great importance in the study of the biomolecules, reproducing them at a very high resolution, in order to carry out an analysis of their dynamic structure.

## **1.2 How AFM works**

The atomic force microscope was introduced in 1986, giving rise to a new way to study samples at very high resolution. It is mainly composed of a cantilever beam, with a sharp tip, which can be conical, spherical or cylindrical.

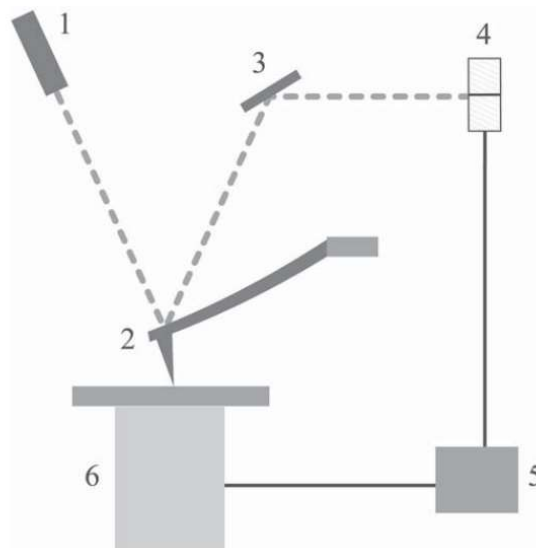


**Figure 1 AFM Scheme. 1, Laser Diode; 2, cantilever; 3, mirror; 4, photodetector; 5, electronic control; 6, PZT scanner with the sample. Picture taken from “How the Atomic Force Microscope Works”, Davide Ricci and Pier Carlo Braga, 2004-Springer**

In the first years after AFM invention, the indenter tip made of diamond has been used, then the silicon has taken its place as it allows greater uniformity and reproducibility of the results. These evaluations are affected mainly by the tip radius and its geometry. The cantilever is fixed to a small glass chip that allows for easy manipulation of the instrument. It can be made in a V or a single arm, the difference between the two forms lies in the different torsional properties. Its dimensions, such as length, width and thickness, determine the mechanical properties of the cantilever, through which it is possible to understand the operating modes necessary to investigate the sample. Cantilevers are classified according to their resonance frequency: we speak of cantilever with low resonance frequency for applications on liquids and in non-contact mode, rigid and high frequency cantilevers for resonance mode in air<sup>5</sup>.

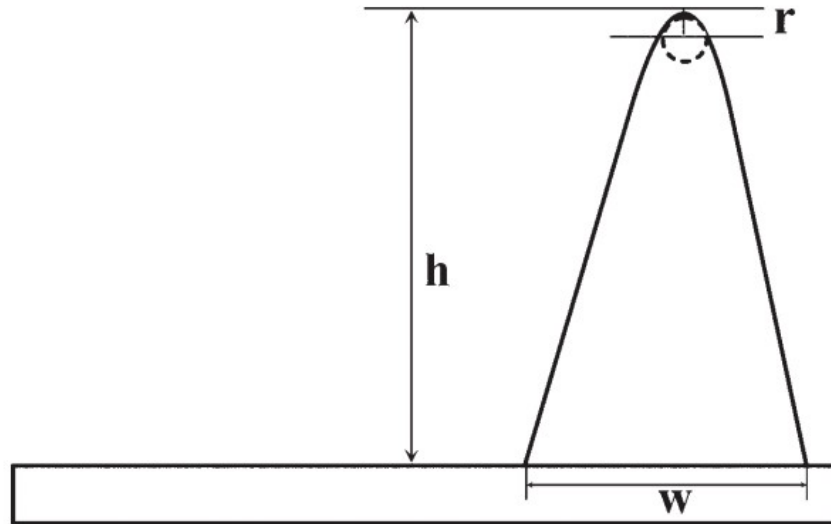


**Figure 2 Geometry of the cantilever: height ( $h$ ), radius of curvature ( $r$ ) and width ( $w$ )**  
 Picture taken from “How the Atomic Force Microscope Works”, Davide Ricci and Pier Carlo Braga, 2004 Springer

In order to measure the vertical deflection of the cantilever, an optical lever is used to measure its displacement when it moves from its equilibrium. A laser beam is reflected from the top of the cantilever, generally coated with a thin layer of metal, on a photodetector. When the cantilever deflects, the reflection of the beam on the photodiode changes. Therefore, if the photodetector has 4 sectors, it is also possible to evaluate the forces that cause the torsion of the cantilever. The piezoelectric scanner (6, in Fig. 2) is guided by AFM control system to position the sample. The tip scans the sample along the defined x-axis and y-axis, until the topographic image is reproduced. It is essential the probe does not get too close to the sample, so the risk of damage to the tip or to the surface to detect is avoided. Furthermore, it is observed that, during the scanning phase, the morphology of the sample does not remain constant. It means that the cantilever deflection is changed. Hence a feedback circuit is installed to move the tip perpendicularly to the analyzed surface, in order to keep the tip-sample interaction force constant.

A signal is produced, and it is proportional to the tip-sample distance, so a 3D image of the sample is reproduced and shown on video through an external device (laptop)<sup>6</sup>.

## 1.3 AFM static and dynamic mode

Three modes have been studied for atomic force microscopy: the static mode, or more commonly known as contact mode, and two dynamic modes, such as tapping mode and contact mode.

The static mode is the simplest of those analyzed and was the first to be performed from a temporal point of view. The tip of the cantilever is pulled on the surface of the sample and the force exerted is kept constant. In this way the contact between the tip and the sample is ensured, while cantilever deflection value is fed back and compared with the set value. An error is given by the difference between these two values and it is sent to the control system. Then, the piezoelectric scanner is commanded to move along z-axis (perpendicular to the sample) and the tip-sample interaction force does not change because of the scanner's displacement. Although it is not very difficult to operate and acquire images in this mode, there are some limits due to the adhesion forces, the possible sticking of the tip to the surface and the inability to identify possible surface defects during the imaging phase. Furthermore, it is not possible to work in UHV conditions, i.e. ultra-vacuum. For this reason, dynamic conditions are preferable: in this case, the cantilever oscillates at the resonant frequency<sup>7</sup>.

In the dynamic mode images can be acquired in two different modes: the tapping mode, or intermittent contact mode, where the amplitude is modulated (AM-AFM), and the non-contact mode, or frequency modulation (AF-AFM). A greater molecular resolution for biological samples in environmental conditions is guaranteed and, as mentioned above, the problem of image acquisition in very high vacuum conditions is solved<sup>8</sup>. It can work both in air and in water, representing a very important feature for the study of biological systems. Furthermore, AM-AFM is easier to manage and cheaper than AF-AFM.

### 1.3.1 AM-AFM

Amplitude modulation atomic force microscopy (AM-AFM) allows to scan the surface

of any sample, where the cantilever is excited from the outside at a frequency very close to the resonant one, keeping its oscillation amplitude constant. As noticed in the Fig.3, the photodiode detects the oscillation of the cantilever and the output signal is analyzed in the Lock-in amplifier, where information on phase and amplitude is obtained. The amplitude value is compared with the set value and the error is sent in the PID (proportional, integrative and derivative) control, in order to command PZT scanner's displacement. In the other hand, the function generator sends an excitation signal to the cantilever at a resonance frequency and a reference signal to the Lock-in amplifier.

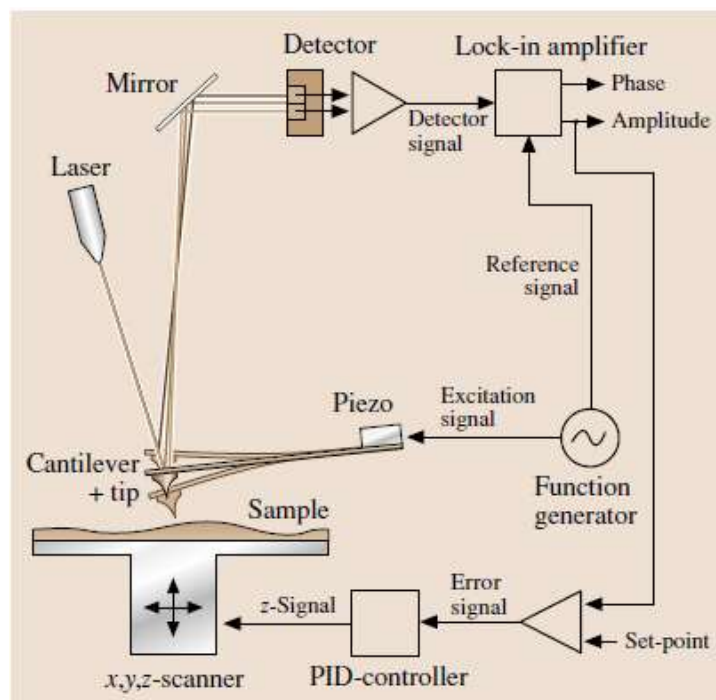


**Figure 3 AM-AFM control scheme** Fig.3 AM-AFM control scheme. Picture taken from *Dynamic Modes of Atomic Force Microscopy*, A. Schirmeisen, B. Anczykowski and Harald Fuchs

### 1.3.2 AF-AFM

Frequency modulation for AFM is used to make measurements in the environments, and they are quite useful for the research field. It works in UHV condition with pressures of the order of  $10^{-10}$  Pa. In this case it is important the system oscillates at the same frequency, for this reason a feedback loop has been added. For this purpose, the frequency demodulator detects the frequency shift, as well as the frequency variation due to the tip-

sample interaction. Its value, converted in voltage (V), is subsequently sent to the PID controller in order to adjust the tip-sample distance. At the same time, it is necessary the amplitude is kept constant in order not to affect the tip-sample interaction. Then, a closed loop control is also added for the amplitude. Its control leads to its gain variation and, after a phase shift, an excitation signal is sent to the cantilever<sup>9</sup>.

With various experiments, it has been seen that it is possible to use more rigid cantilevers and further reduce the oscillation amplitudes to improve the contrast of imaging. In this way, better resolution can be achieved for smaller tip-sample distances. It means that, having smaller frequency shift  $\Delta f$  for each point of the surface (where tip-sample distance is calculated) is a good result for a better resolution.

Compared to AM-AFM, the sensitivity is greater, and it is independent of the bandwidth it can work with. It can detect up to 500 Hz.

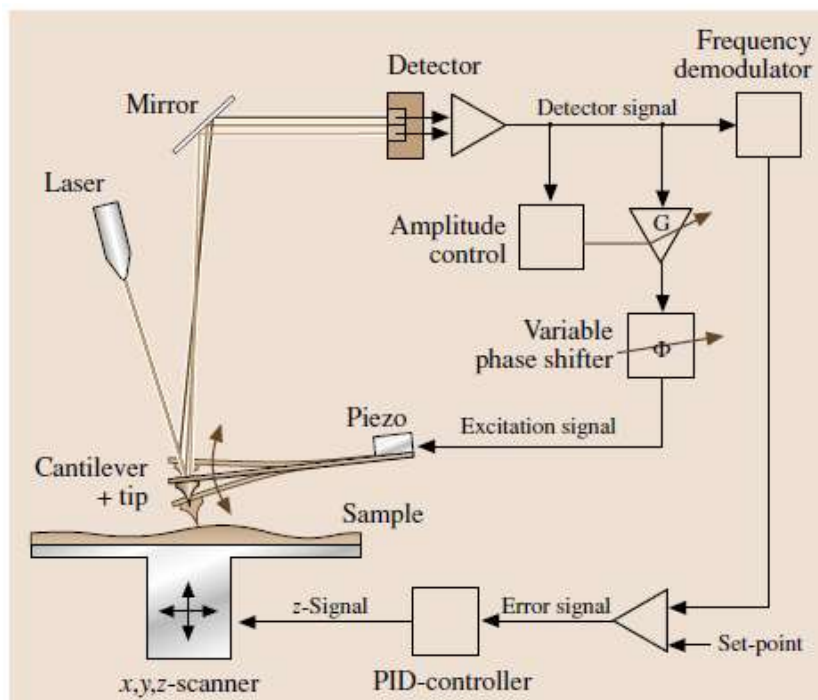


**Figure 4 AF-AFM Control scheme** Picture taken from *Dynamic Modes of Atomic Force Microscopy*, A. Schirmeisen, B. Anczykowski, and Harald Fuchs

## 1.4 Force spectroscopy

One of the useful features of the atomic force microscope is that it can be used for force

spectroscopy. Its aim is to measure the interaction between the tip and the sample as a function of the distance. This method helps to calculate sample's mechanical properties at the nanoscale. Suppose the cantilever moves along z-axis, perpendicular to the sample's surface. At first, when the force between molecules is attractive, the cantilever bends downwards and, as consequence, deflects vertically. This process is known as nanoindentation and represents a different way to study the interactions between the tip and the sample.

The cantilever is kept in contact with the surface for some time, then it retracts upwards. In this way it is possible to calculate the tensile strength and then the respective force. Force spectroscopy is used in biophysics to study the properties of cells and tissues with different stiffness and is applied at the nanoscale to study Van der Waals forces<sup>10</sup>. Lennard and Jones introduced a law in which the intermolecular potential varies with distance. It is an empirical function, renamed as 12-6 law:

$$U(r) = 4\xi \left( \left( \frac{\sigma}{r} \right)^{12} - \left( \frac{\sigma}{r} \right)^6 \right) \quad (1.1)$$

Where  $r$  is the distance between molecules,  $\xi$  is the depth of the potential well,  $\sigma$  is the distance at which the particle-particle potential is equal to zero. The force value is obtained as the gradient of the defined potential.

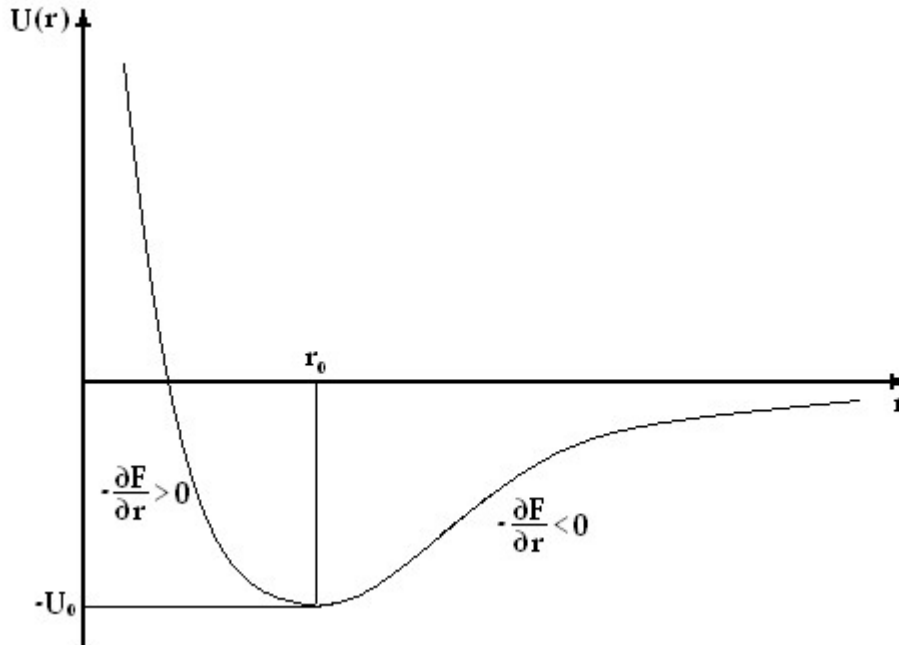


*Figure 5 Lennard Jones potential as function of intermolecular distance. Picture taken from Wikipedia*

## 1.5 Tobacco Mosaic Virus (TMV)

Tobacco mosaic virus is a highly infectious virus, manifested by the formation of yellow spots on the leaves of the plants and it causes their deformation or wrinkling. It was discovered at the end of the 20th century, when Adolph Mayer noticed tobacco's disease on the homonym plant and his investigation was then extended to other crops, including tomatoes. Dmitry Ivanovsky realized the main cause of the spreading of this virus between plants is a filterable sap, that was able to self-replicate and transmit plant to plant. Some experiments conducted in a laboratory lead to the crystallization of the virus, and it was awarded with the Nobel Prize in 1946. Tobacco mosaic virus (TMV) was then defined as a single-stranded RNA virus<sup>11</sup>.

It is characterized by the presence of a capsid, consisting of 2130 molecules of coating proteins, assembled around the genome. The virion measures almost 300 nm in length and 18 in thickness.

It encodes 4 genes: two proteins associated with a replicase, a motion protein and a capsid

protein. This type of virus, in most of the cases, weakens the plants without killing them and it is very difficult to recognize the symptoms of the virus. It is very resistant to high temperature and it can live in the soil. Aphids are the most common insects, known as main infectors of this virus<sup>12</sup>.

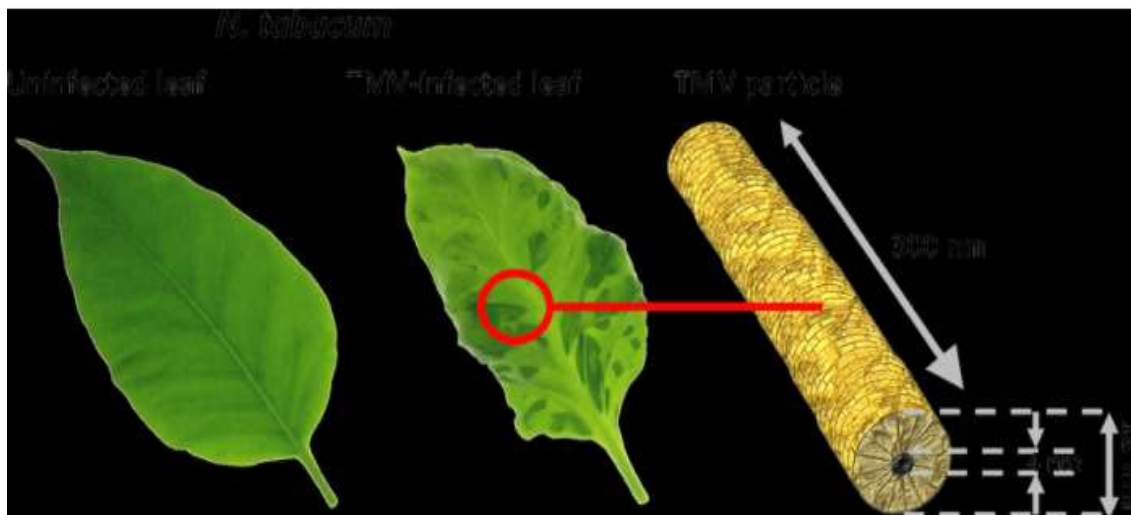


**Figure 6 Tobacco mosaic virus infection. Left: Leaf of a healthy tobacco plant. Center: Leaf of a TMV-infected plant Right: Organization and dimensions of a TMV ribonucleoprotein particle. This picture was taken from “Novel roles for well-known platers: From tobacco mosaic virus pests to enzymatically active assemblies, Beilsetein Journal of Nanotechnology, 613-629**

By the 1980s the interest of scientists and researchers towards the virus structure and its particles increased rapidly and TMV found its application in nanotechnology and in biological field. The cylindrical form of its particles suggests a filamentous morphology of the virus and its 3D structure makes it a very interesting sample to analyze through electron microscope<sup>13</sup>.

The first observations of TMV were made by using an electron microscope, however some limitations were found during the investigation. Some of them are due to the difficulty encountered to analyze RNA, such as the need to complex RNA with a basic protein and staining the sample with metals in order to create a contrast and a better observation of the virus.

The introduction of TEM and then AFM was applied to solve these drawbacks, making possible the study of the interaction between virial RNA and protein and understanding

something more about the behavior of this virus in particular environment under certain conditions<sup>14</sup>.

Tobacco mosaic virus is the first virus discovered by man and for this reason it represents one of the most interesting structure to study. All his properties can acquire a great importance from a biological point of view. It has a great tensile stress and it has a good thermal stability, in fact it can withstand heating to 60°C for half-hour, its pH lever is around 7 and it presents other advantages like non-abrasively, biocompatibility with other molecules.

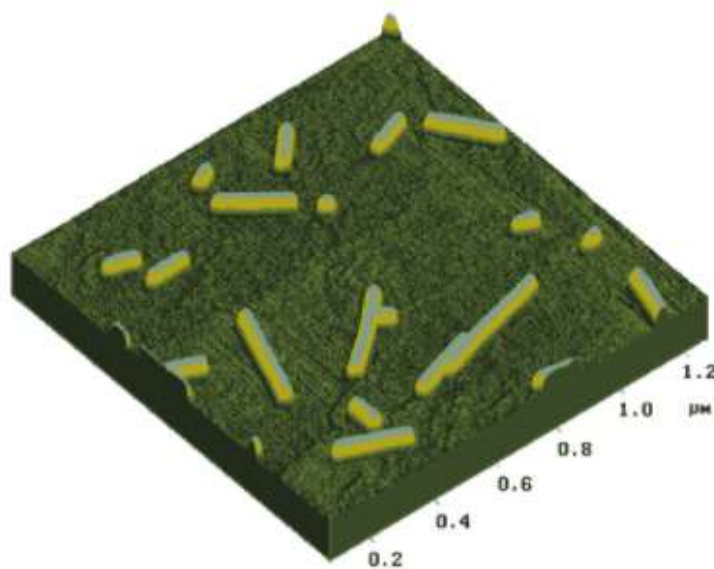


*Figure 7 AFM examination of TMV onto mica. Picture taken from “Atomic force microscopy examination of tobacco mosaic virus and virion RNA”, Yuri F. Drygin, Olga A. Bordunova, Marat O. Gallyamov, Igor V. Yaminsky.*

## 1.6 Mica: a substrate for AFM

In AFM all the probed samples are typically deposited on a substrate, one of this is the muscovite mica.

Mica belongs to the phyllosilicate family and its chemical composition is quite similar to a crystal structure. Its main features are the flatness and the cleavage because of its very small thick and the sheet-like arrangement of its atoms. It has a negative charge and it has

been used as ideal support of biomolecules. Mica disks are prepared following a precise protocol, in order to make all the measurements with accuracy and precision. In fact, the disk size changes according the tip approach speed and the quality of resolution in AFM analysis. It remains stable under high temperature and maintains a good behavior when exposed at electricity.

Before using it for AFM, cations are distributed on its surface, it means that it has acquired a negative charge and it is suitable for molecules analysis with positive charge. For this reason, mica needs treatments like chemical modification to prepare it for the sample. For some AFM applications, it can be coated by polystyrene and cationic lipids following carefully other several protocols<sup>15</sup>.

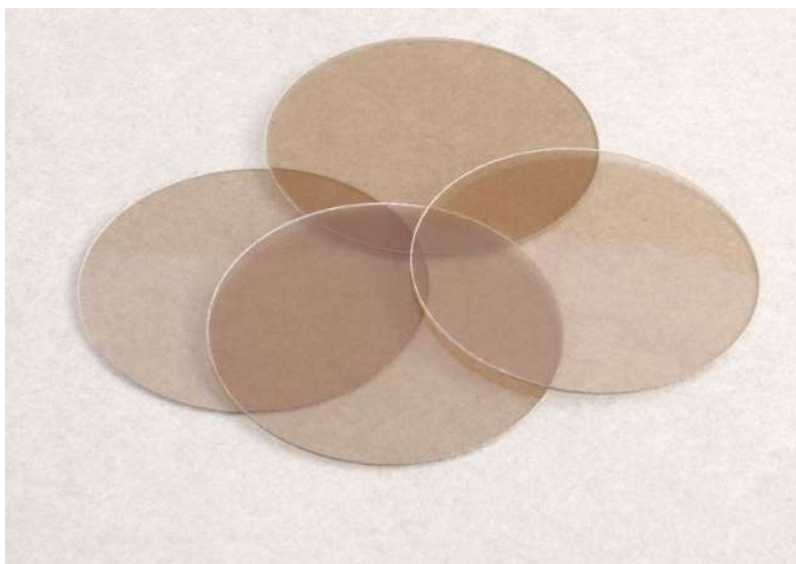


*Figure 8 AFM mica discs. Picture taken from AGAR Scientific Website*

## **1.7 Tip properties**

Cantilever can be made with different types of materials, particularly we focus our attention on Si (silicon) and Si<sub>3</sub>N<sub>4</sub> (silicon nitride). The tip is located at the free end of cantilever and it approaches samples surface according the modes AFM works. Generally, it moves along x-direction and jumps line to line along y-axis, thus reproducing 3D image of the sample. In this way it is possible to identify its properties as a function of tip geometry, tip approach speed and tip-sample distance. For example, the thickness is made depending on material properties and its manufacture. Cantilevers are

ranked according to their geometry in triangular and rectangular shape. The first guarantees a right alignment but it is very difficult to handle mathematically, the second allows to define all the properties in a linear way and it works in a contactless mode.

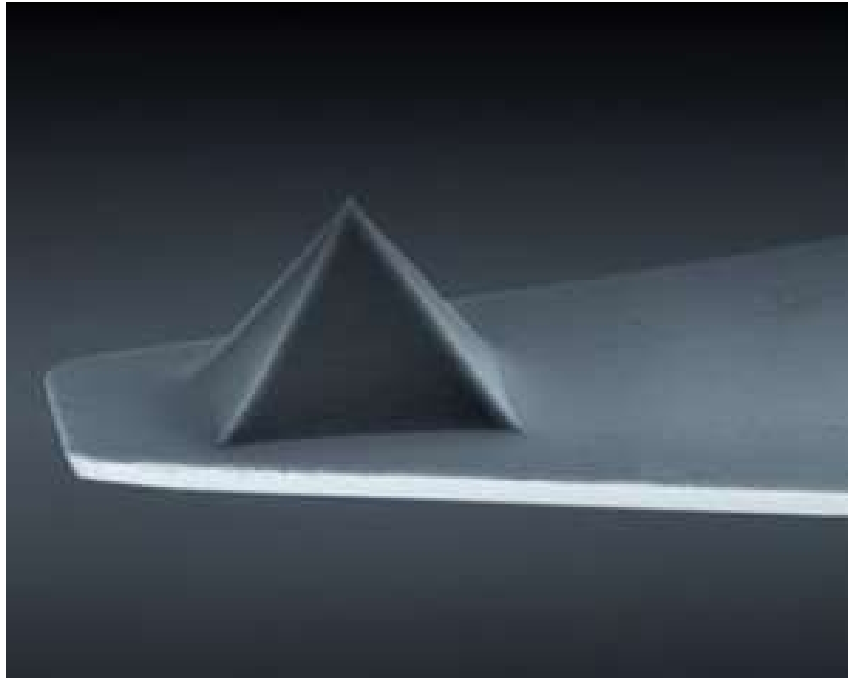


*Figure 9 Triangular silicon nitride cantilever. Picture taken from Soquelec website*

Before installing AFM tips in the AFM head, some very important steps should be followed:

1. Inspect the wafer with microscope to see if it is oriented in the same tip direction
2. Remove the Pyrex strip pressing downwards with the tweezers. In this way the strip is separated from the silicon ring.
3. Put the strip on a piece of paper and studying it under microscope observation
4. Place it on a glass side, grasps the end of the strip with wide tweezers and rotating down until breaking the cantilever substrate free from the others. These are divided by saw cuts.
5. Every cantilever provides two cantilevers with two different leg widths. During measurements, the unused cantilever should be removed for a safe application. A very important caveat is to make sure that each cantilever is on the top side of the substrate.

During their fabrication, a large percentage to find imperfection is possible. During their manufacturing process, imperfections could determine limits in the tip sharpness, and it could affect all measurements and the topographical resolution of the sample under analysis.

If the imperfection of the etch pits limits  $\text{Si}_3\text{N}_4$  cantilever sharpness and therefore tip radius of curvature, those in silicon represent a very valid alternative. The processing steps to their realization does not change but they require very precise wafer for a good etching. Silicon cantilevers cannot be as thin as silicon nitride ones, as consequence its stiffness is higher. They cannot be used in the AFM contact mode. One of the reasons is the fact they could destroy organic sample during testing and have a poor reflectivity in liquid environments<sup>16</sup>.

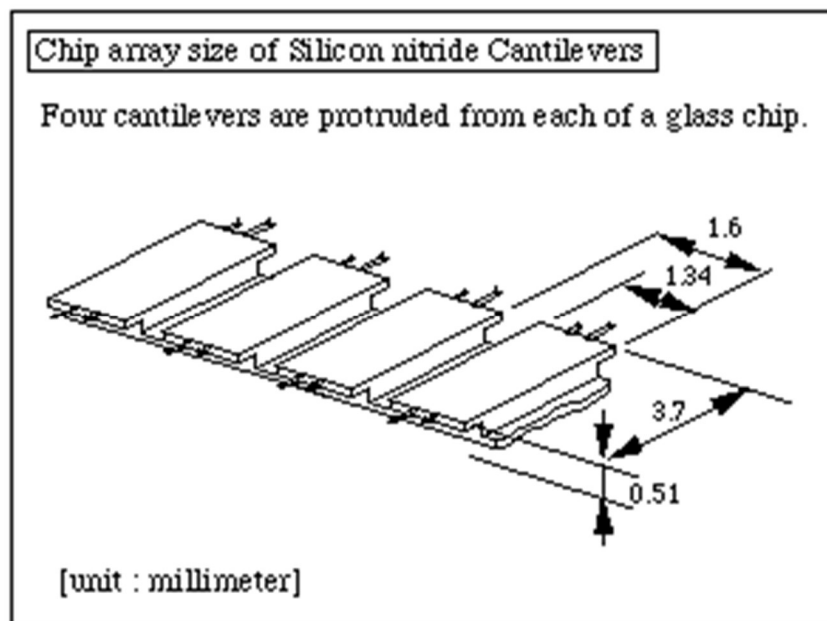


*Figure 10 Chip array size of Silicon nitride Cantilevers. Picture taken from Olympus-global website*

## 1.8 Thesis objective

In the recent years, a large part of metrological research was based on the use of metrology AFM. For accurate and traceable measurements, the Hertzian sphere-

sphere model has been applied to study nanoparticles behavior, and their data analysis compared with x-rays scattering and DLS measurements. Over the past decade, TiO<sub>2</sub> nanoparticles have become the first candidate reference material with non-spherical geometry for measurements at the nanoscale. For this reason, models have been developed to study the critical dimension of the bodies in contact.

TMV studies were done through X-rays diffraction and the effective diameter length was discovered, which was shown to be equal to approximately 18 nm. For this reason, tobacco mosaic virus represents the first natural material, used as reference material because of its stability in dimension (especially for its diameter) and over time.

Metrology interests is aimed at modelling the candidate tip characterizer. Thus, the main purpose of this thesis is to perform experimental tests and calculate the mechanical properties of TMV sample analyzed in INRiM (National Institute of Metrology Research), placed in Torino, by manipulating a metrological atomic force microscope. All the images it generates are scanned in non-contact mode, based on the amplitude modulation (AM-AFM). TVMs are described as rods, thus implies the study of mechanical contact between sphere and cylinder at the nanoscale by several models, in order to evaluate if it is possible to apply them for nanostructure of different shapes. All the measurements have been done using different type of tips, typically in silicon nitride, so that possible variations can be evaluated, and to confirm if the model used is well suited to describe the experiments carried out. At the end, FEM analysis is used to compare all the results obtained.

After having introduced a review of the state-of-art of atomic force microscopy, the thesis is organized according the following structure: chapter 2 provides an overview of all the models applied for AM-AFM and the formulation of contact mechanic theories for the examined cases. At the end of this chapter the instrumentation used in INRiM laboratory is described. Thereafter, in chapter 3 the results will be presented, and FEM analysis procedure depicted in chapter 4. In the last two chapters the discussion of the results and the conclusion will be drawn, proposing the limits, and possible improvements for AFM calibrations and measurements.

## 2 Models and methods

### 2.1 A model system for AM-AFM

A model for AM-AFM becomes necessary for the study of the behavior of the cantilever when moves from its equilibrium to the surface sample. At a first impact, this beam can be modeled as a free harmonic oscillator, but it is easier to realize that in this case the resonant frequency tends to infinite. It means that the cantilever continues to oscillate without stopping. Considering the damping factor, it is possible to describe the system in a real way, with the viscous damping proportional to the velocity, so that the force exerted is opposite to the same velocity.

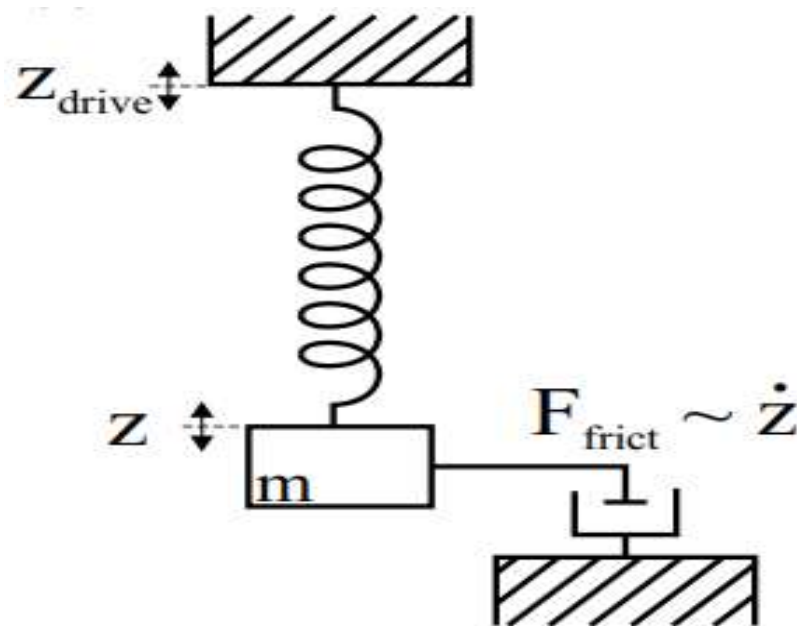


*Figure 11 Schematic of driven damped harmonic oscillator. Picture taken from Voigtländer, B. (2019). Atomic Force Microscopy. NanoScience and Technology*

The cantilever is characterized by three degrees of freedom: amplitude, frequency and phase shift. The approximation of the system to a damped driven harmonic oscillation leads to introduce, according to Newton's laws, the following equation<sup>17</sup>:

$$m\ddot{z} + \beta\dot{z} + \beta z = kz_d \quad (2.1)$$

Where  $m$  is the mass of the cantilever,  $\beta$  is the damping factor,  $k$  is the spring constant and  $kz_d$  is an external force that drives cantilever oscillation,  $z_d$  is modeled as a sinusoidal signal,  $z_d = A_d \cos(w_d t)$ . Dividing all the equation by  $m$ ,  $w_o$  is calculated, that turns out to be the resonant frequency at free oscillation (without damping). The damping factor and the mass are related to a dimensionless parameter we introduce: it is called Quality factor, which is anti-proportional to  $\beta$ :  $Q = m * w_o / \beta$ . The equation (2.1) becomes as follow:

$$\begin{aligned} z \ddot{+} \frac{w_o}{Q} \dot{z} + w_o^2 z & \quad (2.2) \\ & = w_o^2 A_d \cos(w_d t) \end{aligned}$$

The solution of this equation is formed by two part: the steady-state solution and the transient solution. The first part is calculated if the external force that excites the system is equal to zero, thus resolving the homogeneous differential equation. The second is depending on time and it has sinusoidal form, with a decreasing amplitude for  $t > 0$  and it is due to the damping factor.

$$z(t) = A_o \cos(w_o t + \varphi) + A_d e^{\frac{-w_o t}{2Q}} \sin(w_o t + \varphi_d) \quad (2.3)$$

For the first term of the solution of the differential equation, the amplitude and the phase of the oscillation can be evaluated. Because of the presence of the damping factor, the resonant frequency is not equal to  $w_o$  but it is closer to the resonant frequency at free oscillation. We can denote it as  $w_r$ .

$$A_o = \frac{A_d Q w_o^2}{\sqrt{w_r^2 w_o^2 + Q^2 (w_o^2 - w_r^2)^2}} \quad (2.4)$$

$$\varphi = \arctan \frac{w_r w_o}{Q (w_o^2 - w_r^2)} \quad (2.5)$$

It is evident that the Quality factor determines that the maximum value of amplitude is reached at  $w_r$  and, considering that the damping factor is antiproportional to  $Q$ , a relationship between the frequencies and the quality factor can be established.

$$w_r = w_o \sqrt{1 - \frac{1}{2Q^2}} \quad (2.6)$$

The quality factor is around 100-1000 for vacuum air applications and is smaller in AFM in liquid environments.

## 2.2 Resonance frequency for rectangular cantilever

The dynamic response of a microcantilever is characterized by three fundamental factors: spring constant, resonant frequency and quality factor.

Cantilever is studied as a continuous system and mass is not punctual but distributed. The Eulero-Bernoulli equation is the equation of motion used to describe its behavior<sup>18</sup>.

$$EI \frac{\partial^4 w}{\partial x^4}(x, t) + \mu \frac{\partial^2 w}{\partial x^2}(x, t) = F_{ext} \quad (2.7)$$

Where  $E$  is the Young modulus of the beam,  $I$  is the moment of inertia,  $w$  is the displacement in z-axis and this distance is calculated with respect to the beam's free end,  $\mu$  is mass per unit of length of the cantilever. This equation is equal to a force applied outside and it contains all the forces on the tip per unit of length.

Introducing the boundary condition to the system, it is easier to resolve it and to calculate all the terms of our interest.

If the frame reference is jointed to the fixed end of the cantilever, as described in Fig.11, we can say that, for  $x=0$  the displacement and the first derivative of the displacement are

equal to zero, for  $x=l$ , at the free end of the cantilever, the second and the third derivative of the displacement are equal to zero.

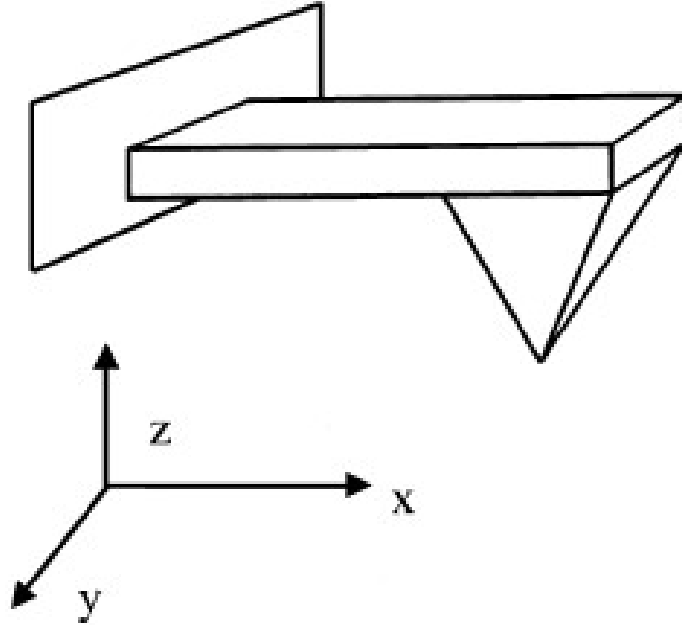


**Figure 12 Schematic of cantilever-tip system in 3D. Picture taken from *Dynamic atomic force microscopy and methods*, R. Garcia**

The normal force constant is defined as the ratio between the force applied and the spring displacement along the same direction. With the introduction of E-B equations, a relation between the cantilever stiffness and its geometry has been found. For this reason, for a vertical bending of the beam, a new equation can be written<sup>19</sup>:

$$k = \frac{3E I}{L^3} = \frac{E W h^3}{L^3} \quad (2.8)$$

Where  $L$  is the cantilever length,  $W$  is the width and  $h$  is its thickness. This equation can be applied for a beam with a rectangular shape.

Now it is possible to calculate the resonance frequency according to this formula:

$$f_o = \frac{1}{2\pi} \sqrt{\frac{k}{m}} = \frac{1}{2\pi} \sqrt{\frac{E}{\rho}} \frac{h}{L^2} \quad (2.9)$$

Where frequency is expressed in Hz and all the dimensions are in the order of microns.

This model was formulated by Sader, in which he considers cantilever thickness and density to estimate the mass. These formulas are used when  $l/h \gg 1$ , so cantilevers should be very thin.

Another equation has been introduced through Cleveland's experiments, performed in a fluid environment, typically in the air. The spring constant is related to air properties, as we can see below:

$$k = 0.1906 p_f w^2 l Q r(w_f) w_f^2 \quad (2.10)$$

Where  $p_f$  is the air density,  $w$  and  $l$  are the width and the length respectively,  $w_f$  is the resonance frequency and  $r(w_f)$  is the imaginary component of the hydro-dynamic function. It can be estimated in relation to Reynolds number<sup>20</sup>:

$$Re = \frac{p_f w^2 l}{4\eta} \quad (2.11)$$

Where  $\eta$  is the viscosity of the air. Reynold number and the hydro-dynamic function are related as the plot figured below, where the real and the imaginary component are shown in solid line and in dashed line, respectively.

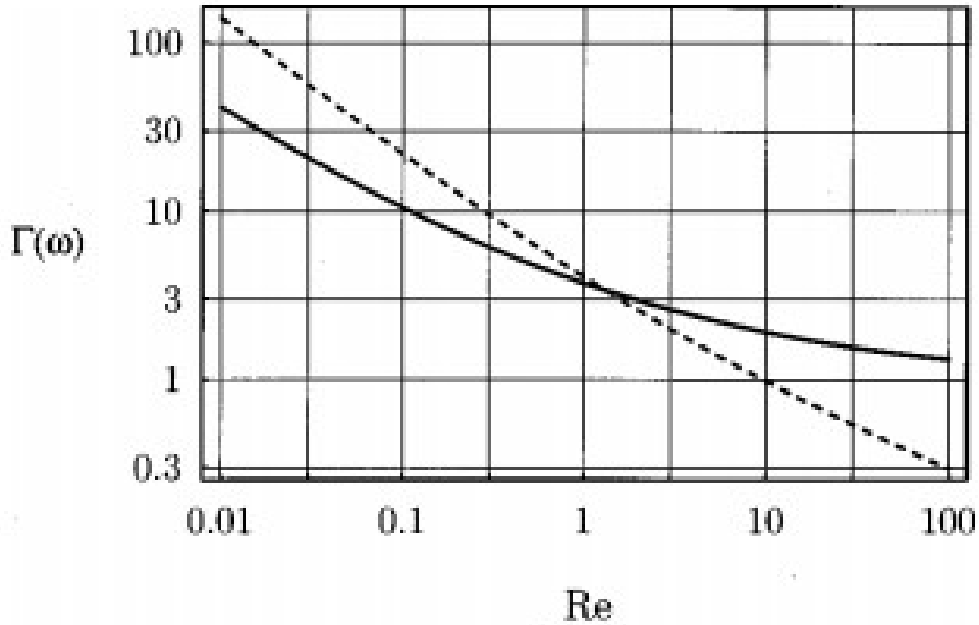


**Figure 13** Plot relating the real and imaginary hydro-dynamic function to Reynolds number. Picture was taken from "Calibration of rectangular AFM", Sader

This method proposes a direct relation between the spring constant of the cantilever and the Quality factor. This dimensionless parameter is generally defined as the ratio between the energy stored and the energy dissipated per cycle during cantilever oscillation. The first term is identified as the sum of the potential and kinetic energy and the lost quantity is generated by an external force. In AM-AFM analysis it allows to keep the amplitude constant.

In the specific case of resonant oscillations, the energies can be expressed as function of the frequencies and it introduces another definition of Quality factor:

$$Q = \frac{w_r}{\Delta w} \quad (2.12)$$

$\Delta w$  is defined as bandwidth, given by the difference between two frequencies very close to the resonant frequency and calculated when the amplitude oscillation is equal to the root mean square of the maximum value of the same amplitude.

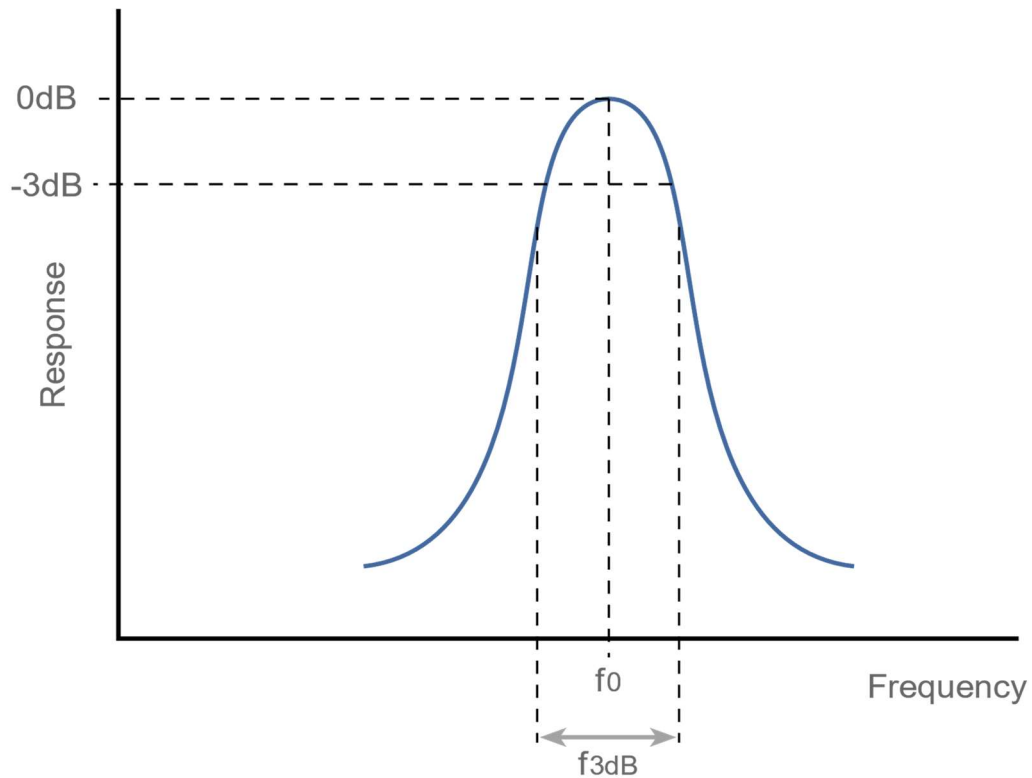


*Figure 14 Graphic interpretation of the Quality factor as function of bandwidth. Picture taken from Electronicnotes website*

## 2.3 Hertz theory

When the AFM tip scans a sample, such mechanism involves a contact between these two bodies. At first, it was thought that the contact manifested is punctual, but this hypothesis is true only if both the tip and the surface are modeled as rigid. Indeed, they undergo a local deformation, and the contact area is not a point but a very small surface. It means that the pressures due to the contact are too high and in the proximity of this contact area a state of tri-axial tension-compression has developed. This pressure varies according to the bodies' geometry and elastic modulus.

Heinrich Hertz studied a theory based on contact mechanical, in which he outlines all the problems related to the elastic deformation and resolves these problems in terms of pression distribution, contact radius and state of tension.

Hertz describes what happens when two bodies touches in the same point under compression, finding out that the problem is nonlinear, as explained by the relation

between force and depth penetration.

There is some various hypothesis behind it:

- Surfaces are smooth and continuous, described by equations of the second order. Any type of defects that affects the distribution of pressure on the surfaces are neglected.
- Bodies are homogeneous and isotropic.
- Deformation is elastic and follows Hook's law.
- Deformation is too small.
- Contact radius is smaller than bodies' radius of curvature.
- Surfaces in contact are without friction.

In this dissertation we analyze the deformation of mica and TMV. So, a mathematical model will be introduced, pointing out the contact between a sphere and an elastic half-space<sup>21</sup> for mica's deformation and the contact between a sphere and a cylinder for TMV's deformation.

The first step of Hertz's theory consists of determining a method to calculate the shape of area contact. Let us consider a spherical surface  $S_1$  tangent on a plane  $A_1$  at a point  $P$ .

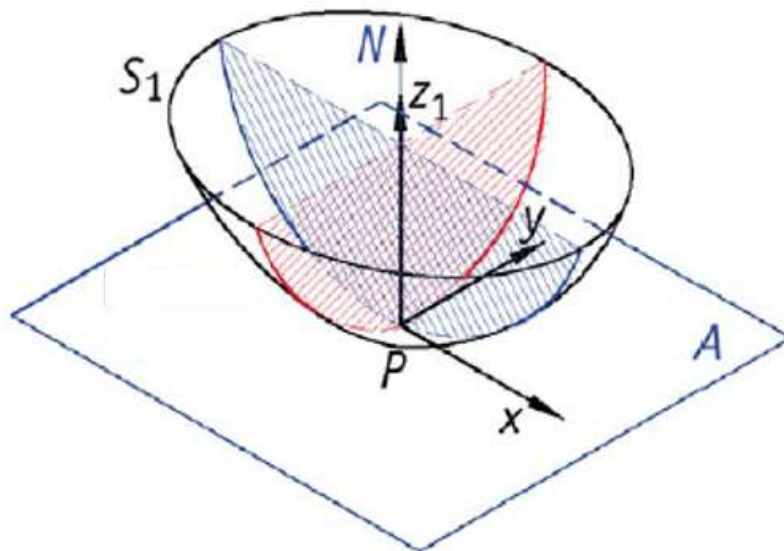


**Figure 15 Representation of contact between surface and plane.**

They can be modeled according the following equation:

$$z = \frac{1}{2} [a_{11}x^2 + 2a_{13}xy + a_{12}y^2] \quad (2.13)$$

Where  $a_{11}$  and  $a_{13}$  are respectively the curvature of the section x-z<sub>1</sub> and y- z<sub>1</sub> in P, in particular:

$$a_{11} = \frac{1}{R_{11}} \quad (2.14)$$

$$a_{12} = \frac{1}{R_{12}}$$

$R_{11}$  and  $R_{12}$  are the maximum and the minimum curvature radius according to the principal coordinate reference system. In this case,  $a_{13}$  is equal to zero and (2.14) can be re-written as below:

$$z = \frac{1}{2} \left[ \frac{1}{R_{11}}x^2 + \frac{1}{R_{12}}y^2 \right] \quad (2.15)$$

$$z = \frac{1}{2} [\rho_{11}x^2 + \rho_{12}y^2] \quad (2.16)$$

Let us consider another surface  $S_2$  tangent on a plane  $A_2$ . It is noticeable that the planes coincide, but the reference systems of the surfaces are different. Taken two points A and B, belonging respectively to  $S_1$  and  $S_2$ , their distance is calculated in a new oriented reference system. Thus, it is possible to derivate the following equation<sup>22</sup>:

$$2h = 2AB = [Cx'^2 + Dy'^2] \quad (2.17)$$

Where C and D are the coefficients of the area contact between the surfaces.

C and D are determined with respect to curvature radius  $\rho$ :

$$C + D = \rho_{11} + \rho_{12} + \rho_{21} + \rho_{22} \quad (2.18)$$

$$C - D = \rho_{11} + \rho_{21} - (\rho_{12} + \rho_{22}) \quad (2.19)$$

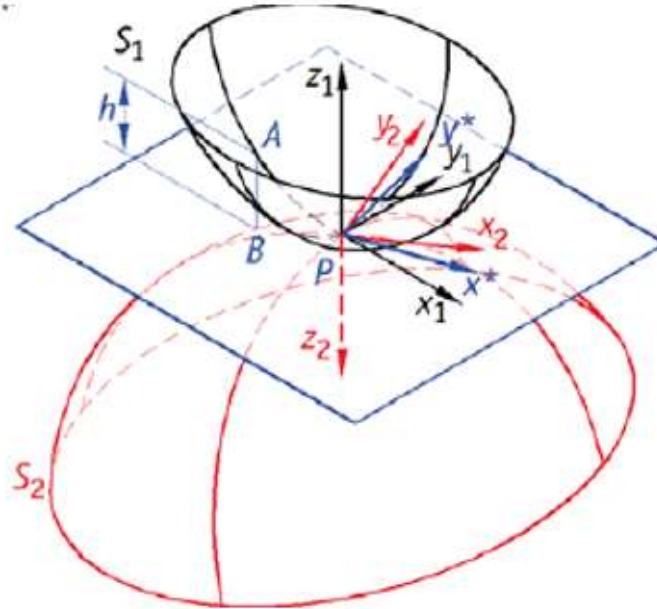


**Figure 16** Two surfaces in contact at point P.

The first subscript of curvature radius refers to the surface  $S_1$  or  $S_2$  in Fig.16, the second subscript is used to indicate the maximum and the minimum curvature radius according to the principal coordinate system reference. The ratio between (2.19) and (2.20) equations is equal to an angle, through which the coefficients  $\alpha$  and  $\beta$  are determined. Their value can be estimated through the table in Fig.17.

$$\cos\tau = \frac{C - D}{C + D} \quad (2.20)$$

The maximum semi-axis and the minimum semi-axis are so calculated:

$$a = \alpha q, \quad b = \beta q, \quad q = \sqrt[3]{\left(\frac{3}{2}\right) \left(\frac{F}{E' \cdot \Sigma \rho}\right)} \quad (2.21)$$

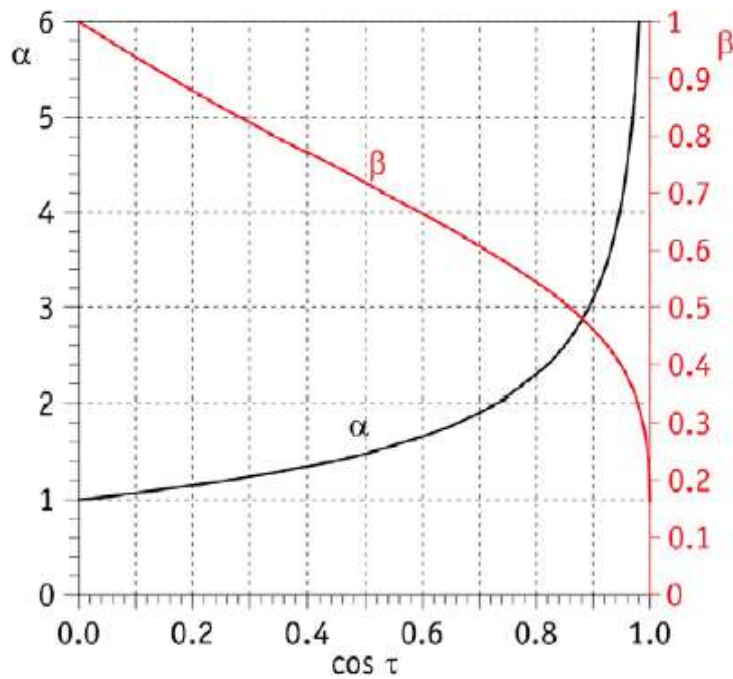


**Figure 17** Curves of  $\alpha$  and  $\beta$  with respect to  $\tau$

Some particular cases of Hertz theory are summarized in the following table:

<i>Cases</i>	<i>C</i>	<i>D</i>	<i>Area contact shape</i>
<i>Sphere-sphere or sphere-plane</i>	$\geq 0$	$\geq 0$ and equal to <b>C</b>	<b>spherical</b>
<i>Cylinder-cylinder or cylinder-plane</i>	$\geq 0$	<b>= 0</b>	<b>rectangular</b>
<i>Sphere-cylinder</i>	$\geq 0$	$\geq 0, \neq C$	<b>elliptical</b>

**Table 1** Description of area contact shape according to some particular cases

Now, let us consider the Hertzian contact between sphere and a semi-elastic plane.

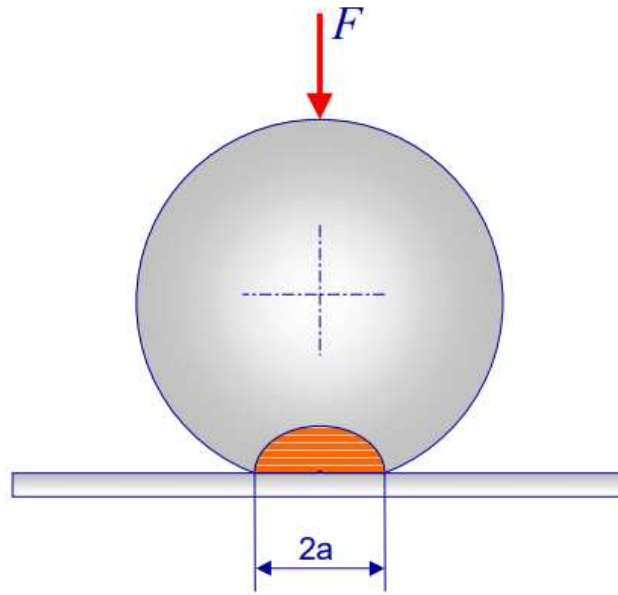


**Figure 18 Hertzian contact between sphere and elastic half-space. Picture taken from Norton, 2008**

As depicted in Fig.14, the contact between these two bodies generates a contact surface. The force applied is:

$$F = \frac{2}{3} \pi a^2 p_{max} \quad (2.22)$$

Where  $a$  is the dimension of the surface of contact,  $p_{max}$  is the maximum pressure exerted by the compression. From (2.22), the formula for the maximum pressure can be obtained and compared with the average pressure, as follows:

$$p_{max} = \frac{3}{2} \frac{F}{\pi a^2} \quad (2.23)$$

$$p_{med} = \frac{F}{\pi a^2} \quad (2.24)$$

$$p_{max} = \frac{3 p_{med}}{2} \quad (2.25)$$

The area of contact will be rectangular, with its dimension equal to:

$$a = \sqrt[3]{\frac{3FR}{4E'}} \quad (2.26)$$

Where  $E'$  is the reduced Young's modulus and  $R$  is the effective radius of the bodies:

$$\frac{1}{E'} = \frac{1 - \nu_1^2}{E_1} + \frac{1 - \nu_2^2}{E_2} \quad (2.27)$$

$$\frac{1}{R} = \frac{1}{R_1} + \frac{1}{R_2} \quad (2.28)$$

With  $E_1, E_2, \nu_1, \nu_2$  being the Young's modulus and the Poisson ratio for the bodies, and  $R_1, R_2$  the radius of each body in contact. The second of them is a plane, or in other words a sphere with  $R_2 \rightarrow \infty$ . It implies that  $R = R_1$ .

Another very important parameter to study is the penetration depth,  $h$ . It indicates how much the surface is deformed under compression. This factor is in relation with the pressure distribution on the surfaces in contact. In the case of cylinder - half space, the calculation has been simplified by approximating the pressure on the contact surface as constant. This implies that the relation between the force and the penetration depth is almost linear. For sphere-sphere contact, the force is 3/2-proportional to the deformation. Generally, if the surface is nearly 1-dimensional, the relation will be  $F \propto h^2$ . So, we can conclude that, for Hertzian contact sphere-plane, the deformation  $h$  is expressed as below<sup>23</sup>:

$$h = \frac{a^2}{R} \quad (2.29)$$

## 2.4 Importance of adhesion at the nanoscale

In the last decades, tribology studies became something of collective interest, involving all the researchers and scientific community to resolve all the problems related to failed components and to optimize product performances at the macroscale. There were some attempts to bridge the nanoscale adhesion data to the macroscale data, without any good results. Nevertheless, tribology studies are addressed to a possible application of contact mechanics, including adhesion and friction properties, to establish how the atomic and the nanoscale interaction change when two surfaces are in contact<sup>24</sup>.

Particularly, AFM experiments were conducted to measure adhesion through the behavior of the cantilever tips when a pull-off force is exerted.

When we investigate the world of nanoparticles, the work of adhesion acquires an important rule, because it is not a quantity to neglect and it can affect mechanical properties at the macroscale. For instance, computer hard disk and bearings need of a minimum energy of adhesion to have good performances, or micromechanical devices should be controlled until they work well. Work of adhesion is related to the surface energy and its value is related to the solid/liquid surface in contact when a pressure is applied.

In 1932, Bradley resolved the problem of work of adhesion, modifying the Hertz theory between rigid spheres, but the first elaborate in which its value was calculated dates back to 1971, when Johnson demonstrated what happens if energy surface is considered in the contact between elastic bodies.

At the same time, another formulation of the same concept was idealized by DeJaguin in 1975, that differs from Johnson by the different region in which intermolecular adhesion is considered.

Two years later, Tabor introduced a new parameter, renamed as his person, in order to find a compromise between the two theories explained, realizing that both the discoveries are true and valid for different cases<sup>25</sup>.

The main molecular interaction that describes the work of adhesion are listed as below:

- London dispersion interaction
- Dipole-dipole interaction
- Induction orientation
- Hydrogen bond
- Donor-acceptor bond
- Electrostatic interaction

The sum of the first three contributes give the work of Van der Waals force. Indeed, when we define the potential given by adhesion, the most effectively contribute is due to the Van der Waals force, that allows to determine at what distance the attractive intermolecular forces become repulsive and the tip deflects backwards during AFM probe, and to electrostatic interaction.

## 2.5 Johnson Kendall Roberts Model (JKR)

JKR model was introduced in 1971 and it differs from Hertz theory because of the inclusion of adhesion. It is typically applied for compliant tips and large curvature radius. For this reason, the area of contact is larger than that studied by Hertz and it will be never equal to zero when the bodies are not compressed. It is determined by a balance between lost energy and stored energy.

For the case sphere – semi-elastic half space, the dimension of rigid sphere<sup>26</sup> can be calculated as follow:

$$a_{JKR}^3 = \left(\frac{3R}{4E'}\right) [F + 3\pi\Delta\gamma R + (6\pi\Delta\gamma RF + (3\pi\Delta\gamma R)^2)]^{\frac{1}{2}} \quad (2.30)$$

Where  $\Delta\gamma$  is the work of adhesion ( $J/m^2$ ) and  $F$  is the force calculated by Hertz. The part of the equation in the brackets is equal to the force estimated by Johnson, Kendall and Roberts,  $F_{JKR}$ .

The penetration depth also changes with respect to Hertz model and it is equal to:

$$h_{JKR} = \frac{a_{JKR}^3}{R} - \left(\frac{2}{3}\right) \left[ \frac{6\pi\Delta\gamma a_{JKR}}{\left(\frac{4}{3}\right) E'} \right]^{\frac{1}{2}} \quad (2.31)$$

Thus, the force depends on the work of adhesion, the curvature radius and the elastic modulus. JKR theory accounts for short-ranged adhesion force inside the contact area. The only limitation of this model is due to a possible underestimation of loading.

This method was modified and applied for the contact sphere-cylinder<sup>27</sup>. The equations are quite like those determined for sphere-sphere contact, but they differ for geometrical properties of the bodies. The radius of the area and the penetration depth are described as below:

$$a_{JKR}^3 = \left(\frac{R}{E'}\right) [F + 6\pi\Delta\gamma R + (12\pi\Delta\gamma R F + (6\pi\Delta\gamma R)^2)]^{\frac{1}{2}} \quad (2.32)$$

$$h_{JKR} = \frac{a_{JKR}^2}{R} - \left[ \frac{8\pi\Delta\gamma a_{JKR}}{3E'} \right]^{\frac{1}{2}} \quad (2.33)$$

## 2.6 Derjagin, Muller, Toropov (DMT Model)

DMT model was formulated four years later than JKR Model (1975). It is applied for systems characterized by tips with high stiffness and small curvature radius. It differs from JKR model because the Van der Waals force is applied outside the contact area.

The contact radius given by DMT is related to the work of adhesion according to the following equation:

$$a_{DMT}^3 = \left(\frac{R}{E'}\right) [F + 2\pi\Delta\gamma R] \quad (2.34)$$

$$h_{DMT} = \frac{a_{DMT}^2}{R} \quad (2.35)$$

The term in the brackets is equal to the force according to DMT model and the critical force to separate the spheres is equal to  $2\pi\Delta\gamma R$ .

Some researchers are trying to study how to apply DMT model for different shapes. In this paper, the cylinder is approximated to a sphere at the nanoscale in order to estimate all the parameters required by the model.

## **2.7 Description of the instruments for INRiM experimentation**

The experimental test carried out in INRiM consists of the acquisition of images of the sample, analyzing its mechanical characteristics and cantilever properties.

The atomic force microscope is located inside an underground tunnel (building 8). Temperature and humidity conditions at which the experimental tests are carried out are important: the environment has been made completely isothermal, at a temperature of 20°C, and the air humidity is around 40-50%. Furthermore, the walls are made in such a way to reduce the effect of noise to zero and the table on which the AFM system is placed is anti-vibrating. Therefore, it is very important to take note of all these precautions to get good results in the tests.

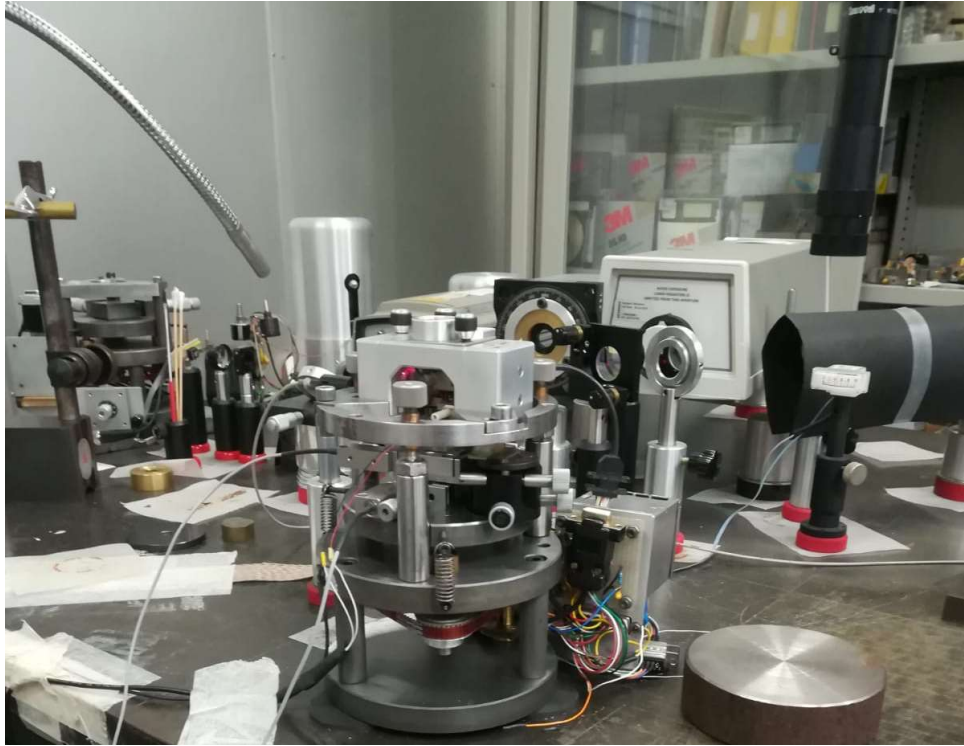


***Figure 19 Illustration of AFM Metrological in INRiM***

The metrological atomic force microscope used to work in tapping mode. At the base there is a mechanical support consisting of two discs connected to each other by cylindrical pillars, on which the piezoelectric scanner rests. It was built in INRiM and it guarantees the metrological loop. On the shaft of the electric motor, behind the microscope, a toothed wheel is keyed, and its operation involves the transmission of motion to a pulley system. The sliding of the belt is responsible for the vertical displacement of the scanner, determining the approach and the retract of the sample to the cantilever tip. A closed loop for piezoelectric scanner position is made in INRiM. The typical substrate for the sample is mica or HOPG. They are easily peeled and suitable for supporting polymers, fabrics and virus particles. The Multimode AFM head, made by Veeco, incorporates two photodiodes, through which it is possible to trace the movement of the scanner along two directions, x and y, and contains the cantilever whose tip is made of silicon or silicon nitride.

The precision and accuracy of the measurement are two fundamental characteristics that, if studied and adjusted correctly, allow you to obtain a better resolution of the image obtained from the scan.

Therefore, a He-Ne (helium-neon) laser tube is arranged outside the microscope structure, which emits a light beam operating at wavelength of 632.8 nm, i.e. red of the visible

spectrum. In the ignition phase, it needs at least 20-30 minutes for the emitted beam to stabilize and to make measurements as accurate as possible. The axis control is made in INRiM and it needs to trace all the measurements for SI.

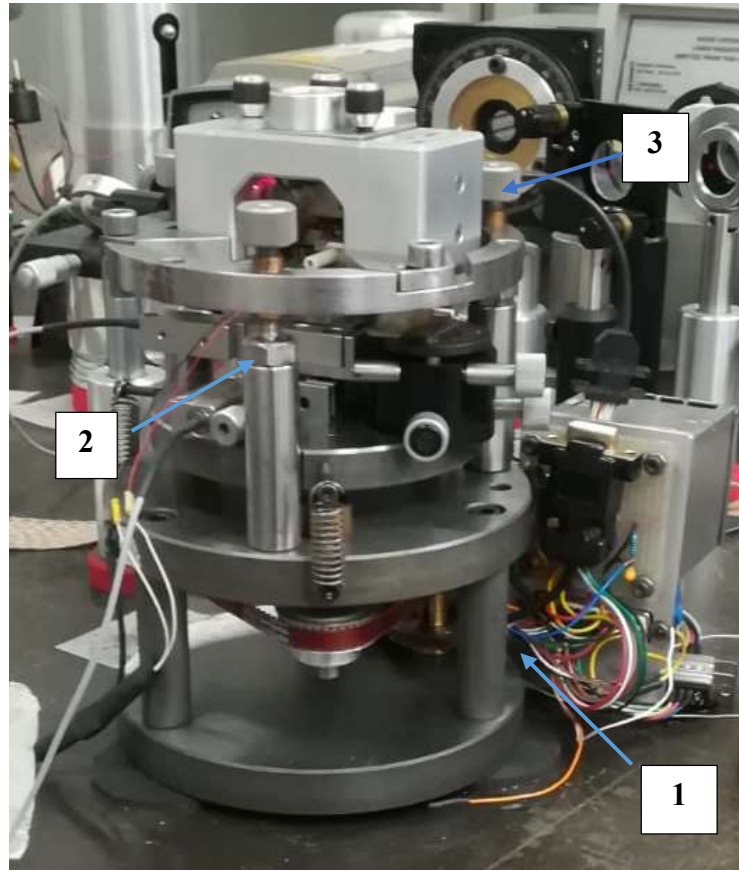


**Figure 20 Zoom of the AFM Metrological: 1. support, 2, PZT scanner, AFM head (where the cantilever and the photodiode are placed)**

The scanner is very sensitive to displacements along the three directions, so the Michelson interferometer was added to the system. The light rays coming from the laser source can interfere in the constructive way if the waves are in phase or in the destructive phase if the waves are in opposite phase. In this way it is possible to calculate the displacement with respect to the wavelength beams. Near the laser tube there is a reference photodiode: the light beam emitted by the tube is reflected by a beam splitter towards this detector. In this way, the initial wavelength of the laser is determined and is possible to define the movement of the scanner along x and y. Another beam splitter is located in order to split the light beam in two directions perpendicular to each other. Both of them meets a polarized beam splitter, determining other two paths: one of them is directed to the

detector for x (or y) displacement, the other goes to the sample order, that connect the interferometric system to the electronic control to get the signals and built by A.P.E. Research. At the end, the beams tend to converge again.

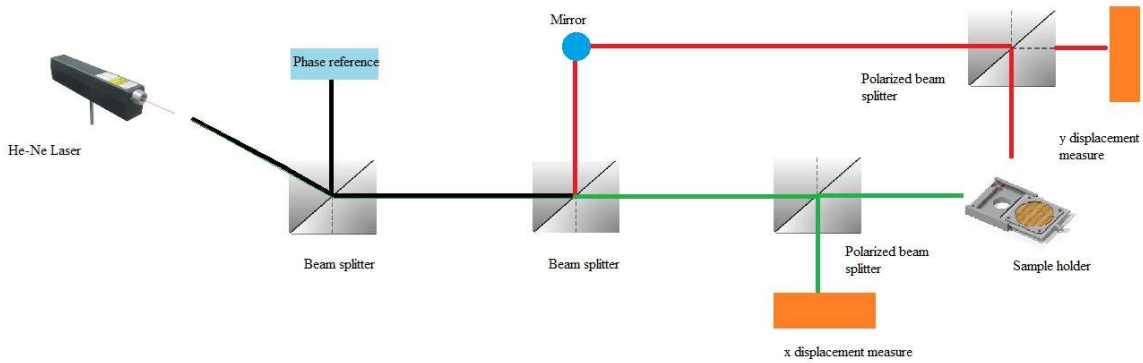


**Figure 21 Schematic of AFM interferometer**

All the measurements done are possible by means of a metrological loop, which set-up is made by a piezoelectric loop control system and an electronic control of interferometric signals. The first of them is very important for nano positioning applications and it must guarantee the absence of vibrations, noise and thermal drift during metrological loop. It can be regulated manually by switching a lever, determining if the probing of surfaces is done in open loop or in closed loop. The electronic control of interferometric signals gives more accuracy of the line positional measurements. The interference fringes are detected and converted into electronic signals, in order to give more information about tip position with respect to the sample.



*Figure 22 Piezoelectric control loop made in INRiM*

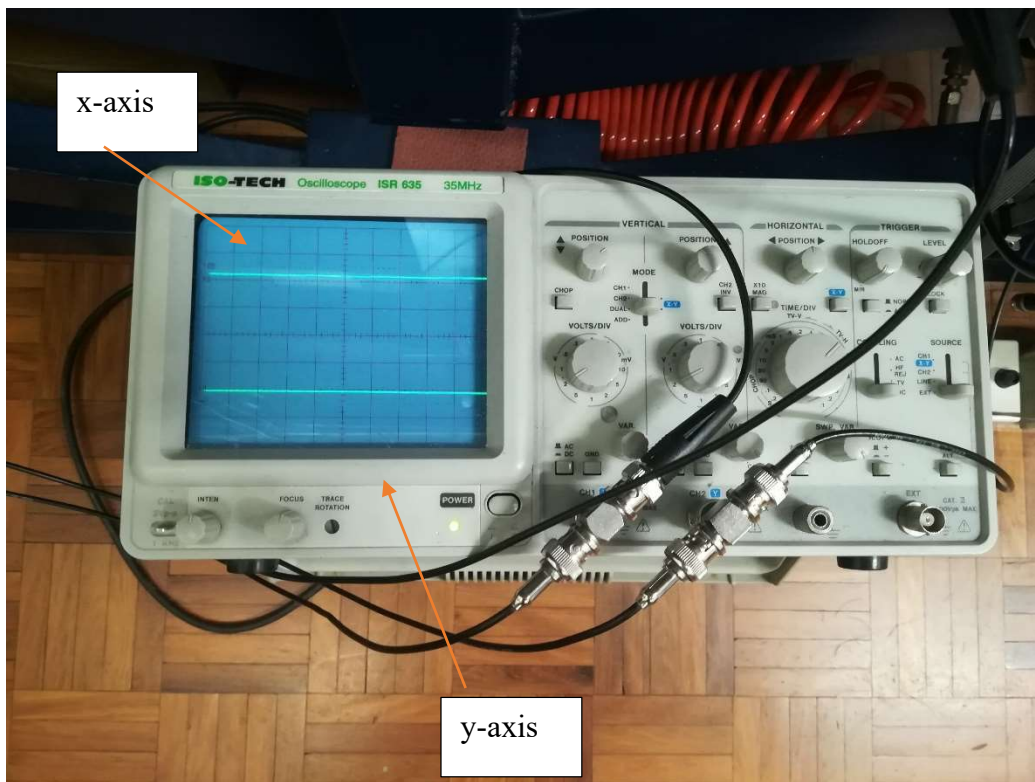


*Figure 23 Oscilloscope. It shows how the cantilever tip moves along x and y direction*

During AFM imaging, the tip moves along x-axis and jumps line to line along y-direction and all the positions occupied are displayed on an oscilloscope. It should be reset for each measurement so that the voltage signals are observed as a waveform of the screen at the right position.

# 3 Results

## 3.1 Tests procedure and analysis of Q-factor

In this chapter we will expose all the results obtained by experimental tests, in order to show the main mechanical properties of the nanostructure and to understand how to regulate a metrological AFM for the data acquisitions. For this purpose, different types of cantilevers are used, to check if a good repeatability of results for each test is guaranteed and how it is possible to determine such properties in non-contact mode. In the next chapter, all the results will be discussed.

Before starting the test, all the cantilevers are observed under a microscope and each of them should be on the top side of the strip, while the saw cuts are in the opposite side from the cantilever. After breaking-off the cantilever substrates, the next step consists of inspecting them under an optical profilometer. Each substrate provides two cantilevers on each end. This phase is important to remove the unused cantilever from that substrate. After doing this, the cantilever is placed on the tip holder and mounted into the head of the metrological AFM. This is a very delicate step of the experimental tests: it is very important that the spot laser hits the rear of the cantilever, in the same position where the tip is located. A subsequent calibration of the spot laser sets the zero position of the photodiode.

The cantilever can be classified according the mode it works:

- Non-contact cantilever
- Contact cantilever

The first of them has been just tested by INRiM. The tip of the cantilever oscillates at resonant frequency. In the metrological AFM it is set by the user through the tool “Resonance”. It has been used to trace the curve that describes how amplitude varies as function of frequency, so calculating the resonant frequency. This tool allows to set the

value of reference voltage.

The novelty of these tests done in INRiM consists of trying to use the contact cantilever in AFM non-contact, useful to make a comparison of their results with non-contact cantilever's data analysis. For this case, the resonant frequency is not searched, but imposed by the user because the cantilever does not oscillate.

These beams can be classified according their geometry in:

- Rectangular cantilever
- V-shaped cantilever

Cantilevers used for the experimentations are listed in the following table.

<i>Type of cantilever</i>	<b>Model</b>	<b>Made by</b>	<b>Stiffness k (N/m)</b>	<b>Date</b>	<b>Geometry</b>
<i>Non-contact</i>	HQ:NSC14/AL BS	Mikromasch	5	08/10/2020	Rectangular.
<i>Non-contact</i>	HQ:NSC15/AL BS	Mikromasch	46	20/10/2020	Rectangular
<i>Contact</i>	NP-20 n.13	Veeco	0.12	13/10/2020	V-shaped
<i>Contact</i>	NP-20 n.3	Veeco	0.12	21/10/2020	V-shaped
<i>Contact</i>	NP-20 n.3	Veeco	0.58	21/10/2020	V-shaped
<i>Contact</i>	HQ:CSC17/AL BS	Mikromasch	0.18	22/10/2020	Rectangular

**Table 2 List of the cantilevers used for Metrological AFM**

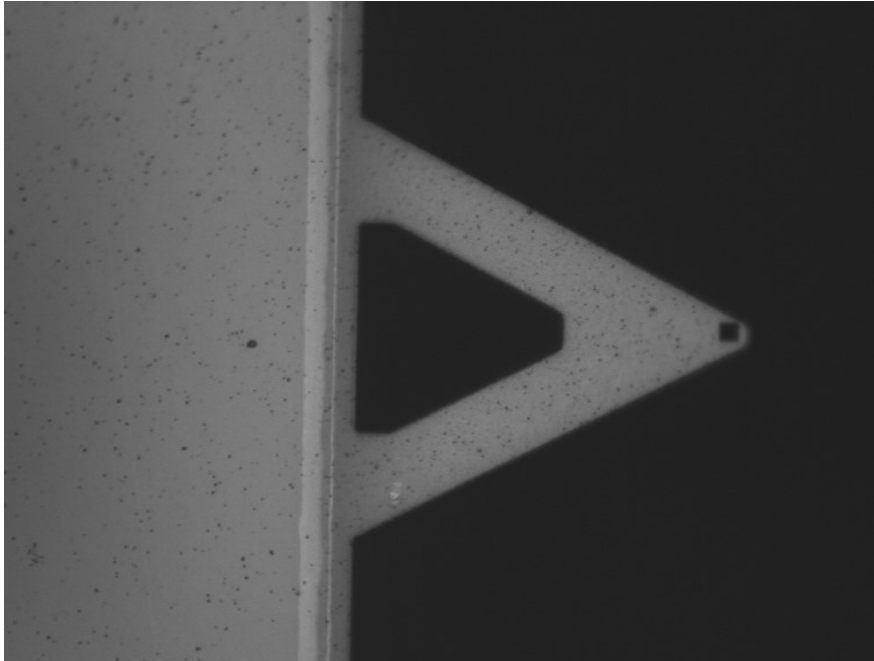


***Figure 24 Cantilever NP-20 n.3 made by Veeco, spring constant  $k = 0.58$  N/m, seen through optical profilometer Sensofar PLu2300, confocal mode with 20x magnification, 21/10/2020. The black square in the picture corresponds to the cantilever tip.***

After calculating resonant frequency, the laser is aligned: the user moves the laser beam relative to the cantilever, by turning the control knobs (located on the head of the AFM) clockwise. Each of them regulates laser beam along x and y direction, and this procedure can differ according to the probe tip geometry. All the detectors of the Michelson interferometer have to show the maximum gain to read the interferometric signals with more accuracy. The alignment acquires an important rule for metrological AFM because the displacements are referable to SI. Red light laser is adjusted with respect to the wavelength national primary standard laser. Then, the phase meters are cleared, the tip is approached to the sample regulating the electric motor speed and the loop is closed. All the AFM systems is covered by a glass cage to reduce the noise and the vibration from the outside and imaging and data acquisition can start.

The electric control system loop acts in different way according the cantilever tip mode. In non-contact tip, a reference voltage is set in “Reference tool”, and when the oscillation amplitude, expressed in voltage, becomes lower than the referable value, the feedback system leads the tip far away from the sample surface. Thus, damages to the metrological AFM are avoided.

In contact cantilever tip, the cantilever deflection is set during AFM calibration. When its value is less than that imposed by the user, the loop control systems brings the entire system in safety.

Mikromasch and Veeco generally provide information about the nominal value of the tip geometry, stiffness and resonance frequency. The first part of the experimental test verifies if the resonance frequency corresponds to its nominal value and determine the real geometry of the tip. The models used are described in the next chapter (Eulero-Bernoulli Method and Reynolds Method) are then compared with the experimental result obtained by the AFM tool. This method is applied only for non-contact AFM for the reason explained in the previous paragraph.

Tables 3 and 4 depicts the results obtained applying both the methods, thus defining cantilever geometry and its Q-factor, table 5 contains their experimental values.

			<b>Tests Date</b>	
<b>Eulero-Bernoulli Method</b>			<b>08/10/2020</b>	<b>20/10/2020</b>
<b>Resonance frequency</b>	rad/s	$w_r$	1005310	1984544
<b>Spring constant</b>	N/m	<b>k</b>	<b>5</b>	<b>46</b>
<b>Cantilever length</b>	$\mu\text{m}$	L	134	133
<b>Width ext</b>	$\mu\text{m}$	B	25	33
<b>Cant density</b>	kg/m <sup>3</sup>	$p_c$	2338,3	2338,3
<b>Young modulus</b>	GPa	E	190	190
<b>Thickness</b>	m	t	1,99	3,90
<b>Natural frequency</b>	rad/s	$w_o$	1005313	1984545
<b>Q factor</b>		<b>Q</b>	<b>279.5</b>	<b>781.4</b>

*Table 3 E-B equation for Q-factor*

			<b>Tests Date</b>	
<b>Reynolds method</b>			<b>08/10/2020</b>	<b>20/10/2020</b>
<b>Resonance frequency</b>	rad/s	$w_r$	1005310	1984544
<b>Air dynamic viscosity</b>	kg/ms	$\mu$	1,86E-05	1,86E-05
<b>Cantilever length</b>	$\mu\text{m}$	L	134	133
<b>Width ext</b>	$\mu\text{m}$	B	25	33
<b>Air density</b>	kg/m <sup>3</sup>	$p_{air}$	1,23	1,23
<b>Reynolds number</b>	-	Re	10.4	35,7
<b>Imaginary part of hydrodynamic function</b>	-	imm	0,89	0,44
<b>Spring constant</b>	N/m	<b>k</b>	<b>5</b>	<b>46</b>
<b>Q factor</b>	-	<b>Q</b>	<b>284</b>	<b>782</b>
<b>Cantilever material</b>			Silicon Nitride	

*Table 4 Q-factor with Reynolds*

Experimental value	Q-factor
Date: 08/10/2020	289
Date: 20/10/2020	790

*Table 5 Experimental Q-Factor*

As just discussed previously, the table above is a result of the searching of resonant frequency done through “Resonance tool”. It finds the peak of the curve, to which the resonance frequency corresponds, and the quality factor is calculated as the ratio between this value and its bandwidth.

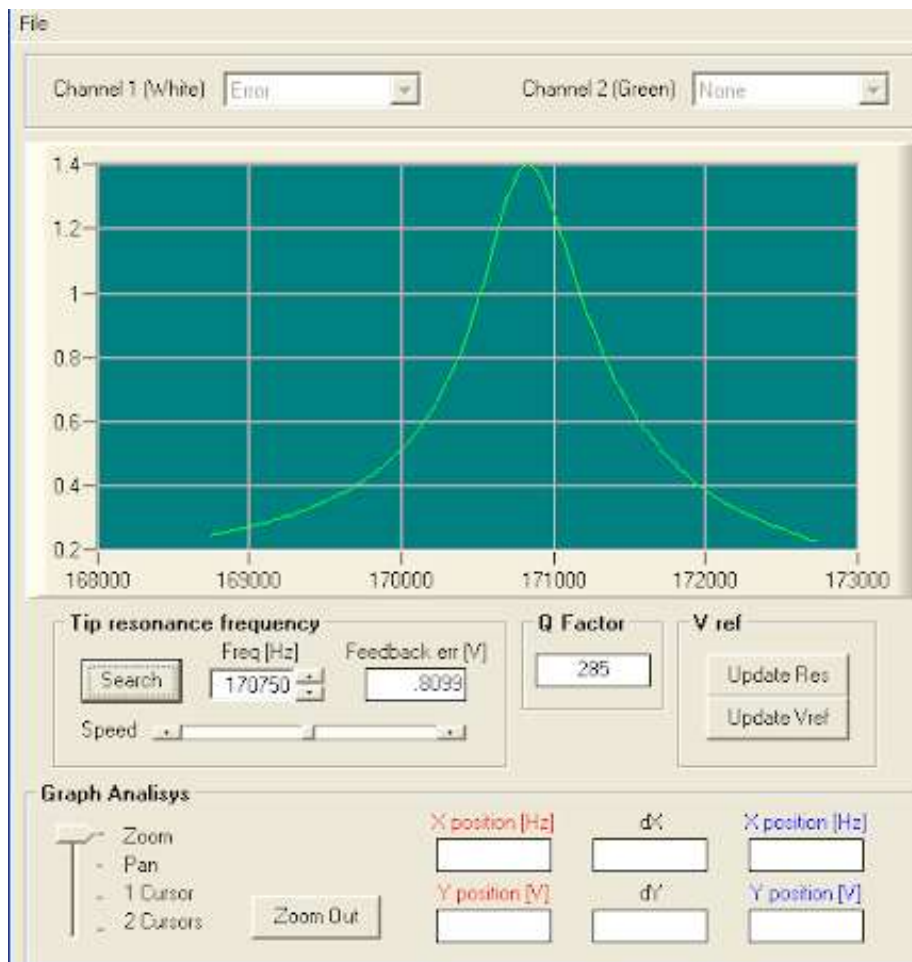


*Figure 25 Display of resonance search through "Resonance tool"*

## 3.2 Amplitude oscillation tests

After AFM calibration, the behavior of the tip amplitude oscillation has been studied when the applied Z-offset piezoelectric varies. It provides information about the tip cantilever behavior when it leaves its rest position. This procedure has been made manually, varying the voltage from -10 V to +10 V with a step of 0.5 V. This voltage range is converted into the stroke of the piezoelectric when it approaches, and then retracts with respect to the sample, knowing that it is equal to  $2\mu\text{m}$ . Thus, when the voltage is equal to -10 V, the piezoelectric is at the maximum distance with respect to the cantilever tip, when the voltage is 10 V, the piezoelectric is closer to the tip cantilever, without contact. The ratio between the voltage range and the piezoelectric stroke is  $98\text{ nm/V}$ .

These measurements done in INRiM are repeated three times in order to verify the degree of repeatability of the tip amplitude oscillations in the approaching phase and in the retracting phase. It was applied for mica and TMV, zooming some areas of interests from the surface topography. These procedures were followed for both non-contact and contact cantilever tip and in the next tables the results of these tests are depicted.

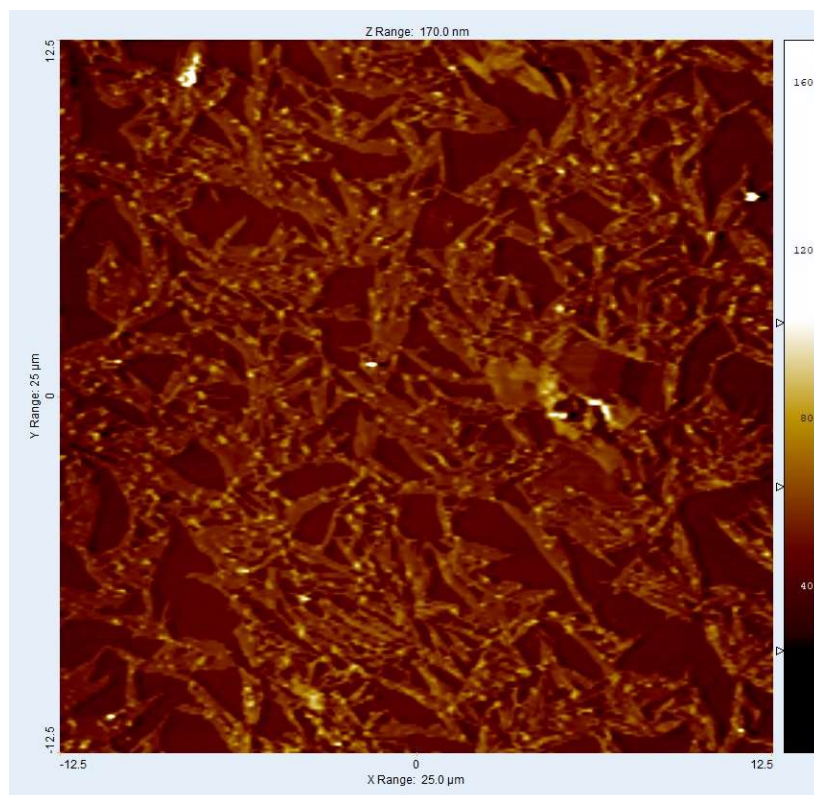


*Figure 26 Picture of TMV sample topography. Size 25000nm, 256x256 pixel, 250 nN*

and spring constant equal to 0.12 N/m

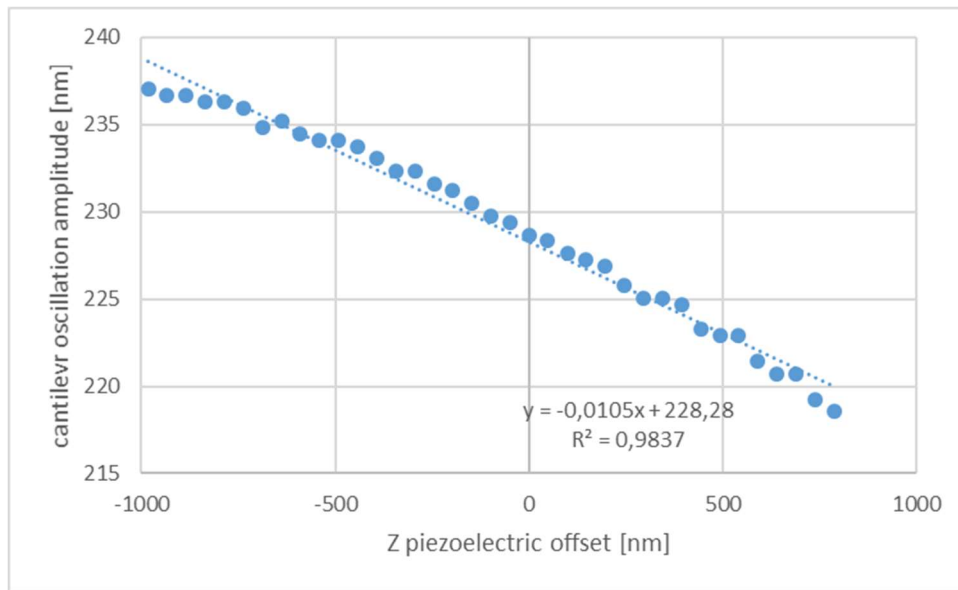


**Figure 27** Variation of the tip amplitude oscillation vs Z-piezoelectric offset for TMV in the approach phase with cantilever stiffness 5 N/m. Non-contact tip, 08/10/2020

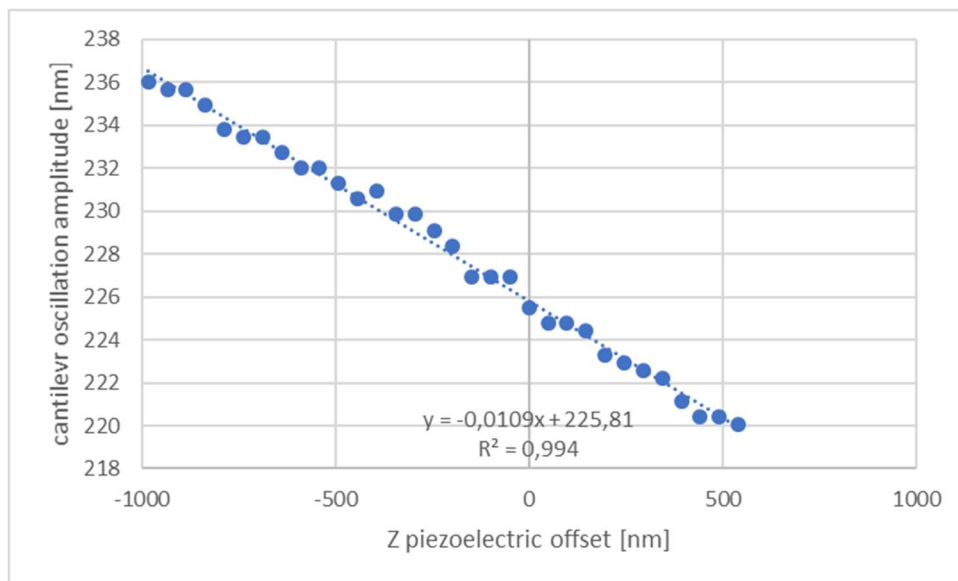


**Figure 28** Variation of the tip amplitude oscillation vs Z-piezoelectric offset for TMV in the retract phase with cantilever stiffness 5 N/m. Non-contact tip, 08/10/2020

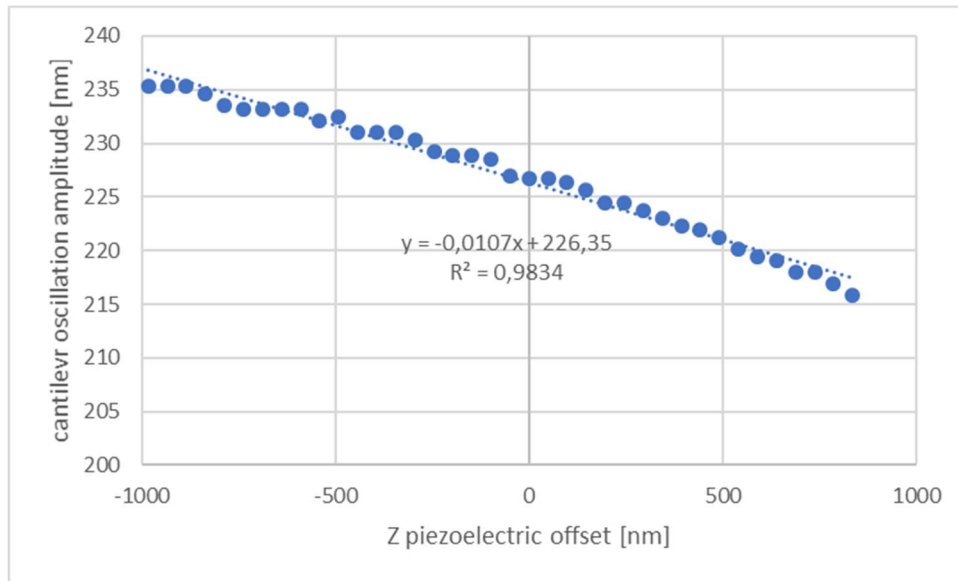


**Figure 29** Variation of the tip amplitude oscillation vs Z-piezoelectric offset for Mica in the approach phase with cantilever stiffness 5 N/m. Non-contact tip, 08/10/2020

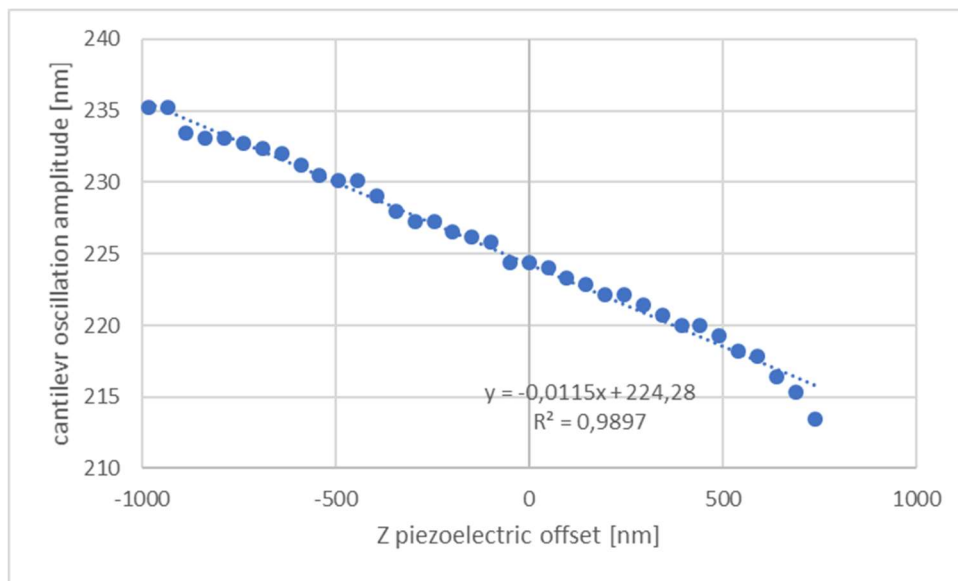


**Figure 30** Variation of the tip amplitude oscillation vs Z-piezoelectric offset for Mica in the retract phase with cantilever stiffness 5 N/m. Non-contact tip, 08/10/2020

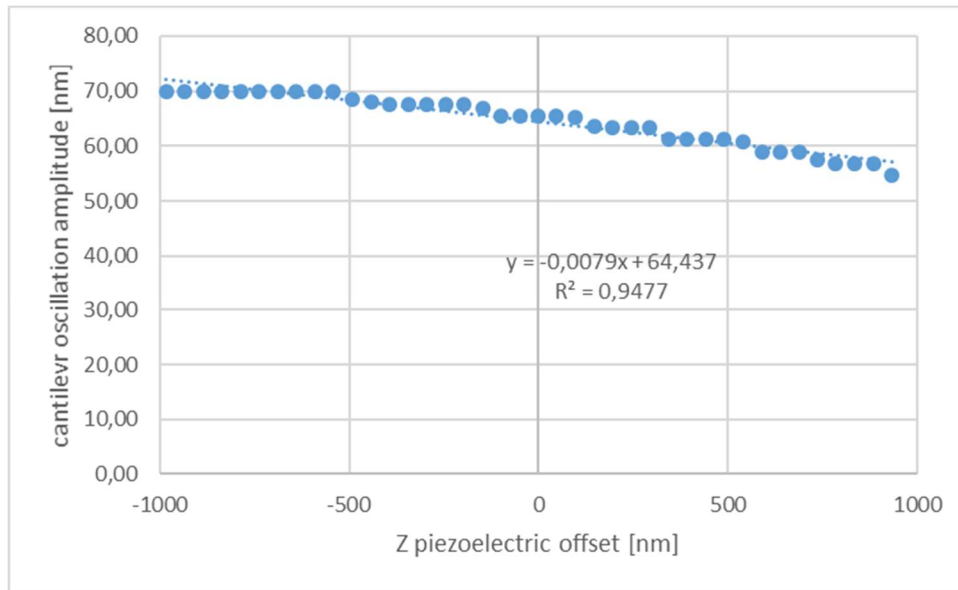


**Figure 31** Variation of the tip amplitude oscillation vs Z-piezoelectric offset for TMV in the approach phase with cantilever stiffness 0.12 N/m. Contact tip, 21/10/2020

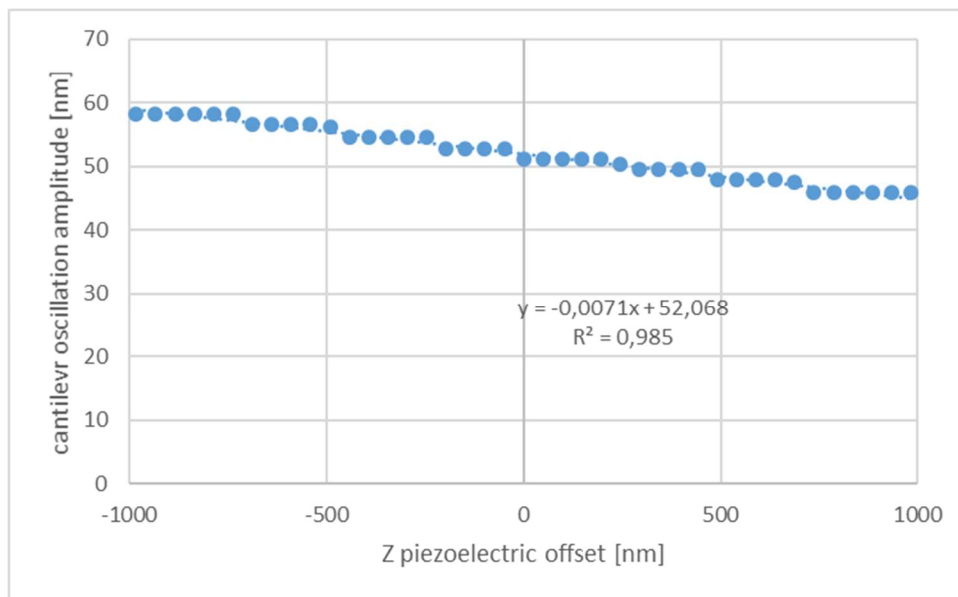


**Figure 32** Variation of the tip amplitude oscillation vs Z-piezoelectric offset for TMV in the retract phase with cantilever stiffness 0.12 N/m. Contact tip, 21/10/2020

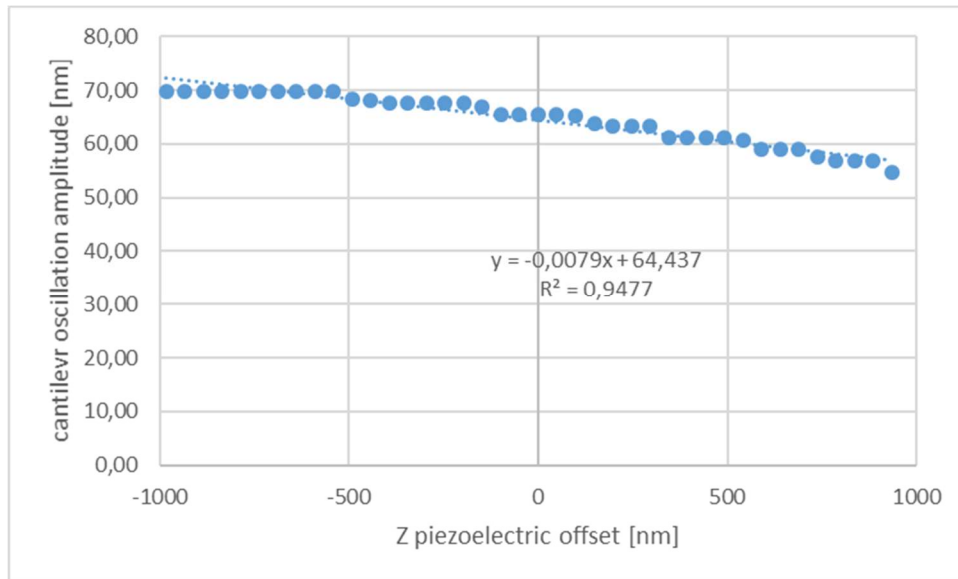


**Figure 33** Variation of the tip amplitude oscillation vs Z-piezoelectric offset for Mica in the approach phase with cantilever stiffness 0.12 N/m. Contact tip, 21/10/2020

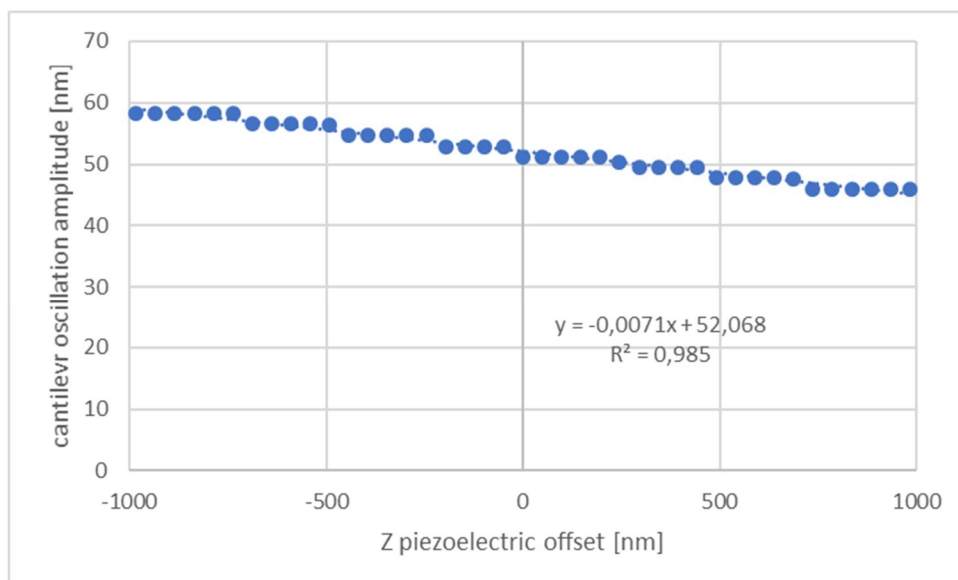


**Figure 34** Variation of the tip amplitude oscillation vs Z-piezoelectric offset for Mica in the retract phase with cantilever stiffness 0.12 N/m. Contact tip, 21/10/2020

Some amplitude oscillating tests failed because of it has not been possible to make topographic measurements with contact cantilever tip with the non-contact AFM.

All the measurements provide the amplitude oscillations expressed in Volt. In order to convert its value in length (nm), the conversion factor has been found as the ratio between the pitch of the screw for the photodiode adjustment (just measured by INRiM in the previous experimental tests and equal to 315  $\mu\text{m}$ ) and the voltage corresponding to a turn of the screw (3.62 V), then corrected for the amplification caused by the optical lever of

the laser beam on the photodiode (about 400). The coefficient obtained, 217.5 nm/V, is used in the Hook's law to determine the stiffness for the calculation of the elastic modulus.

### 3.3 Spectroscopy force tests

Another capability of metrological AFM is to measure how cantilever deflects when the piezoelectric scanner moves perpendicularly to the sample. So, the curve force-distance allows to calculate some properties like adhesion and stiffness. It is the result of the conversion of the curve deflection- tip-sample distance separation by means of the spring constant calibration and deflection sensitivity. The new curve modeled makes possible the analysis of sample properties.

In INRiM all the spectroscopy forces have been developed for contact cantilever tip and non- contact cantilever tip and, according the mode used, the conversion factor is obtained in different way.

For non-contact tips, the conversion factor for photodiode adjustment is corrected for a parameter equal to the slope of amplitude oscillation – piezoelectric Z offset (par. 3.2) for TMV and mica while cantilever is retracting, and then multiplied for the cantilever spring constant, thus applying the Hooke's law.

For contact tips, the “Spectroscopy tool” of metrological AFM sets the force value to about 250 nN as the maximum force for the probing. Therefore, the ratio between this force and the minimum voltage recorded by the tool gives the conversion factor.

The table below summarizes all the calculations done:

#### Non contact tip

Test date	Sample/substrate	Conversion factor photodiode (nm/V)	Amplit. – Z offset slope (R)	k (N/m)	Force-voltage coefficient (nN/V) (G)
08/10/2020	TMV	217.5	0,019	5	11,85
08/10/2020	Mica	217.5	0,0115	5	12,50
20/10/2020	TMV	217.5	0,0147	46	147,07
20/10/2020	Mica	217.5	0,0243	46	243,12

Law used for force-voltage coefficient	$G = 217.5 R k$
--	-----------------

**Table 6 Calculation of force-voltage coefficient for non contact tips**

**Contact tip**

Test date	Spring constant	Sample/substrate	Force-Voltage coefficient (nN/V) (G)
13/10/2020	0.12	Mica	185,69
13/10/2020	0.12	TMV	193,68
21/10/2020	0.12	Mica	194,70
21/10/2020	0.12	TMV	195,12
21/10/2020	0.58	Mica	231,10
21/10/2020	0.58	TVM	223,99
22/10/2020	0.18	Mica	247,37
22/10/2020	0.18	TMV	247,32
Law used for force-voltage coefficient	$G = 250/ Vmin$		

**Table 7 Calculation of force-voltage coefficient for contact tips**

The plots of force spectroscopy curves describe how the interaction force between the tip and the sample varies in the stroke of the piezoelectric scanner.

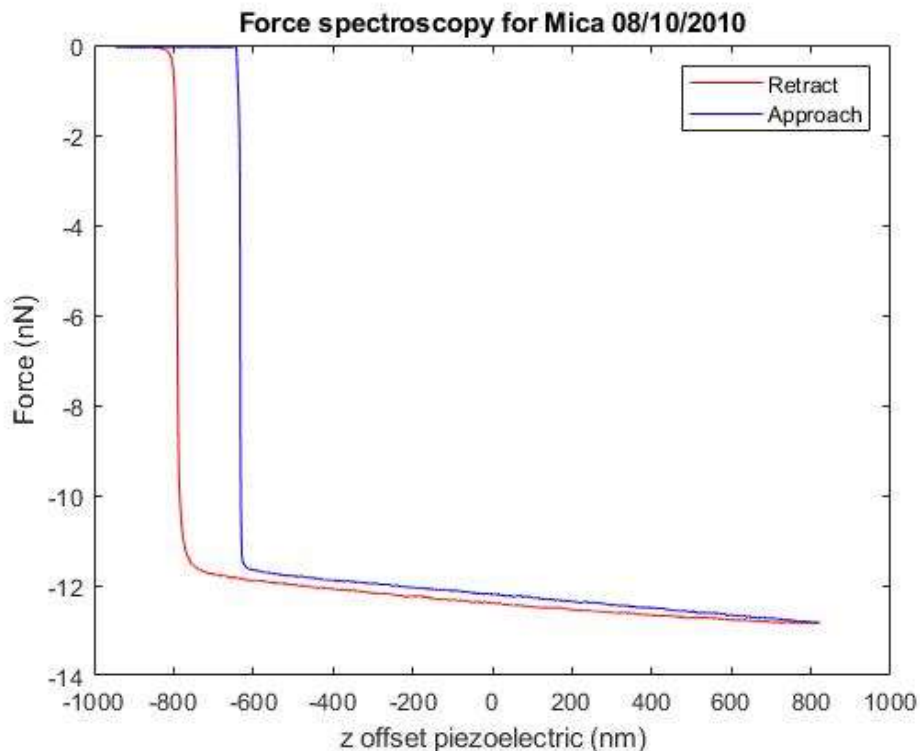


**Figure 35 Force spectroscopy of Mica. Comparison between approach and retract for**

*non-contact tip, 08/10/2020*

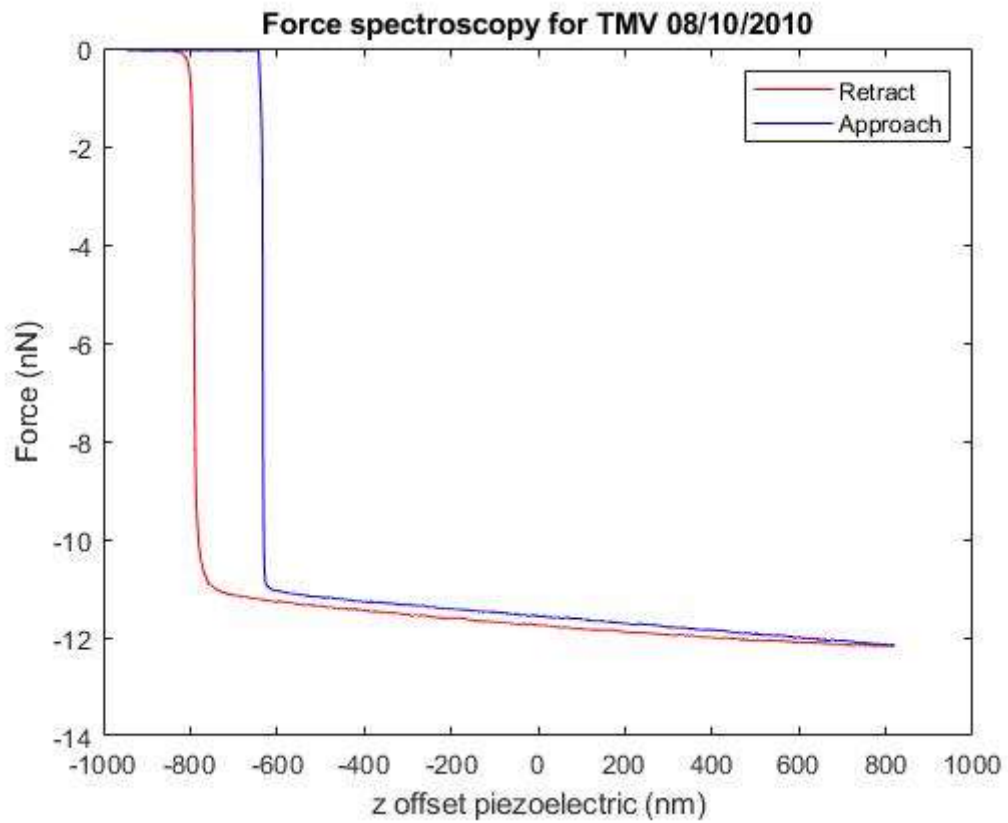


**Figure 36** Force spectroscopy of TMV. Comparison between approach and retract for non-contact tip, 08/10/2020

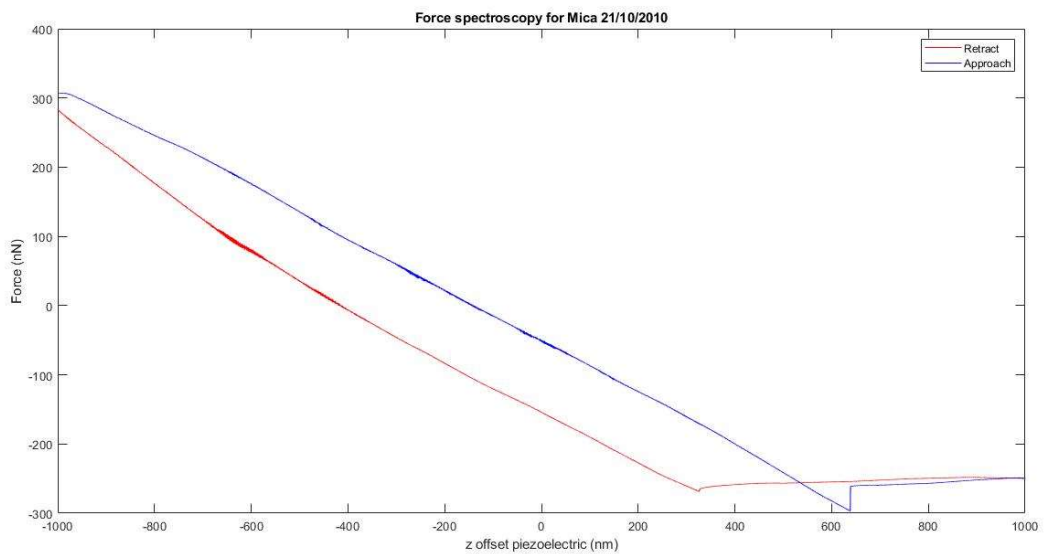


**Figure 37** Force spectroscopy of Mica. Comparison between approach and retract for contact tip, 21/10/2020

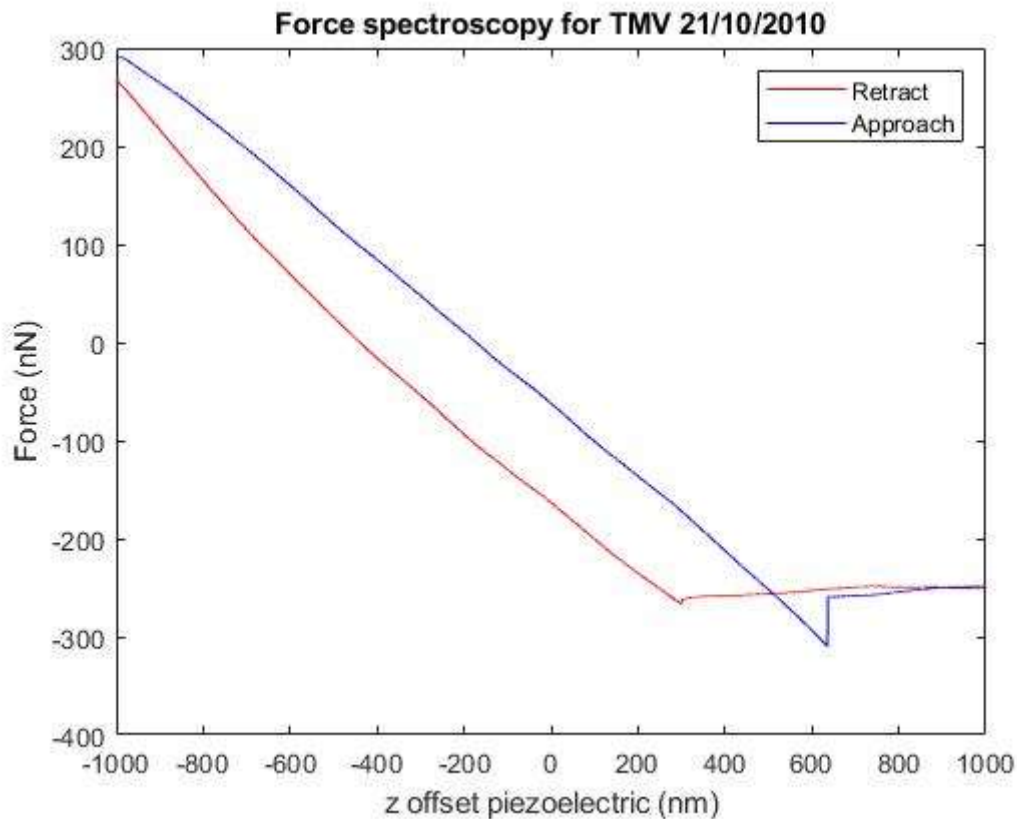


**Figure 38 Force spectroscopy of TMV. Comparison between approach and retract for contact tip, 21/10/2020**

In fig. 38 and 39 we have a plateau: when the cantilever approaches to the sample, the tip-surface interactions make the cantilever snap into contact with the sample, when it retracts, the tip gets stuck in an adhesive dip before emerging from the adhesion at the interface.

The determination of this gain  $G$  (nN/V) leads to the representation of the force-distance curve. In this way it is possible to calculate the stiffness as the slope of the unloading curve section before the spectroscopy force well for mica and TMV. It helps for the calculation of the reduced Young modulus  $E'$  for both the cases considered, according to the Sneddon law<sup>28</sup>:

$$E' = \frac{1}{2} S \sqrt{\frac{\pi}{A_c}} \quad (3.1)$$

Where  $A_c$  is the contact area.

All the stiffness  $S$  are reported in the table as follows:

Tip mode	Test date	k (N/m)	Sample/Substrate	Stiffness (N/m) ( $S$ )
<b>Non-Contact tip</b>	08/10/2020	5	Mica	1,37
	08/10/2020	5	TMV	1,35
	20/10/2020	46	Mica	13,77
	20/10/2020	46	TMV	8,47
<b>Contact tip</b>	13/10/2020	0.12	Mica	17,18
	13/10/2020	0.12	TMV	17,88
	21/10/2020	0.12	Mica	8,30
	21/10/2020	0.12	TMV	8,08
	21/10/2020	0.58	Mica	16,4
	21/10/2020	0.58	TMV	15,07
	22/10/2020	0.18	Mica	11,90
	22/10/2020	0.18	TMV	11,72

*Table 8 Stiffness for all the force-distance curves*

### 3.4 Calculation of the Young Modulus for TMV and Mica

All these experimental tests are needed for the calculation of the Young Modulus for Mica and TMV, in order to study nanostructure's behavior. For this purpose, a new model is

formulated.

As noted above, the force spectroscopy has been studied both for mica and TMV through a non-contact cantilever tip and a contact cantilever tip. The first step of this model consists of the approximation of tip-mica contact to the Hertzian model with sphere – half elastic space and the approximation of tip-TMV contact to the Hertzian model with sphere-cylinder.

The real cantilever tip used for the experiments has a four-sided pyramid shape and it can be compared with a Vickers indenter. Therefore, all the mechanical properties can be related to the area of contact between the bodies taken in consideration and it depends on the penetration depth  $h^{29}$ .

$$A_c = \pi (h * \tan\vartheta)^2 \quad (3.2)$$

Where  $\vartheta$  is the equivalent half-angle for Vickers indenter (about 68°).

The reduced Young Modulus and mica/TMV Young modulus are estimated through an iteration (of maximum 100 steps), in which the penetration depth varies until an effective value of this elastic modulus can be found (eq. 2.27, 3.1 and 3.2).

For cantilever tip – mica contact, the Hertzian model for sphere-half elastic space contact is used to find all the properties related to the Hertz model, comparing it with JKR and DMT models for the elastic modulus estimation.

The Hertzian model for sphere-cylinder, modeled to study cantilever tip – TMV contact, determines a contact area with elliptical shape and depending on the depth indentation. Because of the comparable values of its semi-axis, the ellipse is approximated to a circle in order to simplify all the next steps for mechanical properties calculation.

DMT and JKR models includes the work of adhesion. Its value is estimated by another iteration, until its value is within a range taken from sources in literature, where the work of adhesion is estimated in a range from 0 to 2,4 mJ/m<sup>2</sup> for Mica<sup>30</sup> and from 0 to 70 mJ/m<sup>2</sup> for TMV<sup>31</sup>.

Parameters		08/10/2020	20/10/2020
Tip Poisson ratio	$\nu_{\text{tip}}$	0,27	0,27
TMV Poisson ratio	$\nu_{\text{TMV}}$	0,48	0,48

<b>Tip Young Modulus</b>	$E_{tip}$	GPa	149	149
<b>Penetration depth</b>	$h$	nm	0,166	1,02
<b>Contact Area</b>	$A$	$m^2$	5,31E-19	2,02E-17
<b>Stiffness</b>	$S$	N/m	1,354	8,475
<b>Reduced Young Modulus</b>	$E'$	GPa	1,65	1,67
<b>TMV Young Modulus</b>	$E_{TMV}$	GPa	1,28	1,30
<b>Curvature radius</b>	$R_{tip}$	nm	8,00	8,00
<b>TMV radius</b>	$R_{TMV}$	nm	9,00	9,00
<b>Radius</b>	$R$	nm	4,24	4,24
<b>tan (35°)</b>	$\tan$		0,70	0,70
	$\pi$		3,14	3,14
<b>work of adhesion</b>	$\gamma$	J/m <sup>2</sup>	0,02	0,02
<b>General contact radius</b>	$a$	nm	0,839	2,08
<b>Approx. Contact radius</b>	$q$	nm	0,837	2,08
<b>Hertzian Force</b>	$F_{Hertz}$	nN	0,304	4,73
<b>JKR force</b>	$F_{JKR}$	nN	2,16	24,5
<b>JKR contact radius</b>	$a_{JKR}$	nm	1,77	3,96
<b>JKR penetration depth</b>	$h_{JKR}$	nm	0,317	1,71
<b>JKR Contact Area</b>	$A_{JKR}$	$m^2$	1,93E-18	5,63E-17
<b>JKR Reduced Young Modulus</b>	$E'_{JKR}$	GPa	0,864	1,00
<b>JKR TMV Young Modulus</b>	$E_{TMV_{JKR}}$	GPa	0,668	0,775
<b>DMT Force</b>	$F_{DMT}$	nN	0,836	10
<b>DMT Contact radius</b>	$a_{DMT}$	nm	1,17	2,67
<b>DMT Penetration depth</b>	$h_{DMT}$	nm	0,325	1,69
<b>DMT Contact Area</b>	$A_{DMT}$	$m^2$	2,03E-18	5,48E-17
<b>DMT Reduced Young Modulus</b>	$E'_{DMT}$	GPa	0,842	1,01
<b>DMT TMV Young Modulus</b>	$E_{TMV_{DMT}}$	GPa	0,651	0,786

*Table 9 Calculation of mechanical properties for TMV with non-contact tip*

Parameters			08/10/2020	20/10/2020
<b>Tip Poisson ratio</b>	$\nu_{tip}$		0,27	0,27
<b>TMV Poisson ratio</b>	$\nu_{MICA}$		0,25	0,25
<b>Tio Young Modulus</b>	$E_{tip}$	GPa	149	149
<b>Penetration depth</b>	$h$	nm	3,10E-3	0,0310
<b>Contact Area</b>	$A$	$m^2$	1,85E-22	1,85E-20
<b>Stiffness</b>	$S$	N/m	1,375	13,77
<b>Reduced Young Modulus</b>	$E'$	GPa	89,6	89,6
<b>TMV Young Modulus</b>	$E_{MICA}$	GPa	190	190
<b>Curvature radius</b>	$R_{tip}$	nm	8,00	8,00
<b>TMV radius</b>	$R_{MICA}$	nm	inf	inf

<b>Radius</b>	R	nm	8,00	8,00
<b>tan (35°)</b>	tan		0,70	0,70
	$\pi$		3,14	3,14
<b>work of adhesion</b>	$\gamma$	J/m <sup>2</sup>	3,00E-05	1,00E-04
<b>Contact radius</b>	a	nm	0,157	0,498
<b>Hertzian Force</b>	F <sub>Hertz</sub>	nN	0,0583	1,85
<b>JKR force</b>	F <sub>JKR</sub>	nN	0,0863	2,10
<b>JKR contact radius</b>	a <sub>JKR</sub>	nm	0,179	0,520
<b>JKR penetration depth</b>	h <sub>JKR</sub>	nm	3,41E-3	0,0319
<b>JKR Contact Area</b>	A <sub>JKR</sub>	m <sup>2</sup>	2,24E-22	1,96E-20
<b>JKR Reduced Young Modulus</b>	E' <sub>JKR</sub>	GPa	81,5	87,3
<b>JKR TMV Young Modulus</b>	E <sub>MICA JKR</sub>	GPa	155	179
<b>DMT Force</b>	F <sub>DMT</sub>	nN	0,0598	1,85
<b>DMT Contact radius</b>	a <sub>DMT</sub>	nm	0,159	0,499
<b>DMT Penetration depth</b>	h <sub>DMT</sub>	nm	3,15E-3	0,0311
<b>DMT Contact Area</b>	A <sub>DMT</sub>	m <sup>2</sup>	1,91E-22	1,86E-20
<b>DMT Reduced Young Modulus</b>	E' <sub>DMT</sub>	GPa	88,1	89,5
<b>DMT TMV Young Modulus</b>	E <sub>MICA DMT</sub>	GPa	183	189

*Table 10 Calculation of mechanical properties for Mica with non-contact tip*

Parameters	13/10/2020		
<b>Tip Poisson ratio</b>	$\nu_{tip}$		0,27
<b>TMV Poisson ratio</b>	$\nu_{TMV}$		0,48
<b>Tio Young Modulus</b>	E <sub>tip</sub>	GPa	149
<b>Penetration depth</b>	h	nm	1,00
<b>Contact Area</b>	A	m <sup>2</sup>	1,93E-17
<b>Stiffness</b>	S	N/m	8.29
<b>Reduced Young Modulus</b>	E'	GPa	1,67
<b>TMV Young Modulus</b>	E <sub>TMV</sub>	GPa	1,30
<b>Curvature radius</b>	R <sub>tip</sub>	nm	8,00
<b>TMV radius</b>	R <sub>TMV</sub>	nm	9,00
<b>Radius</b>	R	nm	4,24
<b>tan (35°)</b>	tan		0,70
	$\pi$		3,14
<b>work of adhesion</b>	$\gamma$	J/m <sup>2</sup>	0,07
<b>Hertzian Force</b>	F <sub>Hertz</sub>	nN	4,58
<b>General contact radius</b>	q	nm	2,06
<b>Approx. Contact radius</b>	a	nm	2,06
<b>JKR force</b>	F <sub>JKR</sub>	nN	13,1
<b>JKR contact radius</b>	a <sub>JKR</sub>	nm	3,22

<b>JKR penetration depth</b>	$h_{JKR}$	nm	1,38
<b>JKR Contact Area</b>	$A_{JKR}$	$m^2$	3,68E-17
<b>JKR Reduced Young Modulus</b>	$E'_{JKR}$	GPa	1,21
<b>JKR TMV Young Modulus</b>	$E_{TMV JKR}$	GPa	0,94
<b>DMT Force</b>	$F_{DMT}$	nN	6,44
<b>DMT Contact radius</b>	$a_{DMT}$	nm	2,30
<b>DMT Penetration depth</b>	$h_{DMT}$	nm	1,25
<b>DMT Contact Area</b>	$A_{DMT}$	$m^2$	3,02E-17
<b>DMT Reduced Young Modulus</b>	$E'_{DMT}$	GPa	1,34
<b>DMT TMV Young Modulus</b>	$E_{TMV DMT}$	GPa	1,04

*Table 11 Calculation of mechanical properties for TMV with contact tip, 13/10/2020*

Parameters	21/10/2020 k 0.12		
<b>Tip Poisson ratio</b>	$\nu_{tip}$		0,27
<b>TMV Poisson ratio</b>	$\nu_{TMV}$		0,48
<b>Tio Young Modulus</b>	$E_{tip}$	GPa	149
<b>Penetration depth</b>	$h$	nm	1,02
<b>Contact Area</b>	$A$	$m^2$	1,92E-17
<b>Stiffness</b>	$S$	N/m	8,08
<b>Reduced Young Modulus</b>	$E'$	GPa	1,61
<b>TMV Young Modulus</b>	$E_{TMV}$	GPa	1,25
<b>Curvature radius</b>	$R_{tip}$	nm	8,00
<b>TMV radius</b>	$R_{TMV}$	nm	9,00
<b>Radius</b>	$R$	nm	4,24
<b>tan (35°)</b>	tan		0,70
	$\pi$		3,14
<b>work of adhesion</b>	$\gamma$	J/m <sup>2</sup>	0,07
<b>Hertzian Force</b>	$F_{Hertz}$	nN	4,49
<b>General contact radius</b>	$q$	nm	2,07
<b>Approx. Contact radius</b>	$a$	nm	2,07
<b>JKR force</b>	$F_{JKR}$	nN	13,0
<b>JKR contact radius</b>	$a_{JKR}$	nm	3,25
<b>JKR penetration depth</b>	$h_{JKR}$	nm	1,41
<b>JKR Contact Area</b>	$A_{JKR}$	$m^2$	3,17E-17
<b>JKR Reduced Young Modulus</b>	$E'_{JKR}$	GPa	1,16
<b>JKR TMV Young Modulus</b>	$E_{TMV JKR}$	GPa	0,902
<b>DMT Force</b>	$F_{DMT}$	nN	6,35
<b>DMT Contact radius</b>	$a_{DMT}$	nm	2,32
<b>DMT Penetration depth</b>	$h_{DMT}$	nm	1,27

<b>DMT Contact Area</b>	$A_{DMT}$	$m^2$	3,17E-17
<b>DMT Reduced Young Modulus</b>	$E'_{DMT}$	GPa	1,28
<b>DMT TMV Young Modulus</b>	$E_{TMV DMT}$	GPa	0,994

*Table 12 Calculation of mechanical properties for TMV with contact tip, 21/10/2020*

Parameters			21/10/2020 k 0.58
<b>Tip Poisson ratio</b>	$\nu_{tip}$		0,27
<b>TMV Poisson ratio</b>	$\nu_{TMV}$		0,48
<b>Tio Young Modulus</b>	$E_{tip}$	GPa	149
<b>Penetration depth</b>	$h$	nm	0,868
<b>Contact Area</b>	$A$	$m^2$	1,45E-17
<b>Stiffness</b>	$S$	N/m	8,08
<b>Reduced Young Modulus</b>	$E'$	GPa	1,63
<b>TMV Young Modulus</b>	$E_{TMV}$	GPa	1,27
<b>Curvature radius</b>	$R_{tip}$	nm	8,00
<b>TMV radius</b>	$R_{TMV}$	nm	9,00
<b>Radius</b>	$R$	nm	4,24
<b>tan (35°)</b>	$\tan$		0,70
	$\pi$		3,14
<b>work of adhesion</b>	$\gamma$	J/m <sup>2</sup>	0,07
<b>Hertzian Force</b>	$F_{Hertz}$	nN	3,60
<b>General contact radius</b>	$q$	nm	1,92
<b>Approx. Contact radius</b>	$a$	nm	1,91
<b>JKR force</b>	$F_{JKR}$	nN	11,7
<b>JKR contact radius</b>	$a_{JKR}$	nm	3,12
<b>JKR penetration depth</b>	$h_{JKR}$	nm	1,24
<b>JKR Contact Area</b>	$A_{JKR}$	$m^2$	2,94E-17
<b>JKR Reduced Young Modulus</b>	$E'_{JKR}$	GPa	1,15
<b>JKR TMV Young Modulus</b>	$E_{TMV JKR}$	GPa	0,889
<b>DMT Force</b>	$F_{DMT}$	nN	5,47
<b>DMT Contact radius</b>	$a_{DMT}$	nm	2,20
<b>DMT Penetration depth</b>	$h_{DMT}$	nm	1,13
<b>DMT Contact Area</b>	$A_{DMT}$	$m^2$	2,51E-17
<b>DMT Reduced Young Modulus</b>	$E'_{DMT}$	GPa	1,24
<b>DMT TMV Young Modulus</b>	$E_{TMV DMT}$	GPa	0,963

*Table 13 Calculation of mechanical properties for TMV with contact tip, 21/10/2020*

Parameters			22/10/2020 k 0.18
<b>Tip Poisson ratio</b>	$\nu_{tip}$		0,27

<b>TMV Poisson ratio</b>	$\nu_{TMV}$		0,48
<b>Tio Young Modulus</b>	$E_{tip}$	GPa	149
<b>Penetration depth</b>	$h$	nm	1,46
<b>Contact Area</b>	$A$	$m^2$	4,11E-17
<b>Stiffness</b>	$S$	N/m	11,72
<b>Reduced Young Modulus</b>	$E'$	GPa	1,62
<b>TMV Young Modulus</b>	$E_{TMV}$	GPa	1,26
<b>Curvature radius</b>	$R_{tip}$	nm	8,00
<b>TMV radius</b>	$R_{TMV}$	nm	9,00
<b>Radius</b>	$R$	nm	4,24
<b>tan (35°)</b>	tan		0,70
	$\pi$		3,14
<b>work of adhesion</b>	$\gamma$	J/m <sup>2</sup>	7,00E-02
<b>Hertzian Force</b>	$F_{Hertz}$	nN	7,81
<b>General contact radius</b>	$q$	nm	2,49
<b>Approx. Contact radius</b>	$a$	nm	2,48
<b>JKR force</b>	$F_{JKR}$	nN	17,8
<b>JKR contact radius</b>	$a_{JKR}$	nm	3,59
<b>JKR penetration depth</b>	$h_{JKR}$	nm	1,91
<b>JKR Contact Area</b>	$A_{JKR}$	$m^2$	7,02E-17
<b>JKR Reduced Young Modulus</b>	$E'_{JKR}$	GPa	1,24
<b>JKR TMV Young Modulus</b>	$E_{TMVJKR}$	GPa	0,961
<b>DMT Force</b>	$F_{DMT}$	nN	9,67
<b>DMT Contact radius</b>	$a_{DMT}$	nm	2,67
<b>DMT Penetration depth</b>	$h_{DMT}$	nm	1,68
<b>DMT Contact Area</b>	$A_{DMT}$	$m^2$	5,42E-17
<b>DMT Reduced Young Modulus</b>	$E'_{DMT}$	GPa	1,41
<b>DMT TMV Young Modulus</b>	$E_{TMVDMT}$	GPa	1,10

*Table 14 Calculation of mechanical properties for TMV with contact tip, 22/10/2020*

Parameters	13/10/2020		
<b>Tip Poisson ratio</b>	$\nu_{tip}$		0,27
<b>TMV Poisson ratio</b>	$\nu_{MICA}$		0,25
<b>Tio Young Modulus</b>	$E_{tip}$	GPa	1,49
<b>Penetration depth</b>	$H$	nm	0,0193
<b>Contact Area</b>	$A$	$m^2$	7,18E-21
<b>Stiffness</b>	$S$	N/m	8,56
<b>Reduced Young Modulus</b>	$E'$	GPa	89,5
<b>TMV Young Modulus</b>	$E_{MICA}$	GPa	190
<b>Curvature radius</b>	$R_{tip}$	nm	8,00

<b>TMV radius</b>	$R_{MICA}$	nm	inf
<b>Radius</b>	R	nm	8,00
<b>tan (35°)</b>	Tan		0,70
	$\Pi$		3,14
<b>Contact radius</b>	A	nm	0,393
<b>work of adhesion</b>	$\Gamma$	J/m <sup>2</sup>	1,00E-04
<b>Hertzian Force</b>	$F_{Hertz}$	nN	0,906
<b>JKR force</b>	$F_{JKR}$	nN	1,09
<b>JKR contact radius</b>	$a_{JKR}$	nm	0,418
<b>JKR penetration depth</b>	$h_{JKR}$	nm	0,0201
<b>JKR Contact Area</b>	$A_{JKR}$	m <sup>2</sup>	7,78E-21
<b>JKR Reduced Young Modulus</b>	$E'_{JKR}$	GPa	86,0
<b>JKR TMV Young Modulus</b>	$E_{MICA\ JKR}$	GPa	174
<b>DMT Force</b>	$F_{DMT}$	nN	0,911
<b>DMT Contact radius</b>	$a_{DMT}$	nm	0,394
<b>DMT Penetration depth</b>	$h_{DMT}$	nm	0,0194
<b>DMT Contact Area</b>	$A_{DMT}$	m <sup>2</sup>	7,24E-21
<b>DMT Reduced Young Modulus</b>	$E'_{DMT}$	GPa	89,2
<b>DMT TMV Young Modulus</b>	$E_{MICA\ DMT}$	GPa	188

*Table 15 Calculation of mechanical properties for MICA with contact tip, 13/10/2020*

Parameters	21/10/2020 k 0.12		
<b>Tip Poisson ratio</b>	$\nu_{tip}$		0,27
<b>TMV Poisson ratio</b>	$\nu_{MICA}$		0,25
<b>Tio Young Modulus</b>	$E_{tip}$	GPa	149
<b>Penetration depth</b>	H	nm	0,0187
<b>Contact Area</b>	A	m <sup>2</sup>	6,75E-21
<b>Stiffness</b>	S	N/m	8,3
<b>Reduced Young Modulus</b>	$E'$	GPa	89,5
<b>TMV Young Modulus</b>	$E_{MICA}$	GPa	190
<b>Curvature radius</b>	$R_{tip}$	nm	8,00
<b>TMV radius</b>	$R_{MICA}$	nm	inf
<b>Radius</b>	R	nm	8,00
<b>tan (35°)</b>	Tan		0,70
	$\Pi$		3,14
<b>Contact radius</b>	A	nm	0,387
<b>work of adhesion</b>	$\Gamma$	J/m <sup>2</sup>	1,00E-04

<b>Hertzian Force</b>	$F_{\text{Hertz}}$	nN	0,865
<b>JKR force</b>	$F_{\text{JKR}}$	nN	1,04
<b>JKR contact radius</b>	$a_{\text{JKR}}$	nm	0,412
<b>JKR penetration depth</b>	$h_{\text{JKR}}$	nm	0,0195
<b>JKR Contact Area</b>	$A_{\text{JKR}}$	$\text{m}^2$	7,33E-21
<b>JKR Reduced Young Modulus</b>	$E'_{\text{JKR}}$	GPa	85,9
<b>JKR TMV Young Modulus</b>	$E_{\text{MICA JKR}}$	GPa	173
<b>DMT Force</b>	$F_{\text{DMT}}$	nN	0,870
<b>DMT Contact radius</b>	$a_{\text{DMT}}$	nm	0,388
<b>DMT Penetration depth</b>	$h_{\text{DMT}}$	nm	0,0188
<b>DMT Contact Area</b>	$A_{\text{DMT}}$	$\text{m}^2$	6,80E-21
<b>DMT Reduced Young Modulus</b>	$E'_{\text{DMT}}$	GPa	89,2
<b>DMT TMV Young Modulus</b>	$E_{\text{MICA DMT}}$	GPa	188

*Table 16 Calculation of mechanical properties for MICA with contact tip, 21/10/2020*

Parameters		21/10/2020 k 0.58	
<b>Tip Poisson ratio</b>	$\nu_{\text{tip}}$		0,27
<b>TMV Poisson ratio</b>	$\nu_{\text{MICA}}$		0,25
<b>Tip Young Modulus</b>	$E_{\text{tip}}$	GPa	149
<b>Penetration depth</b>	H	nm	0,0177
<b>Contact Area</b>	A	$\text{m}^2$	6,01E-21
<b>Stiffness</b>	S	N/m	7,83
<b>Reduced Young Modulus</b>	$E'$	GPa	89,5
<b>TMV Young Modulus</b>	$E_{\text{MICA}}$	GPa	190
<b>Curvature radius</b>	$R_{\text{tip}}$	nm	8,00
<b>TMV radius</b>	$R_{\text{MICA}}$	nm	Inf
<b>Radius</b>	R	nm	8,00
<b>tan (35°)</b>	Tan		0,70
	$\Pi$		3,14
<b>Contact radius</b>	A	nm	0,376
<b>work of adhesion</b>	$\Gamma$	$\text{J}/\text{m}^2$	1,00E-04
<b>Hertzian Force</b>	$F_{\text{Hertz}}$	nN	0,793
<b>JKR force</b>	$F_{\text{JKR}}$	nN	0,963
<b>JKR contact radius</b>	$a_{\text{JKR}}$	nm	0,401
<b>JKR penetration depth</b>	$h_{\text{JKR}}$	nm	0,0184
<b>JKR Contact Area</b>	$A_{\text{JKR}}$	$\text{m}^2$	6,55E-21
<b>JKR Reduced Young Modulus</b>	$E'_{\text{JKR}}$	GPa	85,8
<b>JKR TMV Young Modulus</b>	$E_{\text{MICA JKR}}$	GPa	172
<b>DMT Force</b>	$F_{\text{DMT}}$	nN	0,798

<b>DMT Contact radius</b>	$a_{DMT}$	nm	0,377
<b>DMT Penetration depth</b>	$h_{DMT}$	nm	0,0177
<b>DMT Contact Area</b>	$A_{DMT}$	m <sup>2</sup>	6,06E-21
<b>DMT Reduced Young Modulus</b>	$E'_{DMT}$	GPa	89,1
<b>DMT TMV Young Modulus</b>	$E_{MICA DMT}$	GPa	188

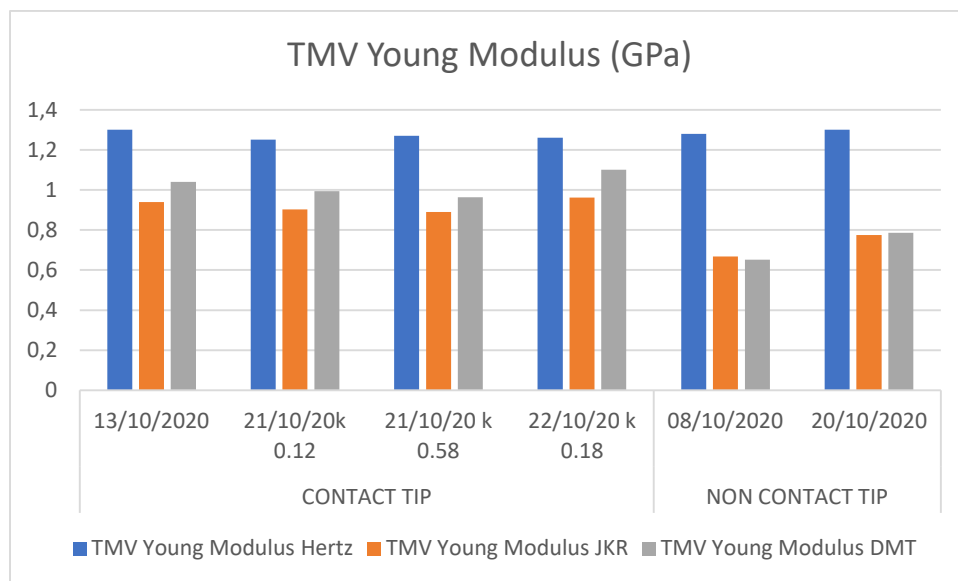
*Table 17 Calculation of mechanical properties for MICA with contact tip, 21/10/2020*

Parameters		22/10/2020 k 0.18	
<b>Tip Poisson ratio</b>	$\nu_{tip}$		0,27
<b>TMV Poisson ratio</b>	$\nu_{MICA}$		0,25
<b>Tip Young Modulus</b>	$E_{tip}$	GPa	149
<b>Penetration depth</b>	H	nm	0,0269
<b>Contact Area</b>	A	m <sup>2</sup>	1,39E-20
<b>Stiffness</b>	S	N/m	11,9
<b>Reduced Young Modulus</b>	$E'$	GPa	89,5
<b>TMV Young Modulus</b>	$E_{MICA}$	GPa	190
<b>Curvature radius</b>	$R_{tip}$	nm	8,00
<b>TMV radius</b>	$R_{MICA}$	nm	inf
<b>Radius</b>	R	nm	8,00
<b>tan (35°)</b>	Tan		0,70
	$\Pi$		3,14
<b>Contact radius</b>	A	nm	0,0464
<b>work of adhesion</b>	$\Gamma$	J/m <sup>2</sup>	1,00E-04
<b>Hertzian Force</b>	$F_{Hertz}$	nN	1,49
<b>JKR force</b>	$F_{JKR}$	nN	1,71
<b>JKR contact radius</b>	$a_{JKR}$	nm	0,486
<b>JKR penetration depth</b>	$h_{JKR}$	nm	0,0277
<b>JKR Contact Area</b>	$A_{JKR}$	m <sup>2</sup>	1,47E-20
<b>JKR Reduced Young Modulus</b>	$E'_{JKR}$	GPa	86,8
<b>JKR TMV Young Modulus</b>	$E_{MICA JKR}$	GPa	177
<b>DMT Force</b>	$F_{DMT}$	nN	1,49
<b>DMT Contact radius</b>	$a_{DMT}$	nm	0,0464
<b>DMT Penetration depth</b>	$h_{DMT}$	nm	0,0269
<b>DMT Contact Area</b>	$A_{DMT}$	m <sup>2</sup>	1,39E-20
<b>DMT Reduced Young Modulus</b>	$E'_{DMT}$	GPa	89,3
<b>DMT TMV Young Modulus</b>	$E_{MICA DMT}$	GPa	188

*Table 18 Calculation of mechanical properties for MICA with contact tip, 22/10/2020*

In these tables, we can see that, after calculating the reduced Young Modulus of TMV and mica following the steps of the experimental measurements, all the mechanical properties are calculated using the Hertzian, JKR and DMT equations. In this way, it is possible to compare all the results obtained for each method, showing all the differences.

YOUNG MODULUS (GPa)		CONTACT TIP			NON CONTACT TIP		
		13/10/20	21/10/20 k 0.12	21/10/20 k 0.58	22/10/20 k 0.18	08/10/20	20/10/20
<b>TMV</b>	Young Modulus Hertz	1,30	1,25	1,27	1,26	1,28	1,3
	Young Modulus JKR	0,94	0,902	0,889	0,961	0,668	0,775
	Young Modulus DMT	1,04	0,994	0,963	1,10	0,651	0,786
<b>MICA</b>	Young Modulus Hertz	190	190	190	190	190	190
	Young Modulus JKR	174	173	172	177	155	179
	Young Modulus DMT	188	188	188	188	183	189



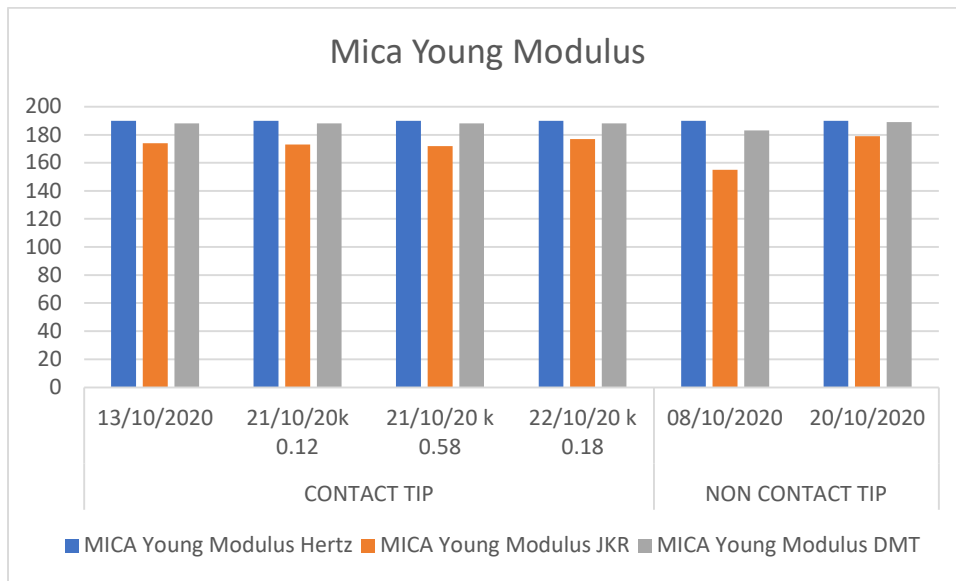


**Table 19 Young Modulus for Mica and TMV according to the models used. All the data are reported in the form of tables and histograms.**

## 4 FEM Analysis

Atomic Force Microscope made it possible to investigate the mechanical properties of the sample analyzed in INRiM. All the tests described in the previous chapter provided the necessary elements to develop a method based on Hertz, JKR and DMT theory for the calculation of Young modulus and depth indentation. The prediction of deformation and stiffness for TMV case determined by AFM measurements are compared with FEM simulation. In this way it is possible to guarantee the reliability of the measurements carried out in the laboratory and to obtain the results of our interest minimizing costs and time. For this purpose, an educational version of Abaqus 6.13-1 is used to evaluate the dynamic response of the cantilever and the force-indentation curve between cantilever-TMV and cantilever-Mica.

### 4.1 Frequency Response function for cantilever model

The first part of FEM simulation consists in calculating the frequency response function for the cantilever used during the AFM tests.

The frequency response function (FRF) is an experimental modal analysis used to plot the amplitude oscillation-frequency curve, providing information on the resonant frequency, the damping and the mode shapes of the structure, defined by the eigenvalues of Newton's laws.

The cantilever is made of silicon nitride, whose density is approximately  $2338,3 \text{ kg/m}^3$  and Young modulus equal to 149 GPa. The Poisson ratio is about 0.27 and the shape cantilever is rectangular. The dimensions used for the model are shown in Tab. 3. The cantilever is assumed to be a 3D solid, given by the extrusion of a rectangular shape. During the swing of the cantilever, the left end of the structure is fixed and the right one can move along the direction perpendicular to the beam surface. The excitation of the cantilever is measured by applying a harmonic force and its magnitude is about 1-10 nN. The cantilever is meshed with tetrahedron elements and the total number is around 700. Submitting the simulation, the results are plotted as follows:

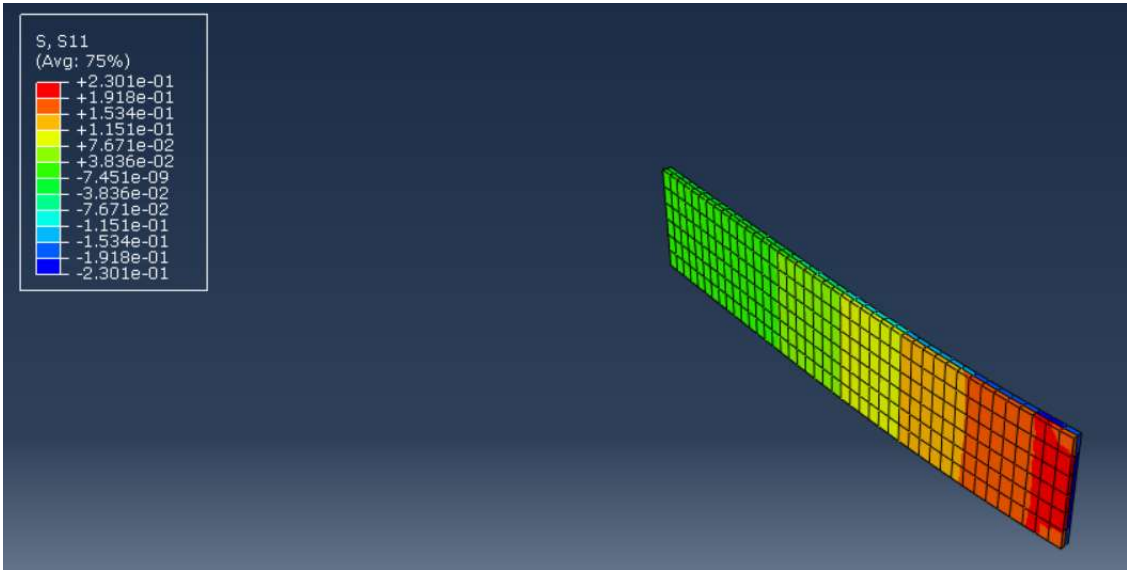


**Figure 39 Postprocessing of FEM simulation of rectangular cantilever**

The picture in Fig. 39 shows the first eigenmode of the cantilever free vibration. The legend describes how Von Mises stress changes along its length, peaking closer to the fixed end.

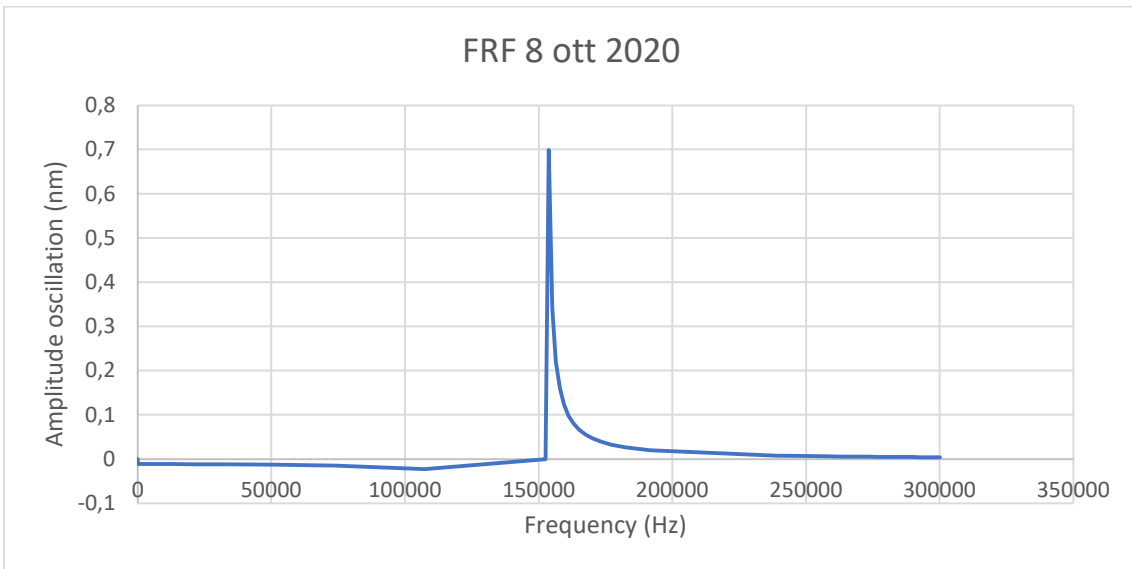


**Figure 40 FRF for 08/10/2020 test**

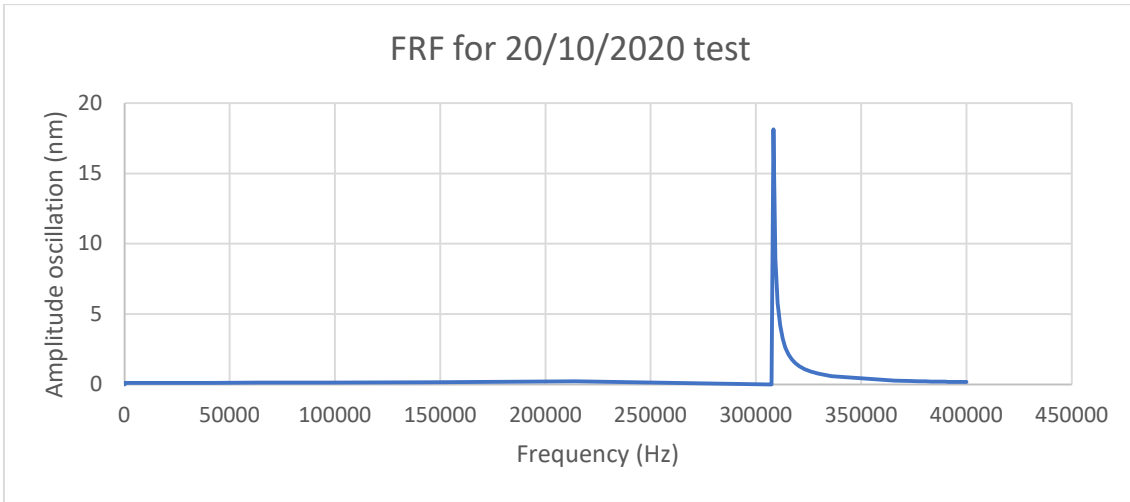


**Figure 41 FRF for 20/10/2020 test**

Figure 40 and 41 shows the amplitude oscillation-frequency curve for the cantilever tested with AFM in non-contact mode. In this way it is easier to determine the resonant frequency and the maximum amplitude oscillation reached. Furthermore, applying the eq. 2.12, the quality factor can be calculated.

In the following table results from FEM Simulation are reported.

Date	Resonant frequency (kHz)	Quality factor
08/10/2020	153	265
20/10/2020	308	771

**Table 20 Resonant frequency and quality factor given by FEM Simulation**

## 4.2 Force-indentation curves

The second part of this simulation consists in performing the structural analysis of the nanostructures as the cantilever approaches the sample. This simulation can only be compared with the tests performed with AFM in contact mode because this software determines these properties only when the bodies are in contact.

In order to simplify the problem and to have a good qualitative comparison with the

Hertzian model, the indenter is approximated to a sphere, TMV is modeled as a cylinder, mica as a cylinder with low curvature, so that it can be quite similar to a plane.

The 2D-axisymmetric model is used to represent the bodies, whose cantilever radius is about 8 nm and TMV radius is estimated equal to 9 nm. The numerical values calculated in the previous chapter are used to define materials' properties:

<b>Body</b>	<b>Young Modulus</b>	<b>Poisson ratio</b>
<b>Cantilever</b>	149 GPa	0.27
<b>TMV</b>	1 GPa	0.48
<b>Mica</b>	190 GPa	0.25

*Table 21 Elastic properties used for FEM Simulation*

In this simulation, the sphere is constrained to be a rigid body and the sample is split in the contact region so that the mesh is finer in that area than the entire body. It means that in the contact region, the number of elements is greater, and it decreases moving away from the contact region. Lower number of elements implies a large element size. Their shape is quadrilateral, and the total number of the elements is up to 1000 (this is the limit of the Abaqus student edition).

The sample is fixed to its base and the indenter can move along vertical direction, and the displacement applied on the simulated tip is equal to the deformation of the sample. For cantilever-TMV nanoindentation, the deformation is about 1.27 nm, the deformation of mica is less and equal to 0.02 nm.

Equation solver method is direct, and the solution technique is full Newton. The time step is determined automatically, with a minimum of  $1e-5$  s and a maximum of 0.1 s, and the simulation time period is set to 5 s.

FEM simulation is validated, and the force-depth penetration curves are plotted as follows:

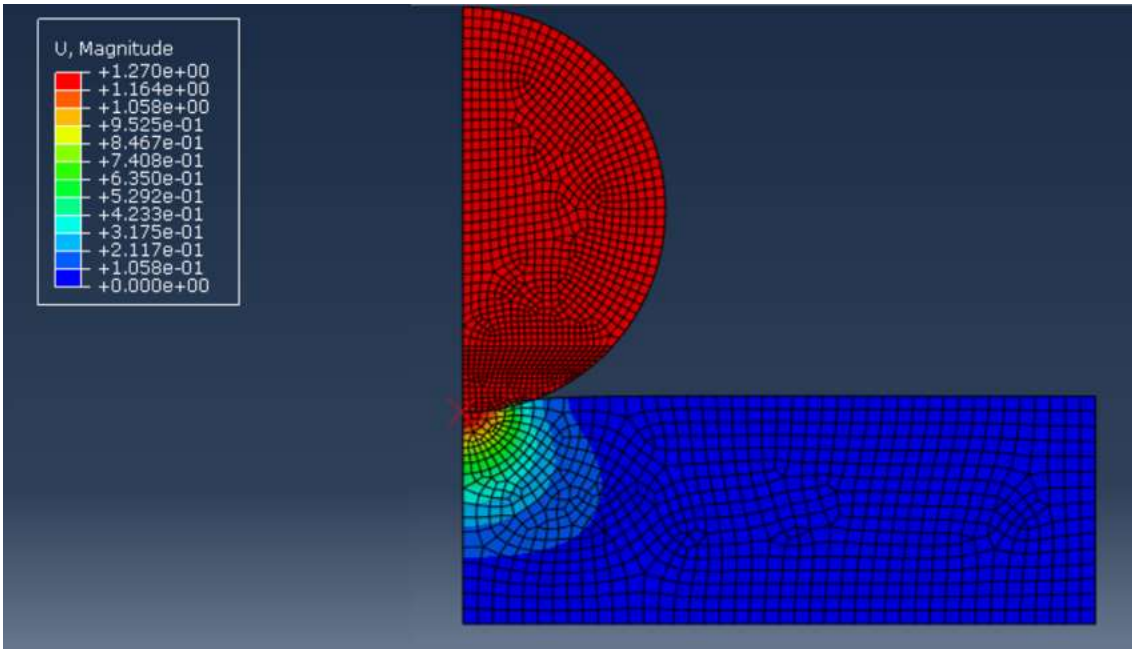


**Figure 42 FEM Simulation of Cantilever-TMV nanoindentation**

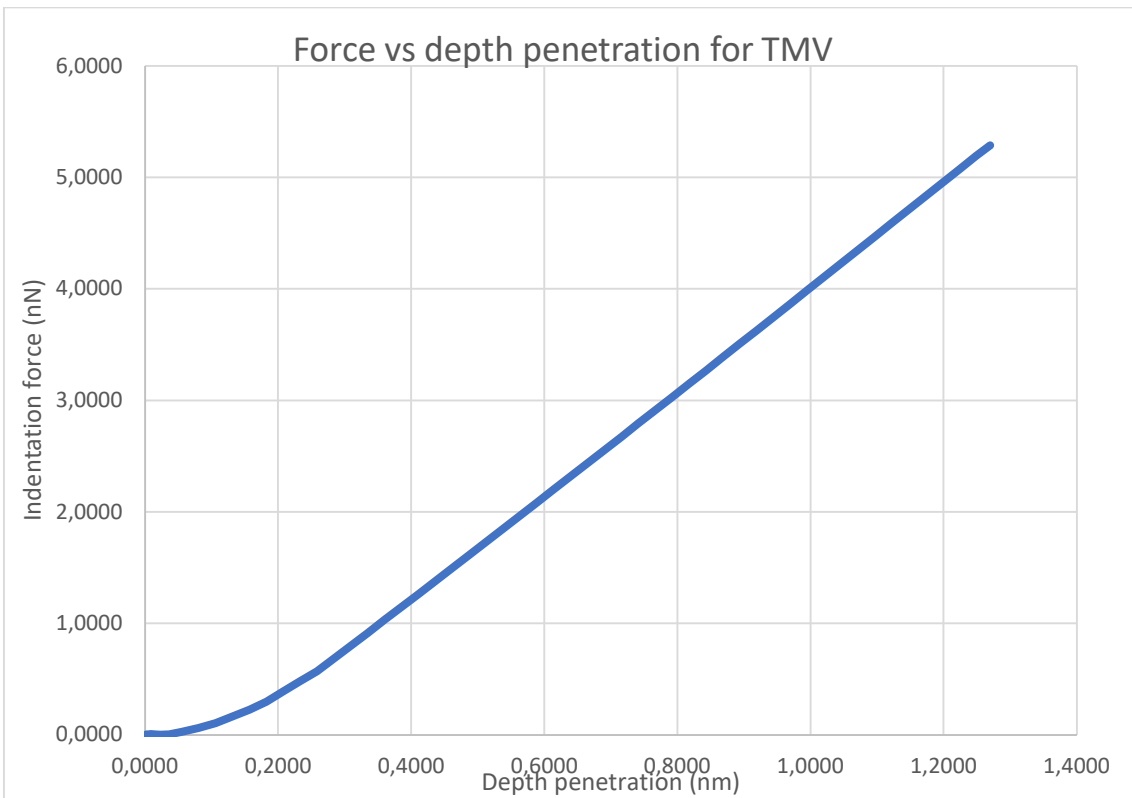


**Figure 43 FEM Validation for Force-depth penetration curve, TMV**

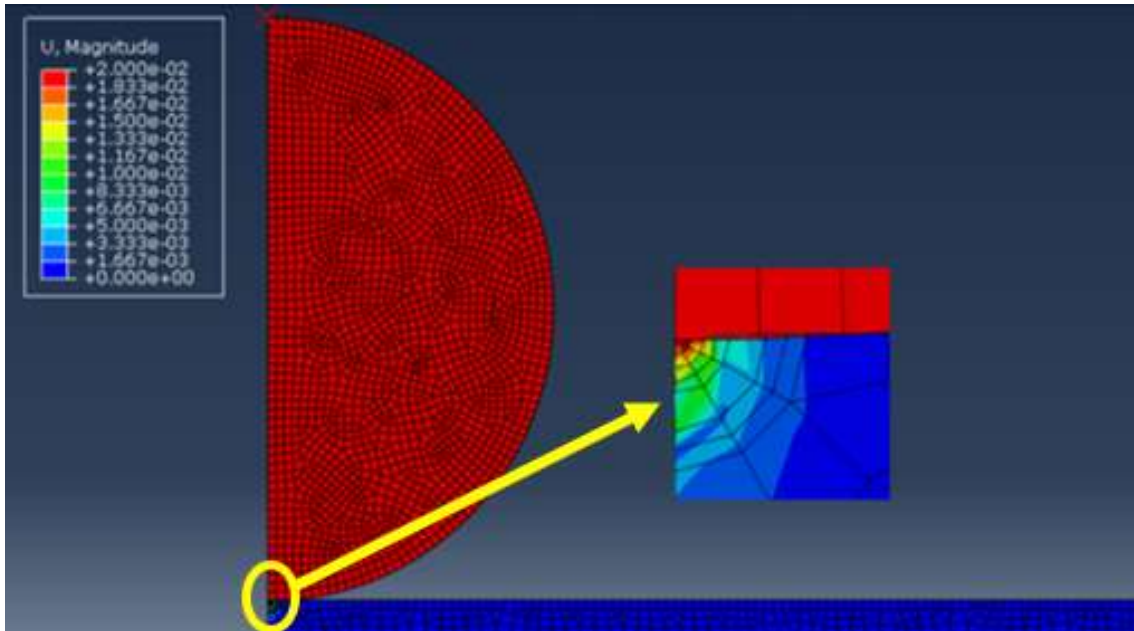


**Figure 44 FEM Simulation of cantilever-mica nanoindentation**

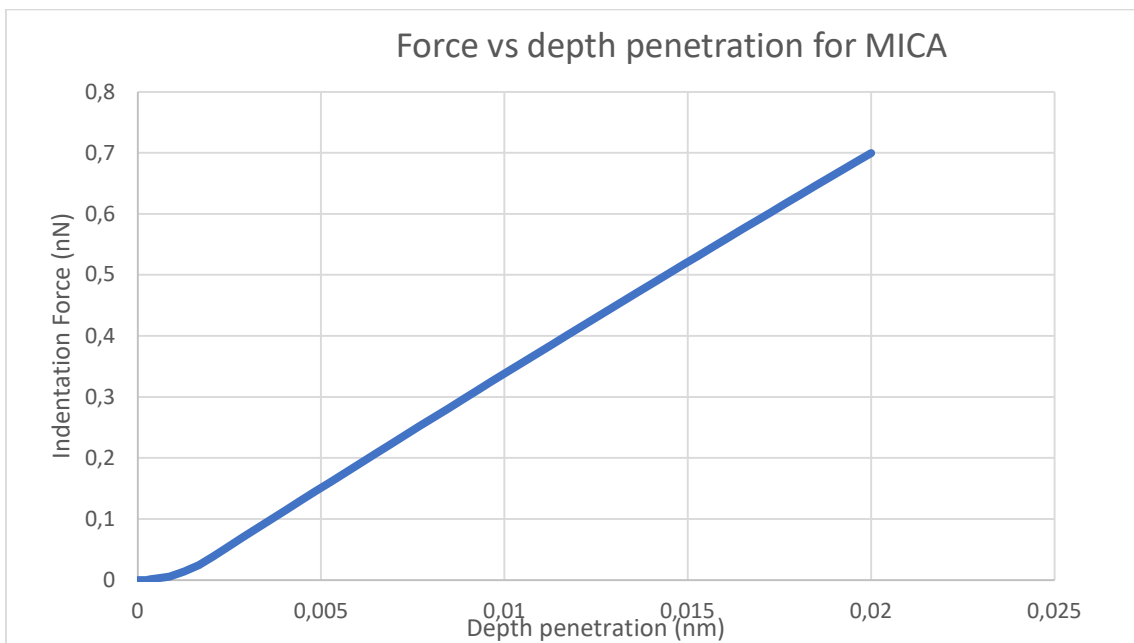


**Figure 45 FEM Validation for Force-depth penetration curve, Mica**

After having studied the relation between the normal force applied to the sample and its deformation, FEM simulation has been used to analyze how the contact area changes during the nanoindentation.

In the following figures these relations are showed.

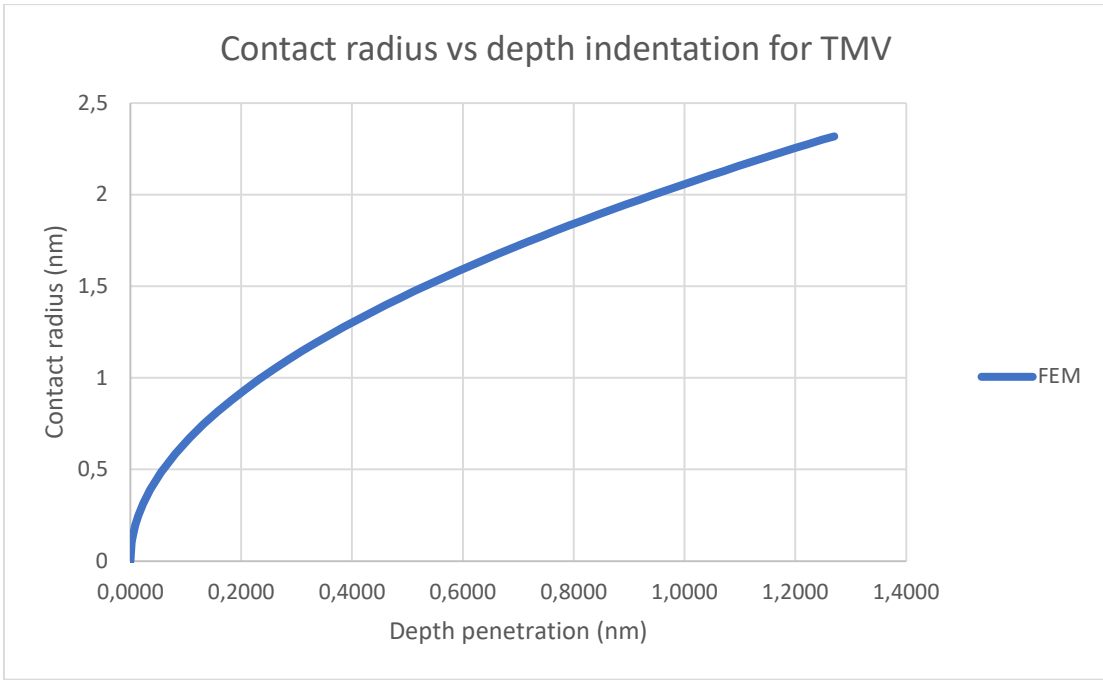


**Figure 46 FEM Validation for contact radius - depth penetration curve, TMV**

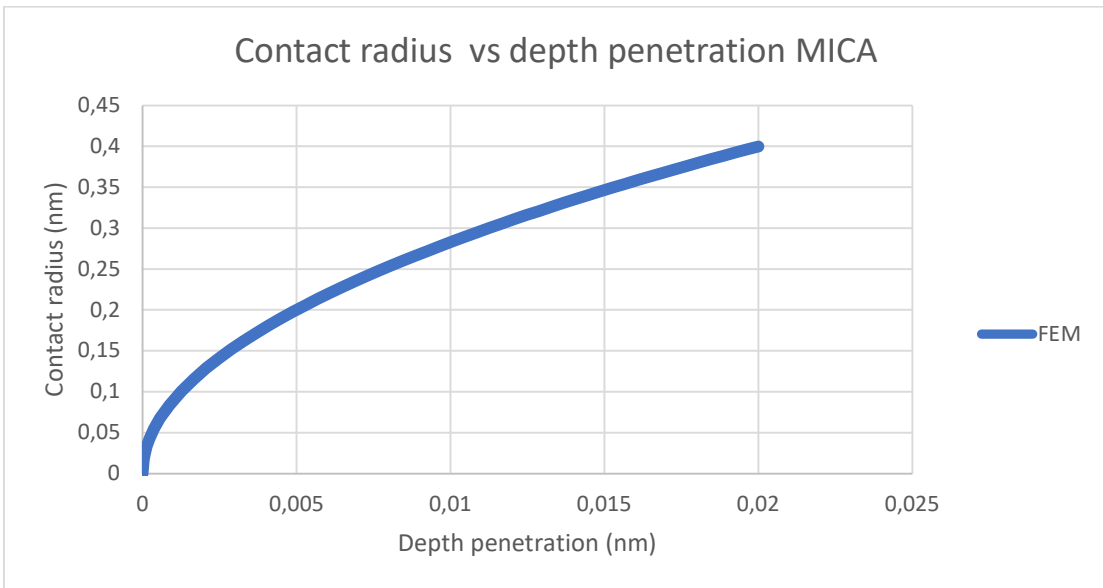


**Figure 47 FEM Validation for contact radius - depth penetration curve, Mica**

## 5 Discussion of the results

In this chapter the parameters and the results obtained will be discussed and compared, in order to prove that the method applied for the experiments with metrological AFM works well.

Hence, a dynamic analysis of the whole system has become the ideal instrument to assess whether the cantilever oscillates at the right resonant frequency, demonstrating that AFM can give a good topography of the sample. Indeed, the cantilever's dimensions and spring constant are two of the determining factors for this purpose.

Contact mechanics theories play an important role in these systems because they provide more information on the structural analysis of nanostructures. Their use represents a valid tool in the metrological field and help to validate that the effective dimension of the virus derives from homogeneity testing and remains stable under determined conditions.

### 5.1 Results from dynamic analysis

One of the steps to follow before starting AFM tests consists to check if the cantilever oscillates at a frequency much closer to its resonant value. The “Resonant tool” of the AFM plots a curve in which the amplitude, expressed in voltage, varies according to the cantilever frequency. These experimental tests are performed in the air, so the damping factor affects cantilever oscillation, reducing its oscillation period.

Q-factor is defined as the ratio between the resonant frequency and the full-width at the amplitude/ $\sqrt{2}$  of the resonance peak and expresses the energy dissipation capacity of a microcantilever.

For this reason, calculating the quality factor becomes a very important requisite for these experiments.

After plotting the dynamic response of the system through AFM in non-contact mode, different methods are used to compare all the results.

### Resonant Frequency (kHz)

Data	Experimental result	E-B eq. (2.9)	Reynolds eq. (2.10)	FEM Simulation
08/10/2020	160	160	160	153.8
20/10/2020	315.9	315.9	315.9	308.1

*Table 22 Comparison of resonant frequency*

### Quality factor

Data	Experimental result	E-B eq. (2.9)	Reynolds eq. (2.10)	FEM Simulation
08/10/2020	289	279	284	265
20/10/2020	790	781	782	771

*Table 23 Comparison of Q-factor*

Data	Mean value $\pm$ St. Dev. resonant frequency	Mean value $\pm$ St. Dev. Q-factor
08/10/2020	158.45 $\pm$ 2.7	279.38 $\pm$ 8.95
20/10/2020	313.95 $\pm$ 3.4	781.10 $\pm$ 6.75

*Table 24 Average value and standard deviation of resonant frequency and Q-factor*

The tables above show a comparison of the models for the calculation of resonant frequency and quality factor. In this case, it can be deduced that the resonant frequency, and consequently the Q-factor, calculated with simulations in Abaqus, are slightly underestimated with respect the experimental result. Another feature to underline is that the method that correlates Q-factor with Reynolds number is more accurate than Eulero-Bernoulli method. It is probably due to the dependence of Q-factor on the cantilever dimension in the E-B case, while Reynolds method says that the quality factor is related to the imaginary part of the hydro-dynamic function. Thus, the size of the cantilever is a more sensitive parameter to manage and, even if Eulero-Bernoulli equation does not prove ideal for determining Q-factor, it allows the cantilever dimensions to be reached. It is evident that greater the width and the length of the cantilever, higher the Q-factor. The same proportional relationship exists between Q-factor and frequency and

consequently cantilever spring constant.

For AFM working in the air, the Q-factor can be from  $10^2$  to  $10^3$ , while it is lower for applications in liquid.

## 5.2 Evaluation of the mechanical properties from static analysis

The main purpose of these experiments leads to the determination of the mechanical properties of Tobacco Mosaic Virus. One of these is the estimation of elastic properties for viruses. The introduction of the theories of contact mechanics, modified according to the system considered, is used to determine above all the Young modulus, the deformation of the sample  $h$  and the contact radius. The first novelty of this project is due to the use of AFM that works in non-contact mode. To date, indentation tests were performed in other Institutes of Research and more sophisticated AFM software provided more information about the mechanical properties of nanostructures. In this case, when the cantilever tip approaches to the sample, there is not contact between the bodies and the deformation of the sample is given by the attractive-repulsive force between tip and sample. Therefore, INRiM challenge is the determination of these properties without indentation and by using the theories just cited. So, the several types of tests performed in the Metrological Institute of Research are necessary to find the right parameters for the estimation of these properties. As just discussed in the previous chapter, all the tests are performed with tips that works in contact mode and non-contact mode, so that it is possible to underline possible differences.

In the following tables it is calculated the mean value and the standard deviation of the Young Modulus, the depth penetration and the contact radius.

	YOUNG MODULUS (GPa)	Mean Value ± St. Dev.
TMV	Young Modulus Hertz	1,27 ± 0,02
	Young Modulus JKR	0,923 ± 0,028
	Young Modulus DMT	1,02 ± 0,05
MICA	Young Modulus Hertz	190,0 ± 0,0
	Young Modulus JKR	174,0± 1,9
	Young Modulus DMT	188,0± 0,0

**Table 25** Young Modulus for TMV and Mica, Mean Value and Standard Deviation for

*contact tip*

	<b>Depth penetration</b>	<b>Mean Value ± St. Dev.</b>
<b>TMV</b>	h Hertz (nm)	1,09 ± 0,22
	h JKR (nm)	1,48 ± 0,25
	h DMT (nm)	1,34 ± 0,20
<b>MICA</b>	h Hertz (10 <sup>-2</sup> nm)	2,02 ± 0,34
	h JKR (10 <sup>-2</sup> nm)	2,10± 0,34
	h DMT (10 <sup>-2</sup> nm)	2,02 ± 0,34

**Table 26** *Depth penetration for TMV and Mica, Mean Value and Standard Deviation for contact tip*

	<b>Contact radius</b>	<b>Mean Value ± St. Dev.</b>
<b>TMV</b>	a Hertz (nm)	2,13 ± 0,21
	a JKR (nm)	3,29 ± 0,19
	a DMT (nm)	2,37 ± 0,18
<b>MICA</b>	a Hertz (Å)	4,00 ± 0,32
	a JKR (Å)	4,25± 0,31
	a DMT (Å)	4,01 ± 0,32

**Table 27** *Contact radius for TMV and Mica, Mean Value and Standard Deviation for contact tip*

In these tables it is evident that the introduction of the adhesion force in JKR and DMT method changes the elastic properties both for the sample and the substrate. The contact area and the deformation of the samples are calculated as a function of the force applied. The contribute of the adhesion force leads to a larger contact radius, and consequently the depth indentation undergoes a little increase. The variation of the sample's deformation is due to the surface energy per unit area. In the case of mica, the surface energy is very small, and the depth indentation is quite similar to that of Hertz, while TMV's deformation increase respectively by 18% and 26% using DMT and JKR method, compared to the Hertzian deformation.

A larger contact area implies a decrease of the reduced Young modulus  $E^*$ : it means that the elastic modulus of the sample calculated by introducing the surface energy is lower

than the Young modulus estimated by Hertz.

The standard deviation for each test is very low, then all the properties calculated does not change according to the type of cantilever used. This consideration is valid only for tips that work in contact-mode. Now let us show how elastic properties change if a non-contact tip is used.

		<b>Mean Value ± St. Dev. For TMV</b>	<b>Mean Value ± St. Dev. For MICA</b>
<b>Young Modulus (GPa)</b>	HERTZ	1,29± 0,01	190,0± 0,0
	JKR	0,722± 0,054	167,00± 12
	DMT	0,719± 0,068	186,00± 3
<b>Depth penetration (Å)</b>	HERTZ	5,93± 4,27	0,171± 0,139
	JKR	10,1± 6,9	0,176± 0,142
	DMT	10,0± 6,8	0,171± 0,140
<b>Contact radius (Å)</b>	HERTZ	14,6± 6,2	3,28± 1,71
	JKR	28,7± 10,9	3,50± 1,71
	DMT	19,2± 7,5	3,29± 1,70

**Table 28 Mechanical properties estimated with non-contact cantilever**

In this case it is possible to underline that the interaction between non-contact tip and mica estimates values of the mechanical properties closer to those measured with contact-tip. The interaction between TMV and non-contact tip is probably affected by errors, and it is confirmed by the high standard deviation. Errors can be determined either by spectroscopy force measurements, or by the choice of topography area of TMV to analyze. Another reason that makes this measurement explainable is the different spring constant of the cantilever used for both tests, respectively equal to 5 N/m and 46 N/m.

The final part of the thesis is characterized by the comparison of the theories applied for Young modulus estimation with the results obtained from FEM Simulation. Even if the Metrological AFM has worked in non-contact mode, Abaqus software simulates indentation between bodies, in which the stroke of the tip is equal to the body deformation. Therefore, considering the same range of depth penetration, force-

displacement curve and contact radius-displacement curve are showed applying the various methods used in this discussion.

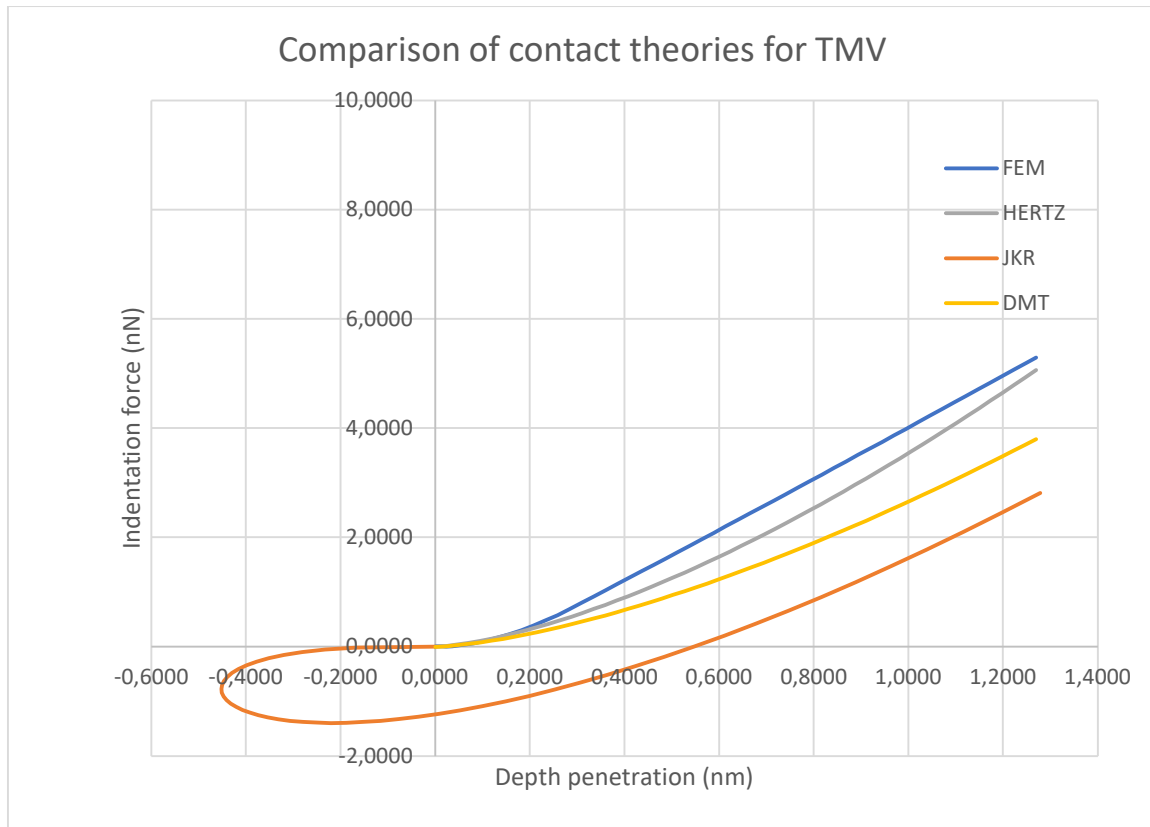


**Figure 48 Indentation force - Depth penetration curve for TMV and comparison with other methods**

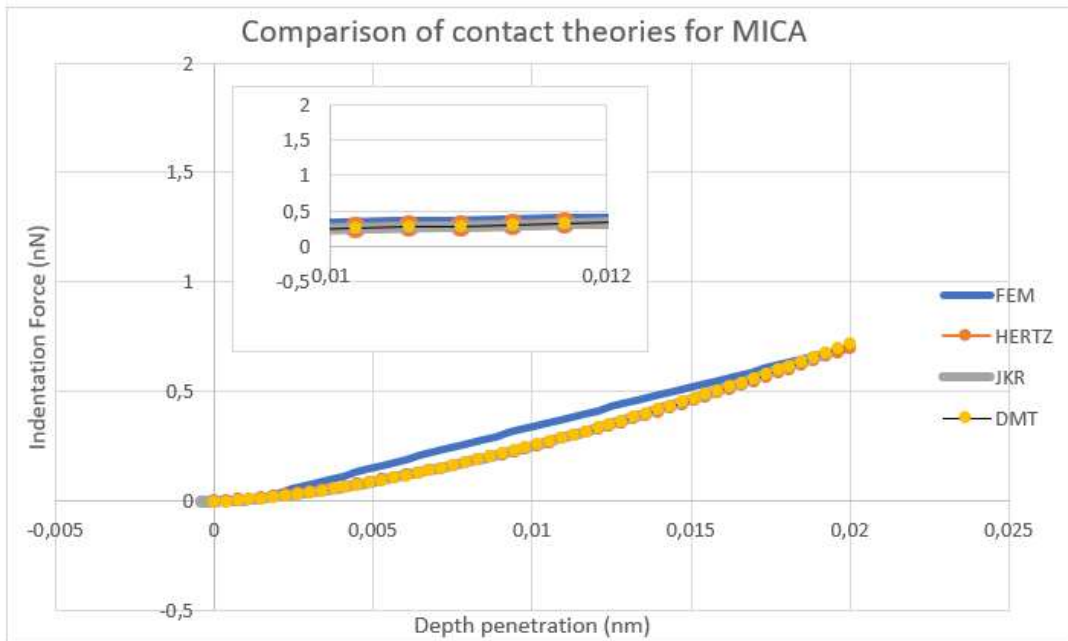


**Figure 49 Indentation force - depth penetration curve for mica and comparison with other method**

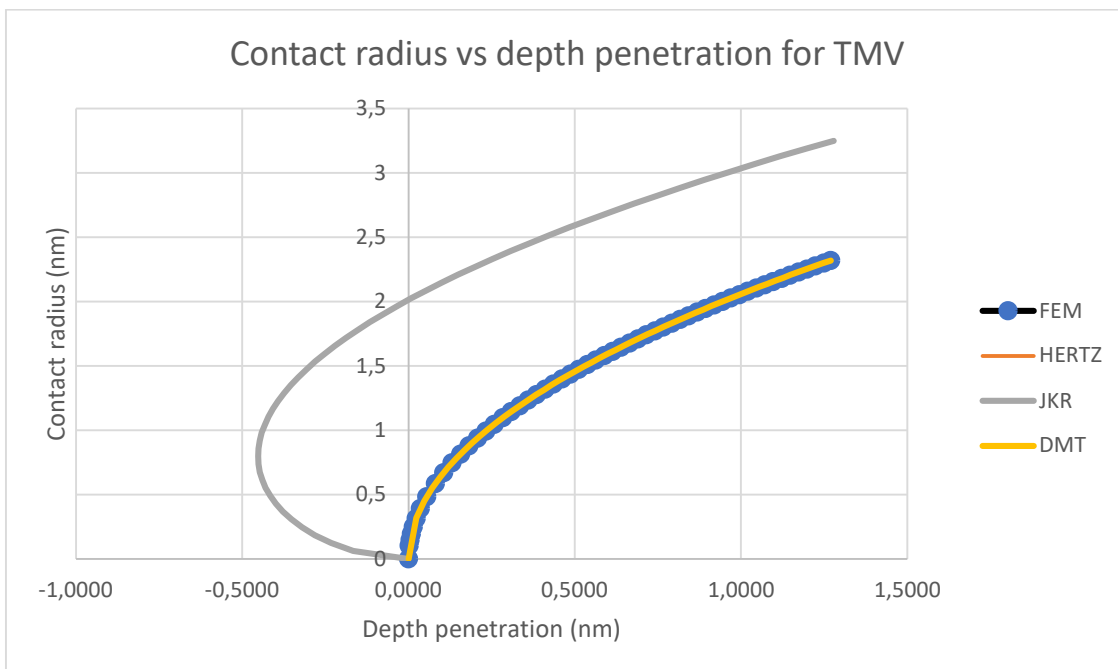


**Figure 50 Contact radius - depth penetration for TMV and comparison with the other theories**

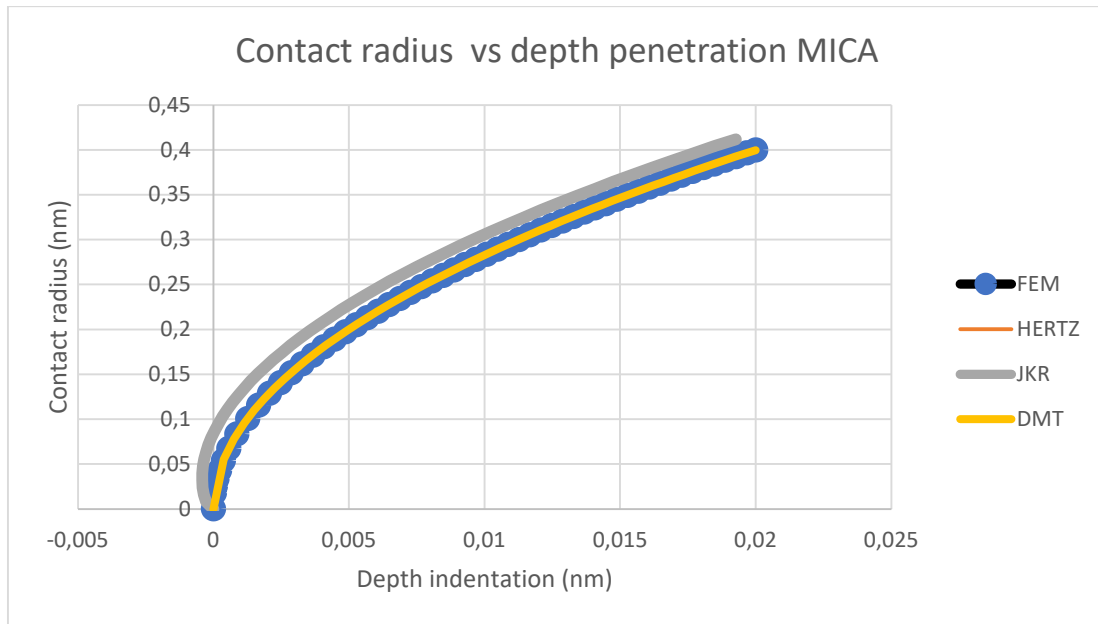


**Figure 51 Contact radius - depth penetration for mica and comparison with the other theories**

Hertz and FEM curves are very closer to each other and the variation between the curves can be neglected. It means that Abaqus is a suitable software for the nanoindentation tests analysis and for the comparison with AFM that works in non-contact mode. There are some differences between Hertz, JKR and DMT methods. Figures 49 and 50 show how the force applied changes when the indentation increases. These considerations are valid if it is assumed that  $h_{HERTZ} = h_{JKR} = h_{DMT}$ . The DMT curve has the same slope of Hertz's one but at  $h = 0$  the force is negative because it only considers the contribute of adhesion force,  $2\pi\gamma R$ . According to the model, the Van der Waals force acts along the contact area and it is added to the compression force between the cantilever tip and the sample. In this way, the repulsion force is weakened. The geometry does not differ much: in fact, figure 50 and figure 51 show that DMT curve overlaps with Hertz's one.

According to the JKR method, the Van der Waals force is applied within the contact zone, and the force-displacement curve has a different shape: a negative force corresponds to a negative depth penetration, generating a sort of neck whose area is equal to the surface energy per unit of area. It means that the adhesion force enforces the elastic repulsion force and for this reason the force magnitude can be decreased. For the same reason, the contact area is larger than Hertz's one with the same deformation. Force-displacement curve for mica describes curves very closer to each other because the surface energy per unit area used is very low.

In figure 52 and 53 it is showed how force-displacement curve modifies if the Young modulus is changed. In this contest, the elastic modulus goes from 0.9 to 1.3 GPa for TMV, from 170 to 190 GPa for mica. For both cases, force is linear proportional to the elastic modulus and it increases if the stiffness is higher.

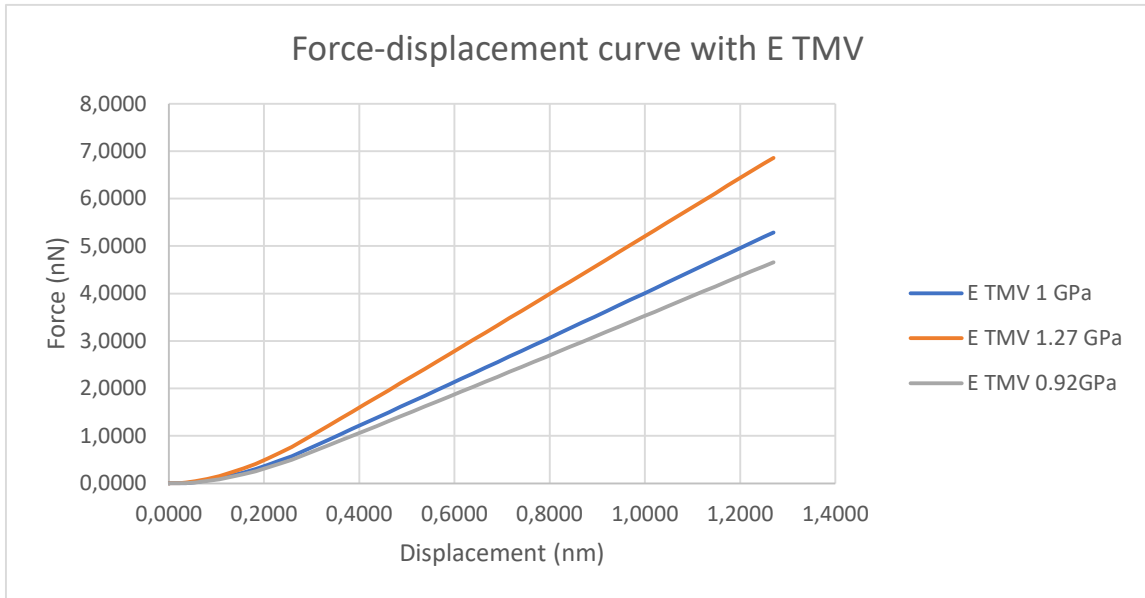


**Figure 52 Force-displacement curves varying TMV Young Modulus**

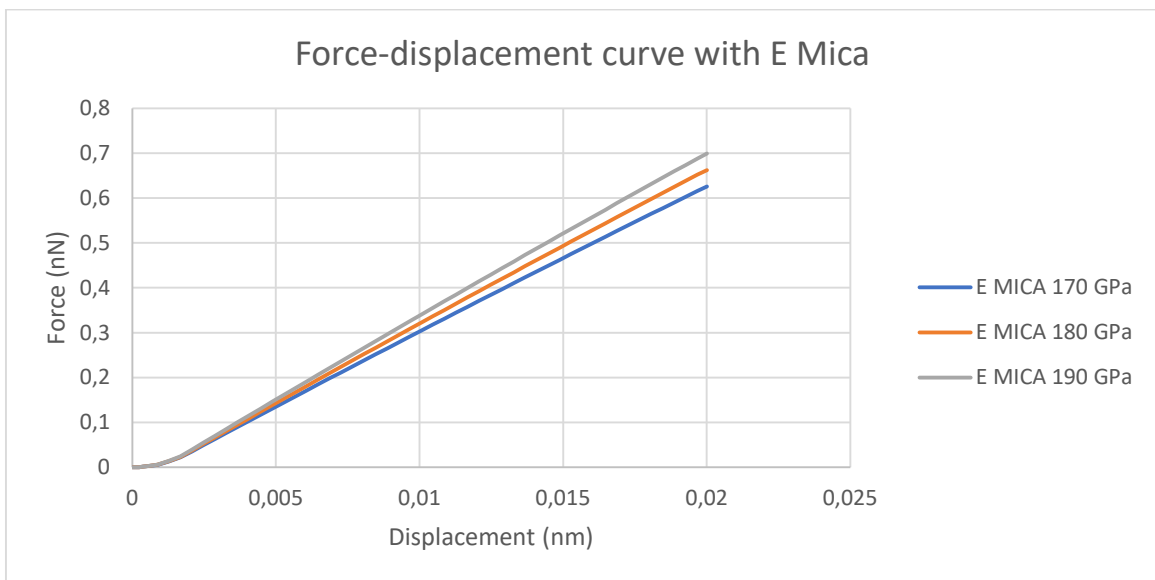


**Figure 53 Force-displacement curve varying Mica Young Modulus**

## 6 Conclusion and future works

In the last years, metrology research focused on the study of mechanical properties of nanostructure and biological systems. Such properties play an important role in the biological process since they are often linked with biological functions. For instance, viruses can modify their characteristics as function of the outside force applied on the system: a mutation of a protein that constitutes their structure can change their elastic properties. For this reason, it is very important to find a way to perform some tests with accurate nanotools in order to estimate how these features change with the sample. These efforts are aimed at a greater knowledge of physiological and biochemical properties of viruses and virus-based nanomaterials. The Institute National Research in Metrology (INRiM) uses a metrological AFM for this purpose: the mechanical analysis of nanostructures is fundamental to define the ideal reference material for the International System (SI). Therefore, it is necessary to demonstrate the stability of Tobacco Mosaic Virus in dimension and over time.

All the tests are performed by using a metrological AFM that works in non-contact mode, and cantilever tips produced by Veeco and Mikromasch are used to compare all the results. The resonant frequency is a parameter that acquires an important function because it varies as function of the mechanical stiffness of absorbed virial nanotubes and it is essential to describe how cantilever tips behave during its oscillation. The damping factor points out that its amplitude oscillation reaches a peak without tending to infinite and depends on material properties and geometry. All the methods adopted are useful to understand the reliability of the theory that defines that models and the correct use of FEM Simulation to study cantilever's dynamic response.

The real need to correlate biomedical and mechanical studies through AFM investigations opens the doors to the research of the real value of TMV's Young Modulus. It can contribute to resolve some questions regarding the virial variability, the infective potential and how it can change according the mutation of its structure. Therefore, it allows to investigate how TMV is deformed when cantilever tip approaches to the sample. Metrological AFM has been demonstrated to be a great tool for this purpose. Even if it

generally works in non-contact mode, the amplitude oscillation and the spectroscopy force tests carry out the necessary value for the determination of the reduced elastic modulus and sample's deformation. This methodological approach is supported by the contact mechanics theories studied in the last century. Thus, the Hertzian elastic modulus is  $1.27 \pm 0.02$  GPa, higher than the Young modulus estimated by JKR method ( $0.92 \pm 0.03$  GPa) and by DMT method ( $1.02 \pm 0.06$  GPa). At the same time, depth penetration and contact radius are determined, and it is observed that Hertz method leads to a sample's deformation equal to  $1.09 \pm 0.26$  nm and contact radius is about  $2.02 \pm 0.38$  nm. The introduction of surface energy per unit area in JKR and DMT methods gives the highest deformation of TMV: according to JKR theory, the depth indentation and the contact radius are respectively  $1.48 \pm 0.30$  nm and  $2.10 \pm 0.38$  nm; DMT methods says that TMV has a deformation equal to  $1.34 \pm 0.24$  nm and the same contact radius of that calculated by Hertz.

FEM Simulation has helped to evaluate if these measurements can be confirmed or if the method used should be changed or not. This software is employed for nanoindentation test, and it differs from the experimental tests performed. Nevertheless, the results given by Finite Element Method are close to that calculated from Hertz method, as function of the parameters derived from Metrological AFM tests. It means that an atomic force microscope working in non-contact mode can be used indirectly for nanoindentation test, with good approximation. This tool is not adequate to verify if JKR and DMT methods work well, so a suggestion for a future work is to try to use a nanoindenter in order to confirm the work done until today and to underline the importance of surface energy when the cantilever approaches and retracts from the sample.

All the measurements performed with non-contact tips give the same Young Modulus of those done with contact tips. It means that the experimental tests are carried out in a correct way. Nevertheless, all the other parameters estimated by using non-contact cantilever tips are lower than the ones calculated with contact-tips. It is probably since the interaction force between tip and sample is very low. However, the standard deviation given by these measurements is very high, so there is needed to compare several types of non-contact tips for a more accurate determination of mechanical properties.

The idea of this project is to give a valid alternative to the existing methods for the determination of these characteristics, underlining possible *food for thought* for future improvements and to help the research to connect the biological world to the mechanical one, apparently distant but very interconnected with each other.

# Bibliography

---

<sup>1</sup> Bert Voigtländer, *Scanning Probe Microscopy: Atomic Force Microscopy and Scanning Tunneling Microscopy*; Springer; 2015

<sup>2</sup> Peter Eaton, Paul West, *Atomic Force Microscopy*, Oxford University Press, 2010

<sup>3</sup> A. Mendez, J. Diaz, *Introduction to Atomic Force Microscopy Simulation*, May 2010, (pp.1338- 1349), Edition: 1

<sup>4</sup> Arivazhagan Rajendran, Masayuki Endo and Hiroshi Sugiyama, *State-of-the-Art High-Speed Atomic Force Microscopy for Investigation of Single-Molecular Dynamics of Proteins* pag 1493-1518, 12 November 2013

<sup>5</sup> Davide Ricci and Pier Carlo Braga, *How the Atomic Force Microscope Works*, 2004-Springer, pag. 3-12

<sup>6</sup> I.A. Mahmood, S.O. Reza Moheimani, *Making a commercial atomic force microscope more accurate and faster using positive position feedback control*, Review of Scientific Instrument 80, 063705(1-8) (2009);

<sup>7</sup>Y. Martin, C.C. Williams and H.K. Wickramasinghe, *Atomic force microscope–force mapping and profiling on a sub 100-Å scale*, J. Appl. Phys. 61 (1987) 4723-4729.

<sup>8</sup> G. Binnig, C. Gerber & C. Quate, *Atomic Force Microscope*, PRL 56 (1986) 930

<sup>9</sup> A. Schirmeisen, B. Anczykowski, and Harald Fuchs, *Dynamic Modes of Atomic Force Microscopy*, Nanotribology and nanomechanics, pp. 243-281

<sup>10</sup> Zackary N. Scholl, Qing Li, Eric Josephs, Dimitra Apostolidou, Piotr E. Marszalek, *Force Spectroscopy of Single Protein Molecules Using an Atomic Force Microscope*, Mechanical Engineering and Material Science, Duke University, February 2019,

<sup>11</sup>Rifkind, D., & Freeman, G. L. *TOBACCO MOSAIC VIRUS. The Nobel Prize Winning Discoveries in Infectious Diseases*, (2005), 81–84.

<sup>12</sup> Creager N. H. Angela, *The Life of a Virus: Tobacco Mosaic Virus as an Experimental Model, 1930-1965*, The University of Chicago Press, 2002

<sup>13</sup> Lomonosoff, G. P., & Wege, C. *TMV Particles: The Journey From Fundamental Studies to Bionanotechnology Applications. Advances in Virus, 2018 Research*. 2018.06.003

<sup>14</sup> Yuri F. Drygin, Olga A. Bordunova, Marat O. Gallyamov, Igor V. Yaminsky, *Atomic*

---

*force microscopy examination of tobacco mosaic virus and virion RNA*, FEBS Letters 425 (1998) 217-221

<sup>15</sup> Yuri L. Lyubchenko,<sup>a,\*</sup> Luda S. Shlyakhtenko,<sup>a</sup> and Toshio Ando, *Methods. Imaging of nucleic acids with atomic force microscopy*, 2011 Jun; 54(2): 274–283.

<sup>16</sup> Othmar Marti, *Measurements of Adhesion and pull-off forces with the AFM*, Experimental Physics, Ulm University, December 2000

<sup>17</sup> Voigtländer, B. (2019). *Atomic Force Microscopy. NanoScience and Technology*

<sup>18</sup> A.F. Payam, Morteza Fathipour, *Modeling and dynamic analysis of atomic force microscopy based on Eulero-Bernoulli beam theory*, September 2009, Digest Journal of Nanomaterials and biostructures.

<sup>19</sup> Feodosov V.I. *Strength of Materials*, MSTU publishing, 2000 – 392 p.

<sup>20</sup> Sader, J. E., Chon, J. W. M., & Mulvaney, P. (1999). *Calibration of rectangular atomic force microscope cantilevers. Review of Scientific Instruments*, 70(10), 3967–3969.

<sup>21</sup> V.L.Popov, *Rigorous Treatment of Contact Problems – Hertian contact*, Springer, January 2010, pp. 55-70

<sup>22</sup> H. Hertz, *Über die Berührung fester elastischer Körper*, Journal für die reine und angewandte Mathematik 92, 156-171 (1881)

<sup>23</sup> E. Placidi, *Introduction to Atomic Force Microscopy*, 2016, pp. 1-30

<sup>24</sup> Marius Enachescu, *Nanoscale Effects of Friction, Adhesion and Electrical Conduction in AFM Experiments*, University POLITEHNICA of Bucharest, March 2012, 99-140

<sup>25</sup> Xiang Gao, Feng Hao, Zhuping Wang, Daining Fung, *Mechanics of adhesive contact at the nanoscale: The effect of surface stress*, International Journal of Solid and Structure, February 2014, pp.566-574

<sup>26</sup> Xinghua Shi and Ya-Pu Zhao, *Comparison of various adhesion contact theories and the influence of dimensionless load parameter*, *J. Adhesion Sci. Technol.*, Vol. 18, No. 1, pp. 55–68 (2004)

<sup>27</sup> Kyriakos Grigoriadis, Anastasios Zavos, and Pantelis G. Nikolakopoulos, *Comparison of Hertzian and JKR theories with a finite element model in boundary lubrication conditions between a compression ring and a cylinder*, MATEC Web of Conferences 188, 04009 (2018)

<sup>28</sup> H. S. Tanvir Ahmed, Eric Brannigan, and Alan F. Jankowski, *On the Tapping Mode Measurement for Young's Modulus of Nanocrystalline Metal Coatings*, Journal of Nanotechnology, 2013

---

<sup>29</sup> Gaylord Guillonnet, Guillaume Kermouche, Sandrine Bec, Jean-Luc Loubet *Determination of mechanical properties by nanoindentation independently of indentation depth measurement*, Journal of Materials Research, Cambridge University Press (CUP), 2012, 27, pp.2551-2560. [ff10.1557/jmr.2012.261](https://doi.org/10.1557/jmr.2012.261)ff. [ffhal-00826308](https://doi.org/10.1017/fhal-00826308)f

<sup>30</sup> A.I. Bayley, *Surface and interfacial tension*, thermopedia.com, 2010

<sup>31</sup> Ruz, J., Tamayo, J., Pini, V. et al. *Physics of Nanomechanical Spectrometry of Viruses*. Sci Rep 4, 6051 (2014). <https://doi.org/10.1038/srep06051>